

UNIVERSIDADE DE SÃO PAULO  
INSTITUTO DE FÍSICA DE SÃO CARLOS

PAULO CESAR VENTURA DA SILVA

Photoassociation and vibrational cooling of  $\text{Rb}_2$  molecules with a high-  
power laser

São Carlos  
2016



PAULO CESAR VENTURA DA SILVA

Photoassociation and vibrational cooling of Rb<sub>2</sub> molecules with a high-power laser

Dissertation presented to the Graduate Program in Physics at the Instituto de Física de São Carlos, Universidade de São Paulo to obtain the degree of Master of Science.

Concentration area: Basic Physics

Advisor:  
Prof. Dr. Luis Gustavo Marcassa

Corrected Version

(Original version available on the Program Unit)

São Carlos  
2016

AUTHORIZE THE REPRODUCTION AND DISSEMINATION OF TOTAL OR PARTIAL COPIES OF THIS THESIS, BY CONVENCIONAL OR ELECTRONIC MEDIA FOR STUDY OR RESEARCH PURPOSE, SINCE IT IS REFERENCED.

Cataloguing data reviewed by the Library and Information Service  
of the IFSC, with information provided by the author

Silva, Paulo Cesar Ventura da  
Photoassociation and vibrational cooling of Rb<sub>2</sub>  
molecules with a high-power laser / Paulo Cesar  
Ventura da Silva; advisor Luis Gustavo Marcassa -  
reviewed version -- São Carlos 2016.  
108 p.

Dissertation (Master's degree - Graduate Program  
in Basic Physics) -- Instituto de Física de São  
Carlos, Universidade de São Paulo - Brasil , 2016.

1. Molecular physics. 2. Rubidium. 3.  
Photoassociation. 4. Vibrational cooling. 5. REMPI  
spectroscopy. I. Marcassa, Luis Gustavo, advisor.  
II. Title.

## **ACKNOWLEDGEMENTS**

Thanks to my father, who is always willing to help me in whatever he can. Thanks also to my family as a whole.

To my partners of the cold molecules experiment, Henry and Ricardo. Only we know the difficulties and tough situations that we had to face during these years of work, and I admire how bravely you dealt with them. To our advisor Marcassa, who guided us through this, and to the Photonics group as a whole.

To all the teachers and professors that I had during my life, specially the physics teachers from the high school, whose talent motivated me to be a physicist.

To the Vôlei CAASO family, the volleyball team where we practice unity and team work.

Thanks to our collaborators Olivier Dulieu and Nadia Bouloufa-Maafa, for providing the theoretical basis of our research.

Thanks to FAPESP for the financial support (grant n. 2014/24479-6).



## ABSTRACT

SILVA, P. C. V. **Photoassociation and vibrational cooling of Rb<sub>2</sub> molecules with a high-power laser**. 2016. 108 p. Dissertation (Master in Science) - Instituto de Física de São Carlos, Universidade de São Paulo, São Carlos, 2017.

We have developed a technique to produce, manipulate and trap Rb<sub>2</sub> molecules with a single optical beam. This beam is generated by a high-power fiber amplifier (50 W of total output power) in the 1060 to 1070 nm range, which is seeded by two light sources: a sharp-band laser and a broadband superluminescent diode. The laser source is tuned to produce Rb<sub>2</sub> molecules from an ultracold <sup>85</sup>Rb sample via photoassociation. The broadband spectrum vibrationally cool the molecules by optical pumping. This source is spectrally shaped in order to populate the molecules at the fundamental vibrational state  $\nu = 0$ . The molecular sample is probed by two-photon ionization, promoted by a pulsed dye laser in the 475 to 480 nm range. By scanning the photoassociation laser frequency, we have obtained a photoassociation spectrum of the  $\nu' = 138$  state of the  $0_u^+$  potential, confirming previous observations. We have also obtained two vibrational spectra of the molecules by varying the ionization laser frequency, in the presence and absence of the broadband source. The comparison between the two spectra, along with *ab-initio* data, provides evidences that the molecules are optically pumped to the fundamental vibrational state.

Keywords: Molecular physics. Rubidium. Photoassociation. Vibrational cooling. REMPI spectroscopy.



## RESUMO

SILVA, P. C. V. **Fotoassociação e resfriamento vibracional de moléculas de Rb<sub>2</sub> com um laser de alta potência.** 2016. 108 p. Dissertação (Mestrado em Ciências) - Instituto de Física de São Carlos, Universidade de São Paulo, São Carlos, 2017.

Desenvolvemos uma técnica para produzir, manipular e aprisionar moléculas de Rb<sub>2</sub> com um único feixe óptico. Esse feixe é gerado por um amplificador de alta potência (50 W de potência total de saída) na faixa de 1060 a 1070 nm, que é alimentado por duas fontes de luz: um laser banda estreita e um diodo superluminescente banda larga. O laser é sintonizado para produzir moléculas de Rb<sub>2</sub> a partir de uma amostra ultrafria de <sup>85</sup>Rb via fotoassociação. O espectro banda larga resfria vibracionalmente as moléculas, por bombeamento óptico. Essa fonte de luz tem seu espectro formatado de modo a deixar as moléculas em seu estado vibracional fundamental  $\nu = 0$ . A amostra molecular é testada por ionização de dois fótons, promovida por um laser de diodo pulsado na faixa de 475 a 480 nm. Variando a frequência do laser de fotoassociação, obtivemos um espectro de fotoassociação do estado  $\nu' = 138$  do potencial  $0_u^+$ , confirmando observações anteriores. Obtivemos também dois espectros vibracionais das moléculas variando a frequência do laser de ionização, com e sem a fonte banda larga. Uma comparação entre os dois espectros, junto de dados *ab-initio*, fornece evidências de que as moléculas são opticamente bombeadas para o estado vibracional fundamental.

Palavras-chave: Física molecular. Rubídio. Fotoassociação. Resfriamento vibracional. Espectroscopia REMPI.



## LIST OF FIGURES

- Figure 1 - Examples of potential curves constructed with spectroscopic data from Rb2 molecules. In this case, each curve contains one stable equilibrium point, meaning that bound states are allowed. .... 30
- Figure 2 - Representation of the classical statement of Franck-Condon principle. Transition i) is strong (more likely) because it preserves nuclear relative position and velocity. Transitions ii) and iii) are weak (less likely), as they change the velocity and the position of the nuclei, respectively. .... 32
- Figure 3 - Schematic representation of the photoassociation process. In i), an initially free atomic pair absorbs a photon and is excited to a bound state of a certain excited electronic potential. This is the photoassociation itself. In ii), the atomic pair spontaneously decay to a bound state of the ground electronic potential. .... 36
- Figure 4 - Ionization spectra of Na2 as a function of the PA laser frequency  $\nu$  (zero set on atomic  $S_{(1/2)} \rightarrow P_{(3/2)}$  transition). a) Broad spectrum showing several peaks, corresponding to different vibrational levels of the 1g potential. The inset shows the shows the region from 0 to -5GHz. b) Fine spectrum of a single vibrational peak, showing off the molecular hyperfine structure..... 37
- Figure 5 - A Feshbach resonance is possible when the energy of a bound state ( $E_c$ ) in a certain potential is close to the energy of free atoms ( $E$ ) in another potential (for ultracold atoms,  $E$  is assumed to be the asymptote of the potential). If the dipole moments in each potential (closed and open channels) are different, it is possible to use a magnetic field to compensate for the energy difference between the states. With the right magnetic tuning, a spontaneous mixing of the states leads to production of molecules..... 39
- Figure 6 - Schematic representation of the molecular optical pumping process. A broadband light source is used to excite molecules from the various vibrational levels of the ground potential; once excited, they spontaneously decay to other random vibrational levels. In this example, the molecule absorbs and emits two times until it falls to the fundamental  $v$  state. Once there, it cannot be excited again, as the light source is shaped for this purpose. .... 40
- Figure 7 - Scheme for molecular optical pumping, in Viteau's Cs2 experiment. In A, the broadband light is spectrally open by a diffraction grating, and then a blocker cuts the "blue" part of the spectrum. In B, Franck-Condon map is shown. The cutoff frequency is so that all transitions from  $v_x = 0$  are forbidden..... 41
- Figure 8 - Main results from Viteau's work. Molecular detection is performed via REMPI, an ionization technique sensitive to different vibrational states. In a), REMPI spectrum is measured after several pumping cycles. Comparison between spectrum with (B) and without(A) broadband shaping evidences the optical pumping process, as in B only the peaks from  $v = 0$  are notorious. In

	b), peaks from different vibrational states are measured in function of the number of pumping laser pulses. It is possible to observe the populational transfer from other states to $v = 0$ .....	42
Figure 9 -	Results for the second vibrational cooling experiment. (a) The setup for $v=0$ pumping was changed, having the grating-blocker replaced by a set of long-pass filters. The final spectrum shape (b) and the results in molecular transfer (c) remained the same. (d) A different concept was used for $v = 1$ pumping. The light spectrally open by a grating is shaped by four small blockers in specific positions. The final spectrum (e) has the bands which excite $v = 1$ transitions removed, making this a dark state. Experimental REMPI spectrum (f) shows the populational accumulation on this state.....	43
Figure 10 -	Schematic drawing of the vacuum system where the experiment is performed. Part 1 indicates the atomic oven, where an Rb sample is heated to around 90 °C, providing an atomic flow of $2 \cdot 10^{16}$ atoms/s. The tube in part 2 is the Zeeman slower, where atoms with an initial speed below 346 m/s are decelerated to a few m/s before entering the final vacuum chamber, indicated on part 3. In this chamber, a pressure below $10^{-11}$ Torr is maintained, providing an adequate environment to the atomic and molecular traps. ....	46
Figure 11 -	Schematic representation of the MOT restoring force. A non-uniform magnetic field (fig. a) splits the states with different $m_F$ . The beam that comes from the positive z side (right) is circularly polarized to the left, and the other beam is polarized to the right. Due to selection rules and the laser detuning to the red, atoms that have positive z coordinate are more resonant with the beam that comes from the right, having a net force to the left. The opposite situation happens at the negative z side. ....	48
Figure 12 -	Hyperfine structure of rubidium-85 D2 line. The two laser frequencies used for the MOT (trapping and repumping) are shown by blue and red arrows, respectively.....	49
Figure 13 -	Comparison between single beam ODT (a) and crossed ODT (b). The confinement along the propagation axis in case (a) is poor, whereas crossed ODT has a good confinement in all spatial directions. ....	51
Figure 14 -	Optical setup for trapping, repumping and Zeeman slower. Both laser frequencies are determined and locked by saturated absorption spectroscopy (SAS) technique. (75) Trapping beam is detuned by AOM2 and amplified by a TA. Repumping beam is detuned by AOM5. Zeeman slower receives light from both trapping and repumping sources, and is twice amplified before sent to the experiment. ....	53
Figure 15 -	Optical setup for the crossed optical dipole trap. The high power light is provided by a fiber amplifier, which provides up to 50 W. An AOM is used to control the laser intensity during the experiment. The same laser source is	

	used to create the two arms of the crossed trap. The waist at the focus is of $\approx 40 \mu\text{m}$ .	54
Figure 16 -	Calculated Franck-Condon factors for the photon absorption from $X^1\Sigma_g^+$ to $0_u^+$ , which is used to the photoassociation. The calculations consider the most excited vibrational state of the $X^1\Sigma_g^+$ , which is a good approximation for the free atoms wavefunction. In red, the states that can be accessed by the PA seed and amplifier tenability ranges (1060 to 1070 nm) are highlighted.	56
Figure 17 -	Scheme of a Franck-Condon map, where the Franck-Condon factors are plotted as a function of the vibrational quantum numbers of each potential involved in the process. For molecular potentials that have a single minimum, the most probable transitions (i.e., the highest FCFs) are located in the Condon Parabola.	57
Figure 18 -	Representation of the excitation light spectrum (left) and the Franck-Condon map for absorption of a photon by the molecules (right). The spectral shaping avoids any transition from the fundamental vibrational level of the ground potential.	58
Figure 19 -	A possible cycle of absorption and emission during the vibrational cooling process. In the absorption (fig. a1), the molecule is excited to a low-energy vibrational state of the excited potential (fig. a2). Then it spontaneously decay to the ground potential (figs. b1 and b2), either to the initial vibrational state (path ii) or to a lower energy state (path i). The net effect is to reduce the vibrational energy. The process ends when the molecule reaches the fundamental vibrational state, from which it cannot be excited.	59
Figure 20 -	Interaction potentials used in the vibrational cooling process.	60
Figure 21 -	Franck-Condon factors map for the two potentials used for the vibrational cooling. The red dashed line is the approximate spectral shaping cutoff of the broadband SLD, meaning that any transition above this line is inaccessible by the excitation light.	60
Figure 22 -	Schematic representation of the optical setup for photoassociation and vibrational cooling. The SLD is spectrally dispersed by a diffraction grating, and then the higher frequencies are removed by a blocker. The photoassociation laser has its frequency measured and controlled by a wavelength meter. Both beams are combined and injected on the YAR high power amplifier, which produces the ODT.	62
Figure 23 -	Combination of the photoassociation and vibrational cooling light sources, before (a) and after (b) amplification by the YAR amplifier. The cutoff frequency is chosen to be between 1042 nm and 1048 nm, corresponding to the transitions $v = 0 \rightarrow v' = 0$ and $v = 1 \rightarrow v' = 0$ respectively.	63
Figure 24 -	Rb2 potentials involved on the two-photon one-color REMPI (ionization) process.	64

Figure 25 - Franck-Condon map for the ionization process (REMPI). The red dashed lines mark approximately the transitions accessed during the measurements with our pulsed dye laser. The laser spectral range was chosen to reach some of the strongest transitions from the fundamental vibrational state $v = 0$ . ....	64
Figure 26 - Schematic representation of the REMPI experimental setup. The pulsed dye laser ionizes atoms and molecules in the sample, and each particle has a specific time-of-flight which depends on its mass. Each detected ion generates a pulse, which is viewed in an oscilloscope triggered by the laser pulses. This allows us to correlate the ions with the laser pulse times. ....	65
Figure 27 - Signal of the ion detector, as seen in the oscilloscope. The trigger is the laser pulse, and an average of 10 pulses is taken. The ratio between the molecular (b) and the atomic (b) peak delays is approximately $\sqrt{2}$ , which is in agreement with the square root of the mass scaling. ....	66
Figure 28 - Startup program interface. The program simply sets the controllable parameters to a constant value, which allows us to load a static MOT. ....	67
Figure 29 - LabVIEW program interface to control the REMPI experiment on the MOT.	68
Figure 30 - Representation of the periodic sequence for the REMPI experiment on the MOT. The first step is the MOT loading, with all parameters at MOT conditions. Following steps are the cooling of the MOT (to increase density) and the transference of the atoms to $F = 2$ , which allows the photoassociation. The ionization dye laser is then pulsed, generating the ions, with the MOT lights off. An extra time is given to ensure that the ionization will occur with no MOT lights. ....	69
Figure 31 - Front panel of the LabVIEW program to control the ODT loading sequence. Some of the parameters in this print may not be set to the actual values. ....	70
Figure 32 - Sequence of events for the loading and imaging of the optical dipole trap. After loading a MOT for some seconds, the parameters are changed in order to reduce the atoms' temperature. This allows for an efficient loading of the optical dipole trap. After this step, the repumping light is turned off to transfer the atoms for the $F = 2$ hyperfine level. The MOT is then turned off, leaving the atoms to be trapped only in the ODT. The ODT shape and population can be proved by a fluorescence image. ....	70
Figure 33 - Two examples of ODT images, showing a "bad" (a) and a "good" (b) trap. In a), only one of the beams are visible, meaning that the overlapping between the two arms is not correct. In b), the two arms are visible and a brighter spot at the center is present, indicating that the arms are correctly overlapped. ....	71
Figure 34 - Number $N$ of atoms in the ODT as a function of time, for $^{87}\text{Rb}$ (circles) and $^{85}\text{Rb}$ (squares) atoms. The solid line represents a curve fitting that considers both single-body and two-body losses, resulting in a clearly non-exponential decay. The two body losses can be explained by photoassociation. The inset	

	shows the temperature over time, and the nearly constant value indicates that no relevant losses due to thermalization occurred. ....	74
Figure 35 -	Trap loss spectra of the magneto-optical trap, as a function of the PA laser wavenumber. The measurements were performed both around $\nu' = 137$ (a) and $\nu' = 138$ (b) transitions. The negative peaks indicated by red arrows are attributed to the photoassociation by the high power laser. ....	75
Figure 36 -	Lifetime measurements performed with the new setup (using the YAR amplifier instead of the broadband laser). ....	76
Figure 37 -	Molecular ionization signal (REMPI) as a function of the photoassociation laser wavenumber, and comparison with the previously shown trap loss spectrum for $\nu' = 138$ . Each peak correspond to a different rotational state ( $J = 0$ and $J = 1$ ) from this vibrational quantum number. ....	77
Figure 38 -	Molecular ionization signal as a function of the PA laser intensity, which can be varied by changing the output power of the YAR amplifier. $I_0$ is the intensity that corresponds to the maximum output power of the YAR amplifier (50 W). The linear behavior is expected, as the PA is a single-photon mechanism. ....	79
Figure 39 -	Ionization signal as a function of the ionization laser power. The two-photon mechanism of the 1+1 REMPI process is compatible with the measured points. ....	80
Figure 40 -	Molecular ionization signal for REMPI laser wavelength scan, in the absence (a) and presence (b) of optical pumping by the shaped broadband SLD light. Notably, the number of peaks is smaller when the optical pumping is present, meaning that the number of occupied states is reduced in this case. ....	81
Figure 41 -	Comparison between the experimental spectrum (a) and a simulated spectrum (b), based on <i>ab initio</i> calculations performed by Dulieu's group. The simulation considers the vibrational distribution and the FCFs shown in figure 25 (section 4.3). Although the simulation could not reproduce the experimental spectrum (discussion in the text), some qualitative features such as peak density and average separation are similar. ....	82
Figure 42 -	Experimental vibrational spectrum with optical pumping. The wavelengths were converted to wavenumbers ( $1/\lambda$ ), and the peaks were labeled considering that, for each three consecutive transitions, one of them is missing due to low FCF. This behavior is qualitatively extracted from the Franck-Condon map. ....	84
Figure 43 -	Transition wavenumbers as a function of the quantum number, for both experimental spectrum (a) and theoretical data (b). The experimental slope of the line is of $11.9 \text{ cm}^{-1}$ , whereas the theoretical is of $10.0 \text{ cm}^{-1}$ , showing good agreement. The initial quantum number $\nu'_0$ is supposed unknown within the 50 – 100 range. ....	84

Figure 44 -	Control sequence of the proposed molecular loading experiment. The first stage is a normal MOT loading, keeping the parameters at constant MOT conditions. In the second stage, the YAR laser (PA/ODT) is turned on and the molecular signal is measured over time by REMPI pulses. At this stage, the MOT parameters are chopped according to figure 30 from section 4.4.2.	88
Figure 45 -	Control sequence of the molecular population decay in the ODT. The molecules are produced and transferred to the ODT in the first stage. In the second stage, the molecules are left at the ODT and should be lost with time.	88
Figure 46 -	Comparison between the experimental setup developed by Horchani (93) (a) and our similar proposal using two diffraction gratings (b). In both cases, the dispersed light is collimated by a cylindrical lens and then processed in the DLP mirror matrix, which discards the undesired spectral components. The mirror must be placed at a focal distance $f$ to the lens, in order to optimize the distinction between spectral components. ....	91
Figure 47 -	Schematic representation of the dispersion over the grating pair. $\phi$ is the angle between the normal vectors of the gratings. $\theta_1$ and $\theta_3$ are incidence angles, whereas $\theta_2$ and $\theta_4$ are diffraction angles. ....	92

## **LIST OF ABBREVIATIONS AND ACRONYMS**

AOM	Acousto-Optic Modulator
BDL	Broadband Diode Laser
BEC	Bose-Einstein Condensate
BO	Born-Oppenheimer
CW	Continuous Wave
DLP	Digital Light Processing
FCF	Franck-Condon Factor
FWHM	Full Width at Half Maximum
MA	Magnetoassociation
MOT	Magneto-Optical Trap
ODT	Optical Dipole Trap
PA	Photoassociation
REMPI	Resonance-Enhanced Multiphoton Ionization
SLD	Superluminescent Diode
STIRAP	Stimulated Raman Adiabatic Passage
TA	Tapered Amplifier



## CONTENTS

<b>1</b>	<b>INTRODUCTION .....</b>	<b>19</b>
<b>2</b>	<b>THEORETICAL BACKGROUND .....</b>	<b>23</b>
<b>2.1</b>	<b>Standard approach: Born-Oppenheimer Approximation .....</b>	<b>23</b>
<b>2.2</b>	<b>Nuclear vibration and rotation.....</b>	<b>28</b>
<b>2.3</b>	<b>The electronic levels and their nomenclature .....</b>	<b>29</b>
<b>2.4</b>	<b>Transition probabilities: Franck-Condon factors .....</b>	<b>31</b>
<b>3</b>	<b>LITERATURE REVIEW .....</b>	<b>35</b>
<b>3.1</b>	<b>Photoassociation: producing ultracold molecules .....</b>	<b>35</b>
<b>3.2</b>	<b>A counterpart to photoassociation: Feshbach molecules.....</b>	<b>38</b>
<b>3.3</b>	<b>Optical pumping to the vibrational ground state .....</b>	<b>39</b>
<b>4</b>	<b>EXPERIMENTAL SETUP.....</b>	<b>45</b>
<b>4.1</b>	<b>Atomic and molecular trapping and cooling.....</b>	<b>45</b>
<b>4.1.1</b>	<b>Vacuum system .....</b>	<b>45</b>
<b>4.1.2</b>	<b>The magneto-optical trap (MOT) .....</b>	<b>47</b>
<b>4.1.3</b>	<b>The optical dipole trap (ODT).....</b>	<b>49</b>
<b>4.1.4</b>	<b>Optical setup for MOT and ODT.....</b>	<b>52</b>
<b>4.2</b>	<b>Production and manipulation of molecules.....</b>	<b>54</b>
<b>4.2.1</b>	<b>Photoassociation .....</b>	<b>55</b>
<b>4.2.2</b>	<b>Vibrational cooling .....</b>	<b>56</b>
<b>4.2.3</b>	<b>Optical setup for photoassociation and vibrational cooling .....</b>	<b>61</b>
<b>4.3</b>	<b>The REMPI detection technique.....</b>	<b>63</b>
<b>4.4</b>	<b>Control of the experiment.....</b>	<b>67</b>
<b>4.4.1</b>	<b>“Startup” – constant parameters .....</b>	<b>67</b>
<b>4.4.2</b>	<b>REMPI experiments control sequence .....</b>	<b>68</b>
<b>4.4.3</b>	<b>Optical dipole trap loading and imaging.....</b>	<b>69</b>
<b>5</b>	<b>RESULTS AND DISCUSSION.....</b>	<b>73</b>
<b>5.1</b>	<b>Preliminary results .....</b>	<b>73</b>
<b>5.2</b>	<b>Ionization spectrum as function of the photoassociation laser wavenumber .....</b>	<b>76</b>
<b>5.3</b>	<b>Molecular signal as a function of PA and REMPI laser intensities .....</b>	<b>78</b>
<b>5.4</b>	<b>Molecular spectra as a function of the REMPI laser wavelength.....</b>	<b>80</b>
<b>5.5</b>	<b>Discussion about the vibrational cooling.....</b>	<b>83</b>

<b>6</b>	<b>FUTURE PERSPECTIVES .....</b>	<b>87</b>
<b>6.1</b>	<b>Loading and losses of molecules in the ODT .....</b>	<b>87</b>
<b>6.2</b>	<b>KRb molecules.....</b>	<b>89</b>
<b>6.3</b>	<b>Rotational cooling by optical pumping .....</b>	<b>89</b>
<b>7</b>	<b>CONCLUSIONS .....</b>	<b>95</b>
	<b>REFERENCES.....</b>	<b>97</b>
	<b>APPENDIX A – Justification of the “1/2” factor on the optical dipole force.....</b>	<b>105</b>
	<b>APPENDIX B – Proof of the angular dispersion equation .....</b>	<b>107</b>

## 1 INTRODUCTION

The matter and its complexity has always intrigued the humanity, and is one of the main motivations behind the study of physics and chemistry. In the western History, many philosophers from ancient Greece have proposed theories to describe matter, such as Thales and his hypothesis that everything was formed by water, Democritus and Leucippus with the atomism (1), Aristotle's four elements and many others. (2) The atomism from Democritus and Leucippus was a philosophical hypothesis that the matter is composed of several elementary and indivisible components, and only received a modern scientific version in the first decade of the 19<sup>th</sup> century, after John Dalton proposed his atomic model based on previous observations. This model allowed the atomic conception of matter to be tested, and with this it began to win credibility from the scientists. After little improvement during the rest of the 19<sup>th</sup> century, the atomic model passed through an intense development in the first decade of the 20<sup>th</sup> century, when scientists found out that many phenomena that occur with matter could not be explained by the classical laws of physics, giving rise to quantum mechanics. Since then, the study of matter have been divided into some of the current research areas of physics, such as condensed matter physics, atomic and molecular physics, and particle physics.

The present dissertation belongs to the atomic and molecular physics field, which studies the matter by its individual reactive components: atoms and molecules. Until the 1980 decade, many works in atomic physics were mainly developed using thermal samples. (3) However, it was known that the main quantum features of the matter should only appear at very low temperatures since the early development of quantum mechanics, exemplified by the prediction of Bose-Einstein condensation in 1925 (4) and the Cooper pairs theory to explain superconductivity in 1956. (5) In 1975, the idea of atomic *laser cooling* was introduced by Hänsch and Schawlow (6); its potential to achieve temperatures of fractions of Kelvin have attracted strong efforts to its experimental realization. The first experimental achievements of laser cooling came in the 1980 years, with the first Zeeman slower in 1982 (7) and the first *magneto-optical trap* (MOT) in 1987. Several other new techniques were developed at this time, such as the magnetic trap in 1985 (8) and the optical trap in 1986. (9) The development of all these techniques transformed the physics of ultracold atoms in a very strong research area since then. All of this belongs to that ancient and same effort to understand the matter and its phenomenology.

Until the present moment, all the techniques for reaching ultracold temperatures are strongly dependent on the atomic species, and mostly developed with alkaline and alkaline earth

metals. Due to this fact, studying systems that are more complex than simple atoms is very important, and this has been developed along with the atomic physics itself. Rydberg atoms (10-11) and ultracold molecules (12-13) are examples of such alternatives, due to their rich structures and special properties that cannot be found in normal atoms.

Ultracold diatomic molecules have a very wide spectrum of applications. Their complexity give rise to new phenomena that are not present in single atoms, but they are still simple enough to be produced, trapped and manipulated in laboratory with the currently existing techniques. Many important applications of ultracold molecules lie in the fundamental physics domain. For example, the rotational levels of diatomic molecules were used to search for violations of parity symmetry with a precision of  $10^{11}$  times greater than in atoms. (14) CP symmetry tests are also being performed with the search of a possible electric dipole moment on electrons. (15) Several experiments have been proposed in order to detect possible variations of fundamental constants over time, such as the hyperfine structure constant ( $\alpha$ ) and the electron to proton mass ratio ( $m_e/m_p$ ). (16) Review papers on ultracold molecules and fundamental physics tests can be found in (17), (18) and (19). These applications into fundamental physics are possible due to the ultraprecise measurements that can be performed with molecules.

Besides the test of physical constants and symmetries, many other scientific and technologic applications are possible with ultracold molecules. Heteronuclear molecules are highly controllable by external fields, due to their permanent electric dipole moment. This allows, for example, the realization of controlled ultracold chemical reactions (20), in which the reaction rates can be sensibly controlled by changing the orientation of the molecular moments. Polar molecules are also good candidates for qbits, opening possibilities to quantum computation. There are several proposals to this application (21-23), which basically rely on the controllability of molecular states by external fields. Other applications include simulation of condensed matter systems (24), quantum phase transitions (25), high resolution spectroscopy (26) and others. (19)

For most of the applications, the control of the rotational and vibrational states is important, or even essential. The present dissertation is based in an experimental work related to this procedure of controlling internal degrees of freedom of the molecules. In particular, we manipulate the vibrational states of  $\text{Rb}_2$  molecules.

The goals of our work, in a first stage, are the following: (i) produce  $\text{Rb}_2$  and molecules through photoassociation; (ii) transfer a macroscopic fraction of the molecular population to the fundamental vibrational level ( $\nu = 0$ , where  $\nu$  is the vibrational quantum number) by optical

pumping; (iii) trap the  $\nu = 0$  molecules in an *optical dipole trap* (ODT). Most of the concepts related to these procedures are explained throughout the dissertation. It should be also mentioned that we have the same goals for the KRb molecule, which have particular interest because it is heteronuclear. However, the present work is related only to the goals i) and ii) for Rb<sub>2</sub> molecules.

As a long term goal, we expect to use the produced molecular sample to study cold collisions involving atoms and molecules, as well as molecules only. This goal is based in some previous works, such as the cold collisions experiment developed by Staunum and co-workers (27) for Cs<sub>2</sub> molecules.

This dissertation is divided as the following. In the Theoretical Background (chapter 2) we discuss fundamental concepts of the molecular theory under the scope of the Born-Oppenheimer approximation. This is the standard approach that is given to diatomic molecules, and has proven to be very effective in a wide range of situations. To complement the initial considerations of this work, chapter 3 presents a brief review of some articles related to molecular production and manipulation. Among the literature review itself, the basic theory of photoassociation and optical pumping (the two techniques that we use respectively to produce and control the molecules) is also presented.

The methodology is described in chapter 4 – the “Experimental setup” chapter. As it is naturally expected from an experimental work, this is the largest chapter, and contains a detailed description of each part of the experiment that is relevant to this work. Some parts, such as the vacuum system and the magneto-optical trap, are essential to the experiment itself, and were already implemented when the author started to work on the group. Some other parts were partially or completely implemented during the time of this master course, such as the photoassociation and vibrational cooling setups. Special attention is given to these parts, as they are more specific to this work.

The results are presented and discussed in chapter 5. They are mainly related to the experimental proof of the photoassociation and vibrational cooling processes in our experiment, with the setup that we have proposed. The results are, when possible, compared to previous experiments performed in our group or theoretical calculations, mainly provided by our collaborators from the group of Olivier Dulieu and Nadia Bouloufa-Maafa, from *Université Paris-Sud* in France. After the results section, a special chapter is dedicated to our future works perspectives (chapter 6). A single chapter is allocated to this part mainly because we propose an experimental setup to promote also the rotational cooling in our system. Finally (and naturally), the work is reviewed and closed in the “Conclusions” chapter.



## 2 THEORETICAL BACKGROUND

In this section, we discuss basic theoretical topics about molecular quantum theory. These topics are important for the design of our experiment, as well as the understanding of our results. Most of the theoretical principles discussed here are valid for any molecular system, but a special emphasis will be given to diatomic molecules.

Section 2.1 covers the standard approach to solve Schrödinger equation for molecular systems. The method will be explained for a generic situation, and the validity of this approximation will be discussed briefly. Section 2.2 is dedicated specifically to diatomic molecules, and does provide an explanation for the separation between vibrational and rotational motions. Section 2.3 is dedicated to the electronic levels and their nomenclature in the most common case. Finally, in section 2.4, we discuss radiative transitions between different electronic levels, with an emphasis on the intensity differences between the various vibrational levels.

### 2.1 Standard approach: Born-Oppenheimer Approximation

In molecular dynamics, it is common to consider two atoms (more precisely, two nuclei) moving in the action of an “electronic potential”. This argument is based on the *Born-Oppenheimer* (BO) *approximation*, which relies on an adiabatic consideration. According to this approximation, it is possible to decouple the nuclear and the electronic motions, making the originally difficult many-body problem considerably simpler. Here, we do not present all the necessary arguments to justify the approximation, but some important remarks (that are often omitted) will be made.

We begin with the general problem of  $A$  nuclei, indexed by  $a = 1, 2, \dots, A$ , with masses  $M_a$  and atomic numbers  $Z_a$ , and  $I$  electrons indexed by  $i = 1, 2, \dots, I$ . In a fixed Cartesian coordinate system, the positions of the nuclei and the electrons are respectively  $\mathbf{R}_a$  and  $\mathbf{r}_i$ . The exact Hamiltonian of the system, in CGS units, is given by:

$$\begin{aligned}
 H = & \sum_i \sum_\beta -\frac{\hbar^2}{2m} \frac{\partial^2}{\partial r_{i,\beta}^2} + \sum_a \sum_\beta -\frac{\hbar^2}{2M_a} \frac{\partial^2}{\partial R_{a,\beta}^2} + \sum_{i < j} \frac{e^2}{|\mathbf{r}_i - \mathbf{r}_j|} + \sum_{a < b} \frac{Z_a Z_b e^2}{|\mathbf{R}_a - \mathbf{R}_b|} + \\
 & + \sum_{i,a} -\frac{Z_a e^2}{|\mathbf{R}_a - \mathbf{r}_i|}
 \end{aligned} \tag{1}$$

Here  $e$  is the electron charge (in CGS),  $\hbar$  is the Plank constant divided by  $2\pi$ ,  $m$  is the electron mass and  $\beta$  is an index for each of the three Cartesian directions  $x, y, z$ . We conveniently separate the Hamiltonian in two parts, one for the nuclei and other for the electron, as follows:

$$H = H_e + H_n \quad (2)$$

$$H_e = T_e + V_{ee} + V_{ne} \quad (3)$$

$$H_n = T_n + V_{nn} \quad (4)$$

Where:

$$T_e = \sum_i \sum_{\beta} -\frac{\hbar^2}{2m} \frac{\partial^2}{\partial r_{i,\beta}^2} \quad (5)$$

$$V_{ee} = \sum_{i<j} \frac{e^2}{|\mathbf{r}_i - \mathbf{r}_j|} \quad (6)$$

$$V_{ne} = \sum_{i,a} -\frac{Z_a e^2}{|\mathbf{R}_a - \mathbf{r}_i|} \quad (7)$$

Are respectively the electronic kinetic energy, the Coulomb interactions between electrons and the Coulomb interactions between electrons and nuclei. Similarly, we define:

$$T_n = \sum_a \sum_{\beta} -\frac{\hbar^2}{2M_a} \frac{\partial^2}{\partial R_{a,\beta}^2} \quad (8)$$

$$V_{nn} = \sum_{a<b} \frac{Z_a Z_b e^2}{|\mathbf{R}_a - \mathbf{R}_b|} \quad (9)$$

As the nuclear kinetic energy and the Coulomb interactions between nuclei, respectively. The BO approximation is frequently justified as follows: the mass of each nucleus is always much larger (at least 2000 times) than the electron mass, so the nuclear motion is much *slower* than the electronic motion. This allows us to separate the total wavefunction into two factors, one nuclear and the other electronic, and solve the electronic problem considering that the nuclei are all fixed in space; the result is then used to calculate the nuclear motion itself. This argument, however, is not physically precise, because it relies on the classical idea of

trajectories when considers that the nuclei are *slow* and electrons are *fast*. A mathematical argument based on quantum mechanics is therefore required. Here, we indicate the path for this argumentation, but the rigorous justification (and its corrections) goes beyond the scope of this work.

Let us begin with the exact solutions to the electronic problem with fixed nuclei. Henceforth, we shall denote by  $\mathbf{R}$  and  $\mathbf{r}$  all the nuclear and electronic coordinates, respectively.

$$H_e \chi_k(\mathbf{r}; \mathbf{R}) = \varepsilon_k(\mathbf{R}) \chi_k(\mathbf{r}; \mathbf{R}) \quad (10)$$

The semicolon means that the nuclear positions  $\mathbf{R}$  participate on the solution as parameters, not variables. The different solutions are indexed with  $k$ , and form a complete orthonormal basis under integration on  $\mathbf{r}$ , this is:

$$\langle \chi_{k'}(\mathbf{R}) | \chi_k(\mathbf{R}) \rangle = \int \chi_{k'}^*(\mathbf{r}; \mathbf{R}) \chi_k(\mathbf{r}; \mathbf{R}) d\mathbf{r} = \delta_{k',k} \quad (11)$$

For each  $k$ , we propose (as an *ansatz*) that the solution for the complete problem can be found by simply multiplying  $\chi_k(\mathbf{r}; \mathbf{R})$  by another function  $\phi(\mathbf{R})$  (the nuclear wavefunction)\*. We therefore want to use:

$$\Psi_k(\mathbf{r}, \mathbf{R}) = \phi_k(\mathbf{R}) \chi_k(\mathbf{r}; \mathbf{R}) \quad (12)$$

To solve the time-independent Schrödinger equation:

$$H\Psi(\mathbf{r}, \mathbf{R}) = E \Psi(\mathbf{r}, \mathbf{R}) \quad (13)$$

$$[H_n + H_e] \phi_k(\mathbf{R}) \chi_k(\mathbf{r}; \mathbf{R}) = E \phi_k(\mathbf{R}) \chi_k(\mathbf{r}; \mathbf{R}) \quad (14)$$

$$H_n \phi_k(\mathbf{R}) \chi_k(\mathbf{r}; \mathbf{R}) + \varepsilon_k(\mathbf{R}) \phi_k(\mathbf{R}) \chi_k(\mathbf{r}; \mathbf{R}) = E \phi_k(\mathbf{R}) \chi_k(\mathbf{r}; \mathbf{R}) \quad (15)$$

We confirm the validity of the separation *ansatz* on equation 12 if the electronic function  $\chi_k(\mathbf{r}; \mathbf{R})$  can be factorized on equation 15, yielding a purely nuclear equation. We must then study the action of  $H_n$  in  $\phi_k(\mathbf{R}) \chi_k(\mathbf{r}; \mathbf{R})$ , because it is a differential operator and can change

---

\* For a *general* solution of the equation, it should be written as a linear combination of all  $\chi_k$ . However, nothing is lost in our analysis using a single function.

the functional form of  $\chi_k(\mathbf{r}; \mathbf{R})$ , thus avoiding the desired factorization. Using the definition  $H_n = T_n + V_{nn}$  (from equation 4):

$$H_n \phi_k(\mathbf{R})\chi_k(\mathbf{r}; \mathbf{R}) = [T_n + V_{nn}(\mathbf{R})] \phi_k(\mathbf{R})\chi_k(\mathbf{r}; \mathbf{R}) \quad (16)$$

$V_{nn}(\mathbf{R})$  is not a problem, because it is not a differential operator and leaves  $\chi_k(\mathbf{r}; \mathbf{R})$  unchanged; we must then focus on the action of  $T_n$ , the nuclear kinetic energy. Using the definition on equation 8 and applying Leibniz differentiation rule for second derivatives:

$$\begin{aligned} T_n \phi_k(\mathbf{R})\chi_k(\mathbf{r}; \mathbf{R}) &= \sum_a \sum_\beta -\frac{\hbar^2}{2M_a} \frac{\partial^2}{\partial R_{a,\beta}^2} [\phi_k(\mathbf{R})\chi_k(\mathbf{r}; \mathbf{R})] = \\ &= \sum_a \sum_\beta -\frac{\hbar^2}{2M_a} \left\{ \frac{\partial^2 \phi_k(\mathbf{R})}{\partial R_{a,\beta}^2} \chi_k(\mathbf{r}; \mathbf{R}) + 2 \frac{\partial \phi_k(\mathbf{R})}{\partial R_{a,\beta}} \frac{\partial \chi_k(\mathbf{r}; \mathbf{R})}{\partial R_{a,\beta}} + \right. \\ &+ \left. \phi_k(\mathbf{R}) \frac{\partial^2 \chi_k(\mathbf{r}; \mathbf{R})}{\partial R_{a,\beta}^2} \right\} \end{aligned} \quad (17)$$

The two last terms on equation 17 contain derivatives of the electronic function  $\chi_k(\mathbf{r}; \mathbf{R})$  on the nuclear coordinates. This prevents the factorization of the electronic part on equation 15, meaning that the electronic and nuclear motions are coupled. The Born-Oppenheimer approximation consists into completely neglecting these two terms containing nuclear derivatives of the electronic functions. In their original article (28), Born and Oppenheimer showed that this is a good approximation for stable diatomic molecules, though using a different approach. Unfortunately, for the general case, it is very difficult to find a strong argument justifying the approximation throughout the available literature. Yet a relatively simple analysis can be done, following this reference (29), to show when the BO approximation breaks down.

To make this analysis, first consider the expansion of  $\partial \chi_k(\mathbf{r}; \mathbf{R}) / \partial R_{a,\beta}$  again in the electronic states basis:

$$\frac{\partial \chi_k(\mathbf{r}; \mathbf{R})}{\partial R_{a,\beta}} = \sum_{k'} \chi_{k'}(\mathbf{r}; \mathbf{R}) \left\langle \chi_{k'}(\mathbf{R}) \left| \frac{\partial}{\partial R_{a,\beta}} \right| \chi_k(\mathbf{R}) \right\rangle \quad (18)$$

Where:

$$\left\langle \chi_{k'}(\mathbf{R}) \left| \frac{\partial}{\partial R_{a,\beta}} \right| \chi_k(\mathbf{R}) \right\rangle = \int \chi_{k'}^*(\mathbf{r}; \mathbf{R}) \frac{\partial \chi_k(\mathbf{r}; \mathbf{R})}{\partial R_{a,\beta}} d\mathbf{r} \quad (19)$$

Are the expansion coefficients. Considering only the off-diagonal terms (i.e. for which  $k \neq k'$ ), we can use the commutation of the operator  $\partial/\partial R_{a,\beta}$  with the electronic Hamiltonian  $H_e$  to obtain:

$$\left\langle \chi_{k'}(\mathbf{R}) \left| \frac{\partial}{\partial R_{a,\beta}} \right| \chi_k(\mathbf{R}) \right\rangle = \frac{\left\langle \chi_{k'}(\mathbf{R}) \left| \left[ H_e, \frac{\partial}{\partial R_{a,\beta}} \right] \right| \chi_k(\mathbf{R}) \right\rangle}{\varepsilon_{k'}(\mathbf{R}) - \varepsilon_k(\mathbf{R})} \quad (20)$$

It is possible to notice that this term diverges if  $E_{k'}(\mathbf{R}) = E_k(\mathbf{R})$ , i.e., two electronic levels are close to each other for a certain  $\mathbf{R}$ . Therefore, the BO approximation is not valid for level crossing situations. In general, for diatomic molecules, this is not the case for a large domain on  $\mathbf{R}$  (30-31). Corrections for the BO approximation involve the evaluation of the matrix elements defined on equation 19, as well as for the second derivatives  $\partial^2 \chi_k(\mathbf{r}; \mathbf{R}) / \partial R_{a,\beta}^2$ . (32)

To conclude our analysis, we return to the Schrödinger equation (eq. 15) considering the BO approximation, i.e., neglecting the two last terms on the RHS of equation 17:

$$\begin{aligned} [T_n \phi_k(\mathbf{R})] \chi_k(\mathbf{r}; \mathbf{R}) + V_{nn}(\mathbf{R}) \phi_k(\mathbf{R}) \chi_k(\mathbf{r}; \mathbf{R}) + \varepsilon_k(\mathbf{R}) \phi_k(\mathbf{R}) \chi_k(\mathbf{r}; \mathbf{R}) = \\ = E \phi_k(\mathbf{R}) \chi_k(\mathbf{r}; \mathbf{R}) \end{aligned} \quad (21)$$

Finally by factorizing and eliminating  $\chi_k(\mathbf{r}; \mathbf{R})$  on both sides, we get the wave equation for the nuclear wavefunction:

$$[T_n + V_{nn}(\mathbf{R}) + \varepsilon_k(\mathbf{R})] \phi_k(\mathbf{R}) = E \phi_k(\mathbf{R}) \quad (22)$$

In this equation, the only contribution of the electronic motion is to change the effective nuclear potential as follows:

$$V_n(\mathbf{R}) = V_{nn}(\mathbf{R}) + \varepsilon_k(\mathbf{R}). \quad (23)$$

Summarizing the procedure: we first solve the electronic equation 10 to find the electronic levels  $\varepsilon_k(\mathbf{R})$  for static nuclei. These levels are used to solve the nuclear equation 22.

## 2.2 Nuclear vibration and rotation

For diatomic molecules, the nuclear equation is a two-body problem with a central interaction. It can be largely simplified by introducing the *center of mass* and *relative* coordinates as follows: (33)

$$\mathbf{R}_{\text{CM}} = \frac{M_1 \mathbf{R}_1 + M_2 \mathbf{R}_2}{M_1 + M_2} \quad (24)$$

$$\mathbf{R}_{\text{rel}} = \mathbf{R}_1 - \mathbf{R}_2 \quad (25)$$

In this system, the center of mass position  $\mathbf{R}_{\text{CM}}$  corresponds to the translational movement, responding only to external potentials, whereas the relative coordinate  $\mathbf{R}_{\text{rel}}$  represents the vibrations and rotations of the molecule. The equation for  $\mathbf{R}_{\text{rel}}$  (which for diatomic molecules we will call simply  $\mathbf{R}$ ) is similar to eq. 22, using the reduced mass of the system:

$$\left[ -\frac{\hbar^2}{2\mu} \nabla^2 + V_n(\mathbf{R}) \right] \phi_k(\mathbf{R}) = E \phi_k(\mathbf{R}) \quad (26)$$

$$\mu = \frac{M_1 M_2}{M_1 + M_2} \quad (27)$$

The potential  $V_n(\mathbf{R})$  is actually spherically symmetric, so we have a typical central potential problem. By decomposing  $\mathbf{R}$  in its spherical coordinates  $(R, \theta, \varphi)$ , we can separate the wavefunction  $\phi_k(\mathbf{R})$  in radial and angular parts (equation 28), obtaining an effective radial equation: (34)

$$\phi_k(\mathbf{R}) = \frac{u(R)}{R} Y_J^{M_J}(\theta, \varphi) \quad (28)$$

$$\left[ -\frac{\hbar^2}{2\mu} \frac{\partial^2}{\partial R^2} + V_n(R) + \frac{\hbar^2}{2\mu} \frac{J(J+1)}{R^2} \right] u(R) = E u(R) \quad (29)$$

Here  $Y_J^{M_J}(\theta, \varphi)$  are the spherical harmonics, and  $J$  is the rotational angular momentum quantum number of the molecule<sup>†</sup>. An important remark should be made at this point, as we are not considering any spin interaction or internal magnetic coupling on the molecule. Depending on the situation, these interactions can be relevant enough to make  $J$  a bad quantum number, thus requiring considerable corrections. Different coupling situations are studied on the so called *Hund's cases* (see section 6.7 on (35)). For us, it is enough to know that the problem is well described by the nuclear relative distance  $R$ , regardless of the possible complications (section 6.2.2 on (35)).

Solving the radial equation 29 for different values of  $J$  will give the energy levels and radial wavefunctions of the diatomic system. For typical potentials  $V_n(R)$  which have one stable equilibrium point, the bound states are called *vibrational levels*, resembling the classical idea of oscillatory motion. One interesting fact is that the energy scale of the centrifugal term  $\hbar^2/2\mu R^2$  is typically much smaller than the separation between vibrational levels. (36) For this reason, the rotational levels are considered energy branches of the vibrational levels.

### 2.3 The electronic levels and their nomenclature

As we discussed on section 2.1, the solutions for the electronic equation 10 yields different electronic levels as functions of nuclear coordinates, which then are used to calculate the nuclear potential curves. For diatomic molecules, the only relevant variable to the potential curves is the internuclear separation  $R$ .

In practice, for molecules formed by multi-electronic atoms, the solution of the electronic equation with purely theoretical methods is very difficult. The potential curves are then reconstructed using experimental data of the vibrational levels. Another approach is to consider “model potentials”, which are analytical expressions for  $V_n(R)$  that are fitted with parameters found from spectroscopic observations. This last approach is called *ab initio* method, and usually is not as precise as the first one. Examples of potential curves are shown in Figure 1, for the  $\text{Rb}_2$  molecule.

---

<sup>†</sup> In the literature,  $J$  is used to represent the *total* angular momentum of the molecule (including electronic orbital momentum and spin), and  $R$  is the quantum number for the nuclear rotation (35). However, we do not want to confuse this with the relative distance  $R$ .

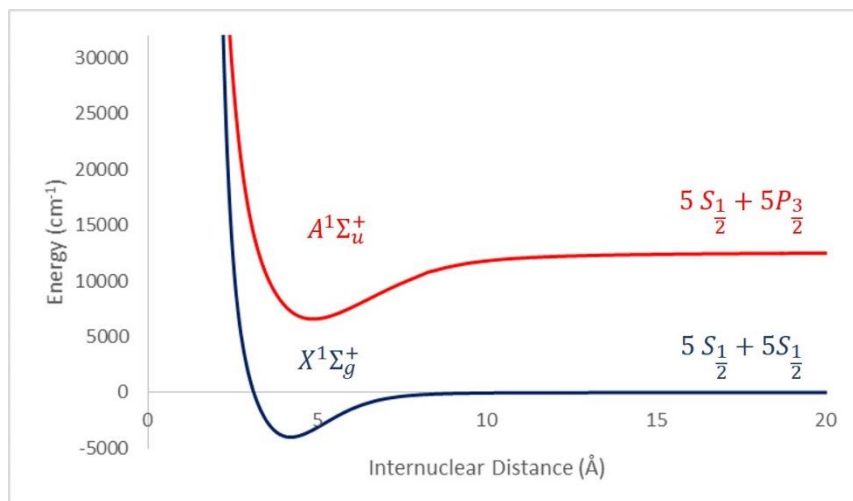


Figure 1 – Examples of potential curves constructed with spectroscopic data from  $\text{Rb}_2$  molecules. In this case, each curve contains one stable equilibrium point, meaning that bound states are allowed.  
Source: By the author.

Each potential curve receives a nomenclature, according to the characteristics of its electronic wavefunction (or, similarly, the quantum numbers that describe it). One interesting fact is that the nomenclature of a single potential is not the same for different ranges on the internuclear distance  $R$ . This happens because the intensity of internal interactions (like spin-orbit coupling or electrostatic and magnetic interactions) may vary with  $R$ , meaning that the good quantum numbers are not always the same. For instance, when the two atoms are apart from one another, the interaction between them is negligible. The potential is then nominated  $A + B$ , where  $A$  and  $B$  are simply atomic term symbols representing the states of each individual atom. Examples in Figure 1 for rubidium are  $5 S_{1/2} + 5 S_{1/2}$  and  $5 S_{1/2} + 5 P_{3/2}$ .

For shorter internuclear distances, the most common case that we work with is the Hund's case (b), for which the spin-orbit coupling is weak when compared to the coupling of the electronic orbital angular momentum with the internuclear axis (see (35) and (37)). This coupling is due to the very strong electrostatic field generated by the nuclei. The electronic orbital angular momentum  $L$  itself is not a good quantum number, but its projection  $M_L$  on the internuclear axis is. The energy levels with  $M_L$  and  $-M_L$  are degenerate (see section 1 of (38)), so it is convenient to define the non-negative quantum number:

$$\Lambda = |M_L| \quad (30)$$

It can assume values  $\Lambda = 0, 1, 2, \dots$ , which are respectively attributed to the capital Greek letters  $\Sigma, \Pi, \Delta, \dots$ , in analogy to atomic orbitals. Moreover, the electronic total spin  $S$  is also a good quantum number, assuming the value  $1/2$  for one electron,  $1$  or  $0$  for two electrons, and so on. The molecular electronic states are then labeled by the *molecular term symbol*:

$${}^{2S+1}\Lambda_{g,u}^{+,-} \quad (31)$$

The number  $\Lambda$  is represented by its Greek letter, and  $2S + 1$  is the electronic multiplicity. The upper right superscript stands for the reflection symmetry of the wavefunction by a plan that contains the internuclear axis<sup>‡</sup>, being “+” for even wavefunctions and “-” for odd ones. The subscript “g,u” (from the German words *gerade* and *ungerade*) applies only to homonuclear molecules, which also presents point symmetry with respect to the geometrical center between the nuclei. It appears as “g” (*gerade*) for even wavefunctions and “u” (*ungerade*) for odd wavefunctions. It is also usual to add a capital letter before the term symbol itself, which is  $X$  for the fundamental level, and  $A, B, C, \dots$  in crescent order of energy for each spin multiplicity. Two examples of this nomenclature are visible in figure 1.

## 2.4 Transition probabilities: Franck-Condon factors

Here we describe the theory of radiative transitions between molecular electronic states, which plays a major role in our experimental work. This description is based on section 6.11 of (35) and section 4 of (39). The basis for studying transition intensities between molecular states is the *Franck-Condon principle*. It was first stated by James Franck in 1926 (40) in a classical and qualitative way, and then enhanced by Edward U. Condon in 1928 (41), who included quantum mechanics concepts and mathematical expressions. The classical statement of the principle can be written as follows: “The electron jump in a molecule (during a transition) takes place so rapidly in comparison to the nuclear motion that, immediately afterwards, the nuclei still have nearly the same relative positions and velocities as before the jump.” (39)

With this simple qualitative assumption, it is possible to determine some transitions that are more likely (or *stronger*) than others. This is illustrated for a diatomic molecule in Figure 2. The transition iii) requires a big change on the internuclear distance, whereas transition ii)

---

<sup>‡</sup> Due to the cylindrical symmetry of any diatomic molecule, every electronic wavefunction is either even or odd by this reflection.

requires a big change in nuclear kinetic energy (the distance between the vibrational level and the potential curve); both are weak transitions. Transition i), on the other hand, preserves nuclear position and momentum, and therefore is stronger than the others.

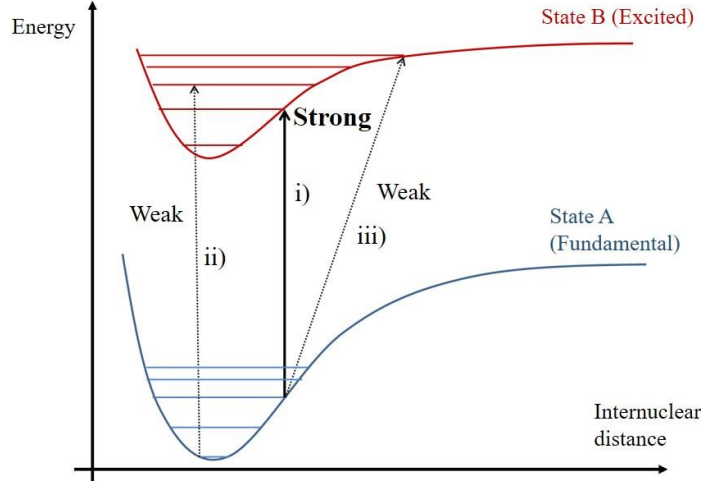


Figure 2 – Representation of the classical statement of Franck-Condon principle. Transition i) is strong (more likely) because it preserves nuclear relative position and velocity. Transitions ii) and iii) are weak (less likely), as they change the velocity and the position of the nuclei, respectively.

Source: By the author.

With the use of quantum mechanics, it is possible to calculate the transition probabilities between different electronic (and vibrational) levels. We are not interested in their exact values, but their relative intensities between different vibrational levels are of interest for our work.

Radiative transitions are determined by the matrix elements of the dipole operator  $\boldsymbol{\mu}$ , defined as follows:

$$[\boldsymbol{\mu}]_{f,i} = \iint \Psi_f^*(\mathbf{r}, \mathbf{R}) \boldsymbol{\mu} \Psi_i(\mathbf{r}, \mathbf{R}) \, d\mathbf{r} \, d\mathbf{R} \quad (32)$$

The subscripts  $i$  and  $f$  denote “initial” and “final” states, respectively, and the integration is over all nuclear and electronic coordinates. In the scope of BO approximation, we open the dipole operator  $\boldsymbol{\mu}$  and the total wavefunctions in their nuclear and electronic parts:

$$\boldsymbol{\mu} = e \left( \sum_a Z_a \mathbf{R}_a - \sum_j \mathbf{r}_j \right) \quad (33)$$

$$\Psi_f(\mathbf{r}, \mathbf{R}) = \phi_f(\mathbf{R}) \chi_f(\mathbf{r}; \mathbf{R}) \quad (34)$$

$$\Psi_i(\mathbf{r}, \mathbf{R}) = \phi_i(\mathbf{R}) \chi_i(\mathbf{r}; \mathbf{R}) \quad (35)$$

The notation follows the same as in section 2.1, except for the electronic index  $j$ , to avoid confusion with the “initial state” index  $i$ . Substituting the equations 33, 34 and 35 into equation 32, we obtain:

$$\begin{aligned}
[\boldsymbol{\mu}]_{f,i} &= \iint \phi_f^*(\mathbf{R}) \chi_f^*(\mathbf{r}; \mathbf{R}) e\left(\sum_a Z_a \mathbf{R}_a - \sum_j \mathbf{r}_j\right) \phi_i(\mathbf{R}) \chi_i(\mathbf{r}; \mathbf{R}) \, d\mathbf{r} \, d\mathbf{R} = \\
&= \iint \phi_f^*(\mathbf{R}) \chi_f^*(\mathbf{r}; \mathbf{R}) e\left(\sum_a Z_a \mathbf{R}_a\right) \phi_i(\mathbf{R}) \chi_i(\mathbf{r}; \mathbf{R}) \, d\mathbf{r} \, d\mathbf{R} - \\
&\quad - \iint \phi_f^*(\mathbf{R}) \chi_f^*(\mathbf{r}; \mathbf{R}) e\left(\sum_j \mathbf{r}_j\right) \phi_i(\mathbf{R}) \chi_i(\mathbf{r}; \mathbf{R}) \, d\mathbf{r} \, d\mathbf{R}
\end{aligned} \tag{36}$$

We can now make use of the Born-Oppenheimer approximation to withdraw the electronic wavefunctions from the nuclear integral. For this, recover from section 2.1 that the BO approximation consists into neglecting the derivatives  $\partial \chi_k(\mathbf{r}; \mathbf{R}) / \partial R_{\alpha,\beta}$  of the electronic functions in the nuclear coordinates. This means that, inside the integration region (i.e., where the nuclear wavefunctions are appreciable), both  $\chi_i(\mathbf{r}; \mathbf{R})$  and  $\chi_f^*(\mathbf{r}; \mathbf{R})$  are effectively constant, and can be replaced by  $\chi_i(\mathbf{r}; \bar{\mathbf{R}})$  and  $\chi_f^*(\mathbf{r}; \bar{\mathbf{R}})$ , where  $\bar{\mathbf{R}}$  denotes a fixed point in the molecular range and whose exact value is not important for this calculation<sup>§</sup>. This approximation holds as long as the appreciable range of the nuclear wavefunctions is not too wide. Using this fact to factorize the electronic part from the nuclear integral:

$$\begin{aligned}
[\boldsymbol{\mu}]_{f,i} &= e \int \chi_f^*(\mathbf{r}; \bar{\mathbf{R}}) \chi_i(\mathbf{r}; \bar{\mathbf{R}}) \, d\mathbf{r} \cdot \int \phi_f^*(\mathbf{R}) \left(\sum_a Z_a \mathbf{R}_a\right) \phi_i(\mathbf{R}) \, d\mathbf{R} - \\
&\quad - e \int \chi_f^*(\mathbf{r}; \bar{\mathbf{R}}) \left(\sum_j \mathbf{r}_j\right) \chi_i(\mathbf{r}; \bar{\mathbf{R}}) \, d\mathbf{r} \cdot \int \phi_f^*(\mathbf{R}) \phi_i(\mathbf{R}) \, d\mathbf{R}
\end{aligned} \tag{37}$$

---

<sup>§</sup> Notice that the value is not necessarily the same for each function, thus this is a notation abuse. However, as it was mentioned, the value itself is not important, but only the fact that the functions can be withdrawn from the nuclear integral.

The first integral on the first term of equation 37 is an electronic integral over *different* electronic states. Due to the orthogonality of these functions (equation 11), this terms vanishes.

We then obtain:

$$[\boldsymbol{\mu}]_{f,i} = [\boldsymbol{\mu}_e]_{f,i} \cdot \int \phi_f^*(\mathbf{R}) \phi_i(\mathbf{R}) d\mathbf{R} \quad (38)$$

Where:

$$[\boldsymbol{\mu}_e]_{f,i} = -e \int \chi_f^*(\mathbf{r}; \bar{\mathbf{R}}) \left( \sum_j \mathbf{r}_j \right) \chi_i(\mathbf{r}; \bar{\mathbf{R}}) d\mathbf{r} \quad (39)$$

Notice that  $[\boldsymbol{\mu}_e]_{f,i}$  depends only on the initial and final electronic states, but not on the nuclear states. The relative intensities of the transitions for different nuclear states are given by the square of the integral on equation 38, which are called *Franck-Condon factors* (FCF):

$$\text{FCF}_{f,i} = \left| \int \phi_f^*(\mathbf{R}) \phi_i(\mathbf{R}) d\mathbf{R} \right|^2 \quad (40)$$

For diatomic molecules, where the vibrational and rotational wavefunctions are separable, the FCF as defined above breaks into two factors: radial and angular. The angular factor gives the selection rules for rotational transitions; the other factor is the overlap between the two radial wavefunctions. In this context, it is more common to define the FCFs as the radial (vibrational) part only (35), excluding the rotational selection rules. Graphically, it is possible to plot FCFs on grayscale 2-D maps (for instance, figures 21 and 25), each axis containing the different vibrational levels of an electronic state.

The importance of the Franck-Condon factors for our work is that they control the optical pumping process, as described in section 3.3. Besides, they are important to interpret the experimental ionization spectra, as discussed in sections 5.4 and 5.5.

### 3 LITERATURE REVIEW

In this section, we present a brief review on two important subjects to this work: the production of ultracold molecules and the transfer to the fundamental vibrational state. Both topics are important to atomic and molecular physics, and still the subject of new discoveries and improvements. In particular, we emphasize the *photoassociation* (PA) and optical pumping techniques, which are the ones that we have used in our experiment.

#### 3.1 Photoassociation: producing ultracold molecules

The process by which two colliding atoms can form a molecule by interacting with light is known since a long time. (31-42) In 1928, in an experiment (3) with potassium vapor, scientists discovered a diffuse spectral band in 575 nm that corresponds to a free-to-bound state transition. However, molecular spectroscopy performed on thermal conditions generally has poor resolution due to Doppler broadening effects and other reasons. Here we shall focus on the photoassociation of ultracold atoms, which became possible after the development of laser cooling and trapping.

Briefly, photoassociation (or simply PA) consists on the production of a bound molecular state via absorption of a photon by two colliding atoms. We can describe it as follows: two initially free atoms begin a collisional process. With an adequately tuned laser beam, it is possible to excite this atomic pair to a bound state in the electronic excited potential (Figure 3-i). From this point, it is possible obtain rich information of this molecular potential by, for example, ionizing the excited molecule. (42) If however the goal is to produce a stable molecule, one can simply allow spontaneous decay to the electronic ground state (fig. 3-ii). For an efficient molecular production rate, the decay probability should favor bound rather than free states of the ground potential.

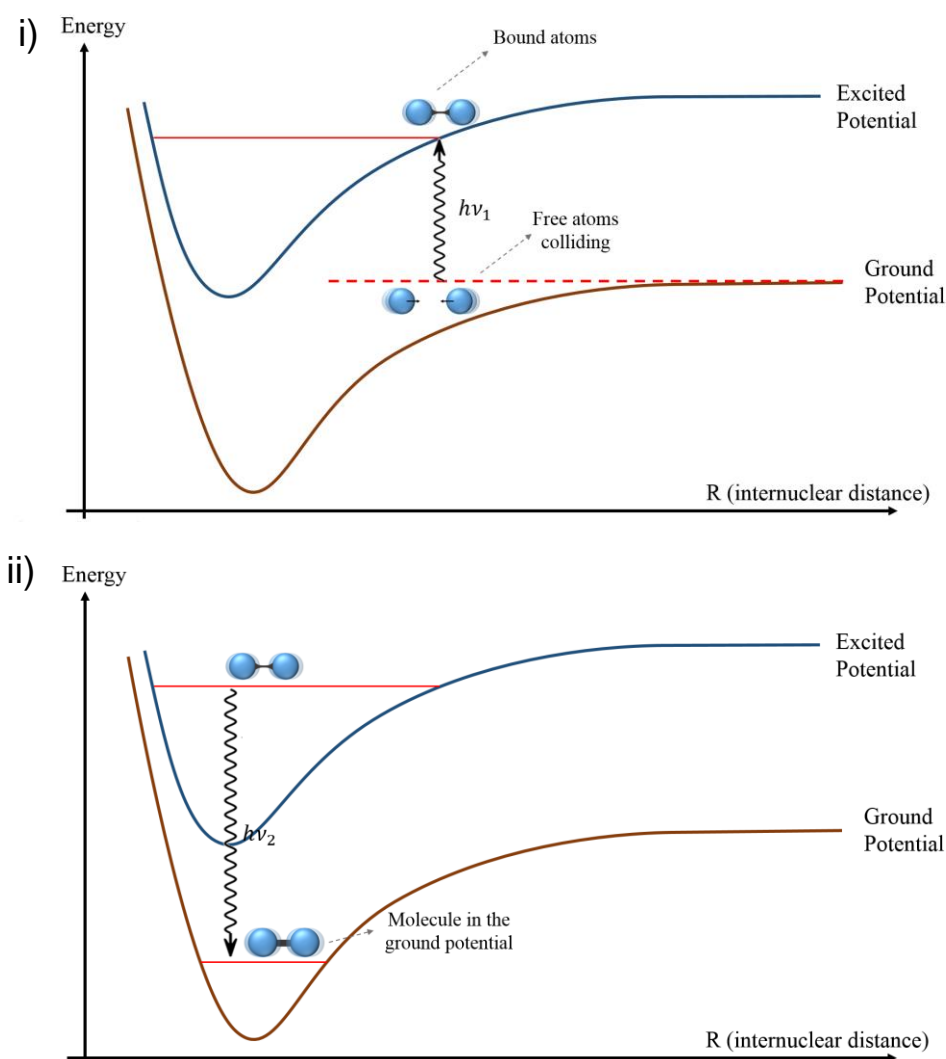


Figure 3 – Schematic representation of the photoassociation process. In i), an initially free atomic pair absorbs a photon and is excited to a bound state of a certain excited electronic potential. This is the photoassociation itself. In ii), the atomic pair spontaneously decay to a bound state of the ground electronic potential.

Source: By the author.

As soon as the first results on laser trapping and cooling were obtained, the search for molecules produced from ultracold atoms had a boost. In 1987, same year of the first MOT (43), Thorsheim and co-workers proposed theoretically the photoassociative mechanism for ultracold atoms. (44)

In this paper, the authors obtained a theoretical expression for the photoassociation rate, as well as for spontaneous decay to bound states and stimulated emission to the initial free state. For simplicity, they consider a pure Hund's-case-(b)\* and neglect the fine and hyperfine structure of the molecular potentials. Then they apply the model to sodium atoms, using

\* See chapter V section 2 on HERZBERG (31).

experimental and *ab initio* potential data for Na, considering  $X^1\Sigma_g \rightarrow A^1\Sigma_u$  and  $^3\Sigma_u \rightarrow ^3\Sigma_g$  photoassociation paths. They concluded that it was possible to achieve good results for reasonable experimental conditions (such as  $T \sim 10$  mK and  $1$  W/cm<sup>2</sup> laser intensity).

A few years later (1993 Lett and co-workers (45) experimentally performed photoassociation spectroscopy in sodium atoms. They photoassociated sodium atomic pairs to bound states of the  $1_g$  potential, and then ionized those excited molecules with a second photon (of the same source), which can be described by the equation  $\text{Na} + \text{Na} + 2h\nu \rightarrow \text{Na}_2^* + h\nu \rightarrow \dots \rightarrow \text{Na}_2^+ + e^-$  ( $\text{Na}_2^*$  represents the excited molecule). This process is usually referred as *photoassociative ionization*, and still useful until nowadays. (46-48)

By monitoring the ion signal as function of the photon frequency ( $\nu$ ), they were able to observe several peaks related to different vibrational states of the  $1_g$  potential (see Figure 4-a). Besides, they acquired a detailed spectrum around a single peak, revealing a structure that they attributed to the molecular hyperfine splitting (Figure 4-b). We shall discuss similar results in section 5.2, related to our work.

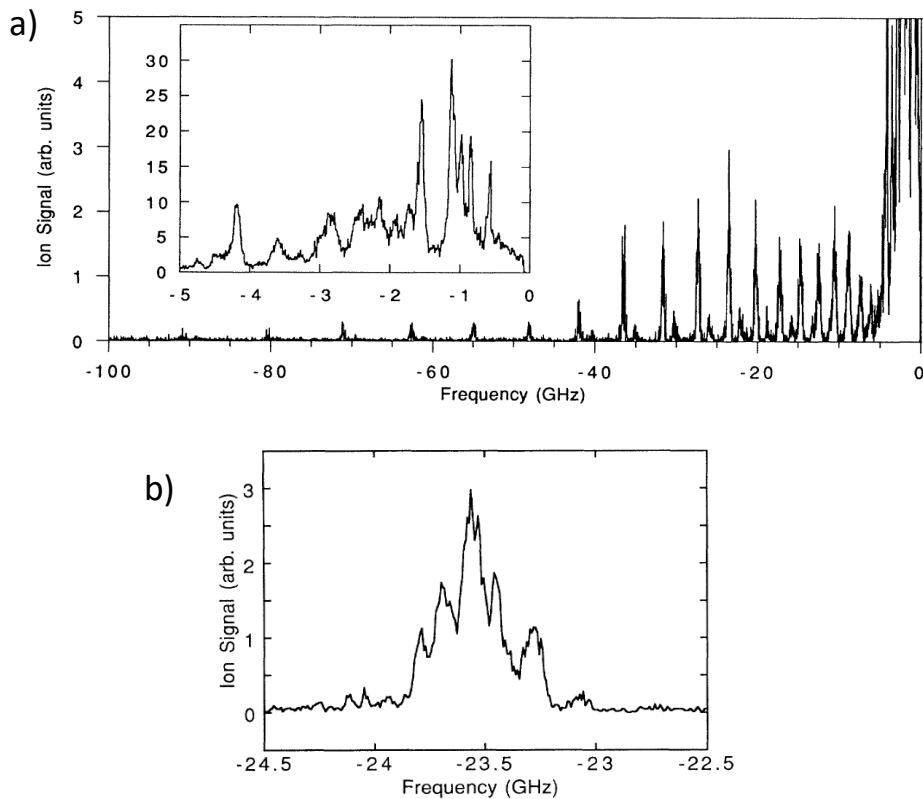


Figure 4 – Ionization spectra of Na<sub>2</sub> as a function of the PA laser frequency  $\nu$  (zero set on atomic  $S_{(1/2)} \rightarrow P_{(3/2)}$  transition). a) Broad spectrum showing several peaks, corresponding to different vibrational levels of the  $1_g$  potential. The inset shows the shows the region from 0 to -5GHz. b) Fine spectrum of a single vibrational peak, showing off the molecular hyperfine structure.

Source: LETT et al. (45)

Another interesting fact about these spectra is that their abscissa axis is in function of the laser detuning relative to the atomic trapping transition. This can be understood, for example, looking back at Figure 3-a, in which we can see that the photon energy is slightly smaller than the asymptotic difference between the two potentials. In the case of sodium, the involved molecular potentials are  $^1\Sigma_g^+$  and  $1_g$ , which in the asymptotical limit of  $R \rightarrow \infty$  goes respectively to  $S_{\frac{1}{2}} + S_{\frac{1}{2}}$  and  $S_{\frac{1}{2}} + P_{\frac{3}{2}}$  atomic states.

The first photoassociation experiment with rubidium molecules was performed in the same year, by Miller and co-workers. (49) The authors have measured a PA vibrational spectrum from the excited  $^3\Sigma_g^+$  state of  $\text{Rb}_2$ , similarly to Lett's group. In the following years, other groups managed to photoassociate homonuclear molecules of other alkaline atoms like Li (50), K(51) and Cs (52).

Photoassociation of heteronuclear molecules began to be studied right after the success with single-species molecules. In 1998, He Wang and William C. Stwalley (53) analyzed the free-to-bound transitions of several heteronuclear alkali pairs. In this theoretical paper, the KRb molecule was highlighted as a good candidate for long range photoassociation. The first PA spectrum of heteronuclear molecules (in the excited state), however, was made with NaCs molecules by Shaffer, Chalupczak and Bigelow. (54)

### 3.2 A counterpart to photoassociation: Feshbach molecules

Another technique used to produce molecules from ultracold atoms is called magnetoassociation (MA) and relies on Feshbach resonances. Briefly, a Feshbach resonance is possible when the energy of an atomic colliding pair is close to the energy of a bound state on another potential. If an external perturbation is applied in such way to compensate for this little – yet important – energy difference between the free and bound states, a spontaneous mixing will occur and molecules can be produced. If the magnetic dipole moments in each potential are different from each other, the external perturbation can be a magnetic field. For this reason, the process is called magnetoassociation (see Figure 5).

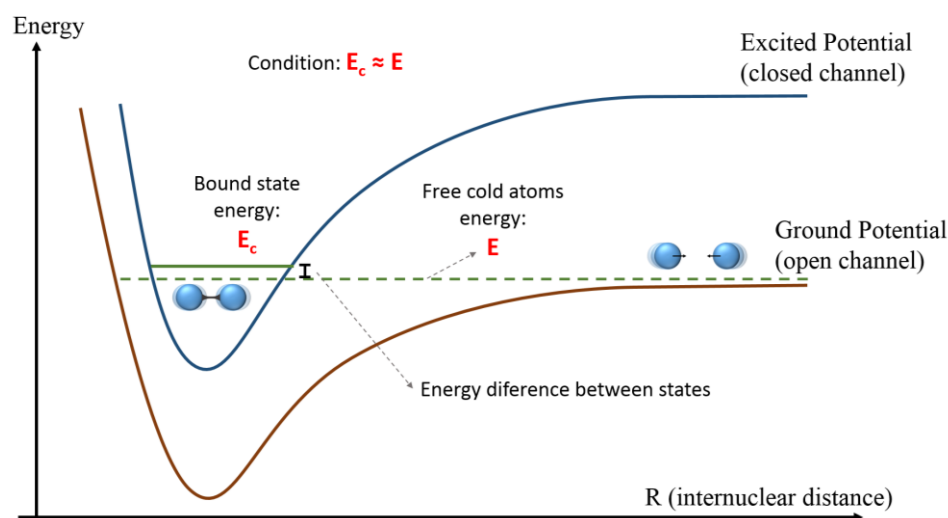


Figure 5 – A Feshbach resonance is possible when the energy of a bound state ( $E_c$ ) in a certain potential is close to the energy of free atoms ( $E$ ) in another potential (for ultracold atoms,  $E$  is assumed to be the asymptote of the potential). If the dipole moments in each potential (closed and open channels) are different, it is possible to use a magnetic field to compensate for the energy difference between the states. With the right magnetic tuning, a spontaneous mixing of the states leads to production of molecules.

Source: By the author.

The potential through which the free atoms come from is called *open channel*, whereas the potential in which a bound state is achieved is the *closed channel*. A good review about Feshbach resonances can be found on this reference. (55)

The Feshbach resonance mechanism was proposed in 1976, by Stwalley. (56) But the first experimental achievements came in 1998 (57-58), after the successful production of a *Bose-Einstein Condensate* (BEC). Since then, it has been a standard method for producing molecules from ultracold atoms. (59)

Feshbach molecules are usually produced in robust experiments. The required magnetic fields are typically on hundreds of Gauss, which require considerable sized coils and high currents. It is also usual to produce a BEC as a stage to reach magnetoassociation (59), which is not trivial to be done. For this reason and others, we have chosen photoassociation as the mechanism to produce our molecules, as it can be considerably simpler than MA.

### 3.3 Optical pumping to the vibrational ground state

Once the molecules are produced in the electronic ground potential, they are typically located in a distribution around high rovibrational levels of this potential. This is an issue, as for the great majority of applications it is necessary to have a molecular sample in a pure state of internal degrees of freedom (like (21) and (22)); many of those applications require the

fundamental rovibrational state. For the purposes of our experiment, we are concerned only to the vibrational purity in  $\nu = 0$ , the fundamental vibrational state.

Two main techniques are currently used for transferring molecules to ground rovibrational state: *the stimulated Raman adiabatic passage* (STIRAP) and optical pumping. The first technique consists on a coherent process involving two light frequencies and an intermediate state. The intensities of the two photon sources should be time-controlled differently, in a “counter-intuitive” way (as the light which tunes the second transition should peak before the other, which tunes the first transition – see (60)). This technique has applications in several situations (61-63), including the transfer of molecules from excited to ground rovibrational states. (64)

We choose to work with the optical pumping technique. This one is based on successive cycles of absorption and emission of photons by the molecules, resulting in an “oriented random walk” of each molecule towards the desired state. In each cycle, the emission is more likely to happen to lower vibrational states, due to Franck-Condon factors. The light source for the optical pumping must be broadband, so the molecules can be excited from several vibrational states. By shaping the light source so that the desired vibrational state is never excited, the molecular population will eventually accumulate on this state (which becomes a so called “dark state”). The process is illustrated on Figure 6. More details of this method will be given in section 4.2.3.

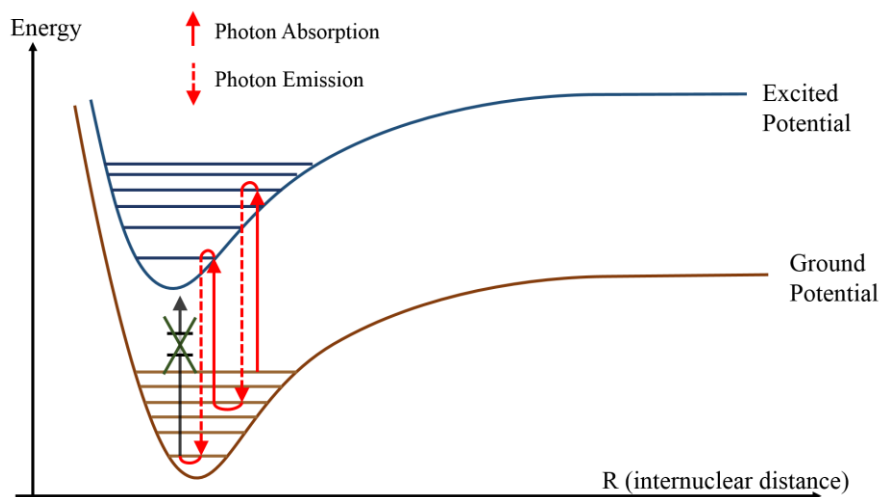


Figure 6 – Schematic representation of the molecular optical pumping process. A broadband light source is used to excite molecules from the various vibrational levels of the ground potential; once excited, they spontaneously decay to other random vibrational levels. In this example, the molecule absorbs and emits two times until it falls to the fundamental  $\nu$  state. Once there, it cannot be excited again, as the light source is shaped for this purpose.

Source: By the author

The first successful work on vibrational cooling via optical pumping was done by Viteau and collaborators in 2008. (65) They photoassociated Cs atoms trapped in the MOT with a continuous laser tuned around  $1\text{ cm}^{-1}$  below the atomic asymptote  $6s_{1/2} \rightarrow 6p_{3/2}$ . Then a broadband femtosecond pulsed laser (80 MHz of repetition rate) was used to perform the optical pumping. In order to have the  $\nu = 0$  as a dark state, the broadband source had its spectrum hard-cut for frequencies greater than a certain value. This value corresponds to the transition from  $\nu = 0$  to  $\nu' = 0$  in the excited potential (see Figure 7). The spectral shaping was done by a simple method, using a diffraction grating, a blocker, a mirror and a lens.

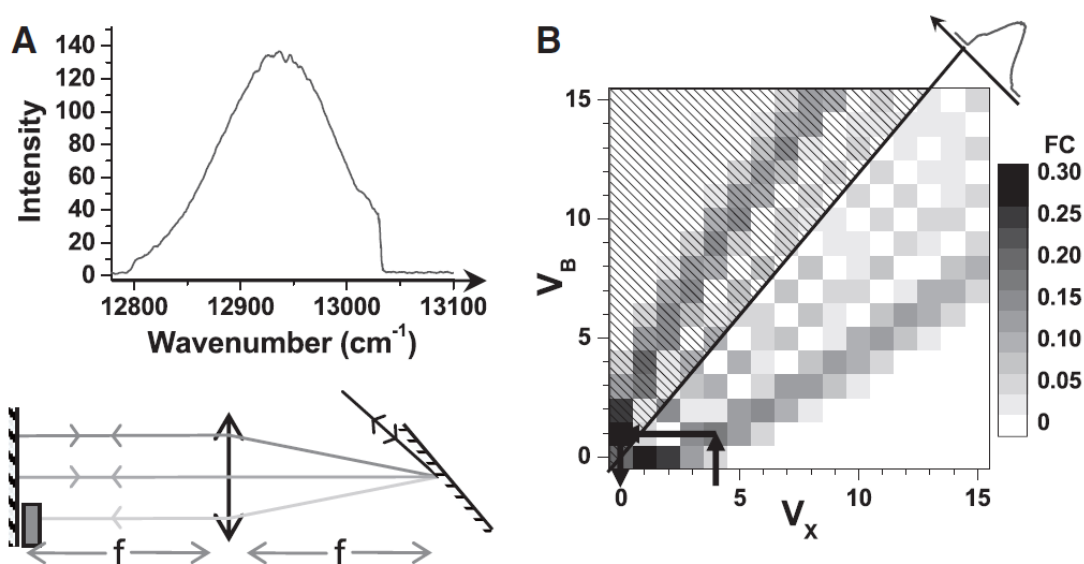


Figure 7 – Scheme for molecular optical pumping, in Viteau’s  $\text{Cs}_2$  experiment. In A, the broadband light is spectrally open by a diffraction grating, and then a blocker cuts the “blue” part of the spectrum. In B, Franck-Condon map is shown. The cutoff frequency is so that all transitions from  $\nu_x = 0$  are forbidden.

Source: VITEAU et al. (65)

Detection of the molecules in the lowest vibrational levels of the ground potential was performed via resonance enhanced multiphoton ionization (REMPI). If the measurement is made after enough time (milliseconds), only transitions starting from  $\nu = 0$  are relevantly observed (Figure 8-a). This means that a molecular population ( $65 \pm 10\%$  of the total) is accumulating at the fundamental vibrational level. The REMPI spectrum can also be performed after a certain number of pulses from the pumping broadband laser. If this is done, it is possible to observe the populational evolution, going from other states to the vibrational ground (Figure 8-b).

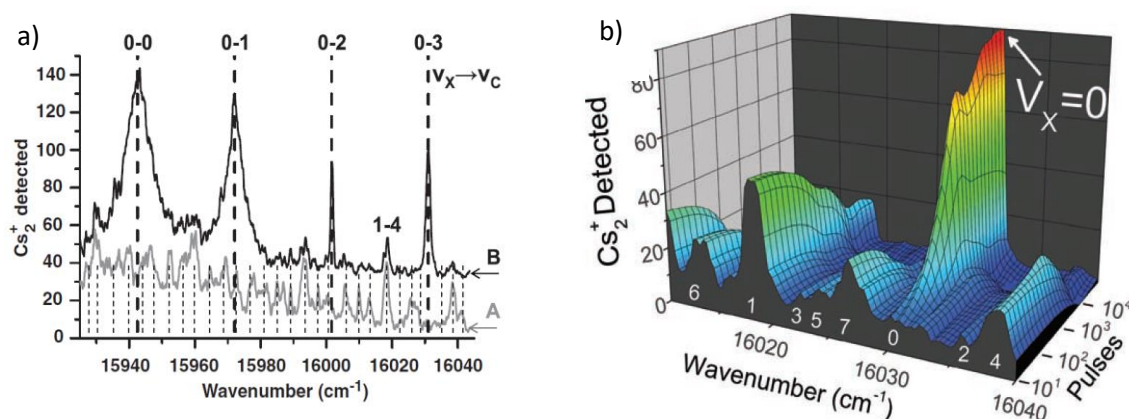


Figure 8 – Main results from Viteau's work. Molecular detection is performed via REMPI, an ionization technique sensitive to different vibrational states. In a), REMPI spectrum is measured after several pumping cycles. Comparison between spectrum with (B) and without (A) broadband shaping evidences the optical pumping process, as in B only the peaks from  $\nu = 0$  are notorious. In b), peaks from different vibrational states are measured in function of the number of pumping laser pulses. It is possible to observe the populational transfer from other states to  $\nu = 0$ .

Source: VITEAU et al. (65)

One year later, in the same group, another interesting result concerning to optical pumping was achieved. (66) Most of the experimental conditions were kept unchanged, except for the pumping light source, which was replaced by an incoherent *broadband diode laser* (BDL), operating as *continuous wave* (CW). The laser was set the near threshold condition, meaning that the laser part of the spectrum had almost the same power than the luminescent part. This represents a bandwidth increase from 2 to 10 nm.

Another experimental change was in the band-shaping method. To achieve  $\nu = 0$ , the grating-blocker system was replaced by a set of commercial long-pass filters, with an angle relative to the beam, so that the right cutoff frequency is set. Despite this technical difference, the concept remains the same as the previous experiment. An essentially different idea, however, was used to accumulate the molecules in the  $\nu = 1$  vibrational state instead of the fundamental one. The light beam was spectrally open by a diffraction grating, but instead of using a single physical blocker to remove frequencies above a certain value, four blockers were used to remove specific frequency values. Those values corresponds to the transitions from  $\nu = 1$  to the first four vibrational levels of the excited  $B^1\Pi_u$  potential. Higher levels of  $B^1\Pi_u$  were naturally inaccessible by the light source, so the  $\nu = 1$  becomes a dark state.

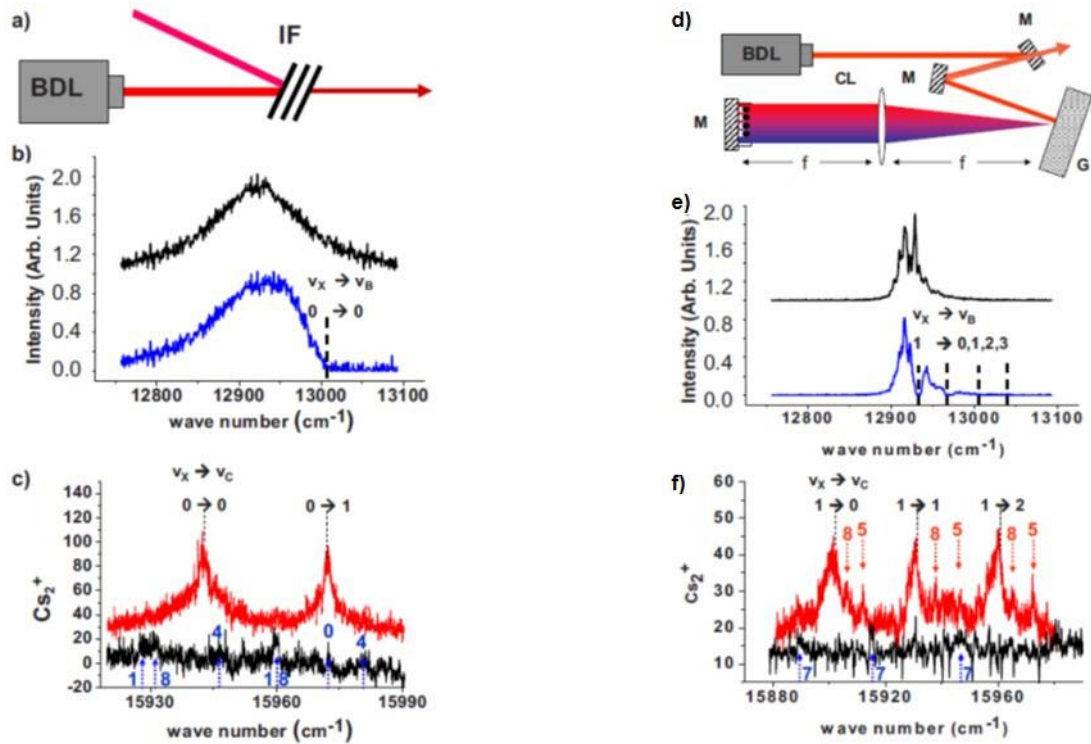


Figure 9 – Results for the second vibrational cooling experiment. (a) The setup for  $\nu=0$  pumping was changed, having the grating-blocker replaced by a set of long-pass filters. The final spectrum shape (b) and the results in molecular transfer (c) remained the same. (d) A different concept was used for  $\nu = 1$  pumping. The light spectrally open by a grating is shaped by four small blockers in specific positions. The final spectrum (e) has the bands which excite  $\nu = 1$  transitions removed, making this a dark state. Experimental REMPI spectrum (f) shows the populational accumulation on this state.

Source: SOFIKITIS et al. (66)

The results for both setups (the filter cut and the blocker cut) evidence the optical pumping process, each one for the desired state ( $\nu = 0$  and  $\nu = 1$  respectively). This shows that the coherence of the light for optical pumping transfer is not crucial, and also that other vibrational levels rather than  $\nu = 0$  can be populated if more complex shaping is applied.



## **4 EXPERIMENTAL SETUP**

This chapter covers details about most of the experimental techniques that are relevant to this work. In section 4.1, we describe the fundamental setup that is common to every experiment performed in our laboratory: the vacuum system, the magneto-optical trap and the optical dipole trap. Section 4.2 is dedicated to the photoassociation and vibrational cooling techniques, which are the essence of this work in particular. Section 4.3 describes the main detection technique used for this work: the resonance-enhanced multiphoton ionization (REMPI). Finally, section 4.4 describes the apparatus that we use to control and synchronize the events in the performed experiments.

### **4.1 Atomic and molecular trapping and cooling**

In order to cool and trap rubidium atoms, we first decelerate them using a Zeeman slower (7), and then confine the cold atoms in a magneto-optical trap. This MOT can be used to load an optical dipole trap (ODT), which is able to confine both atoms and molecules in a smaller volume. We will discuss these procedures in more details in this section.

#### **4.1.1 Vacuum system**

The experiment is performed in an ultra-high vacuum chamber, inside which the MOT and ODT traps are created. The vacuum system was designed by former members (67-68) of our group and built by our institution mechanical workshop. A schematic drawing of the system is presented in figure 10:

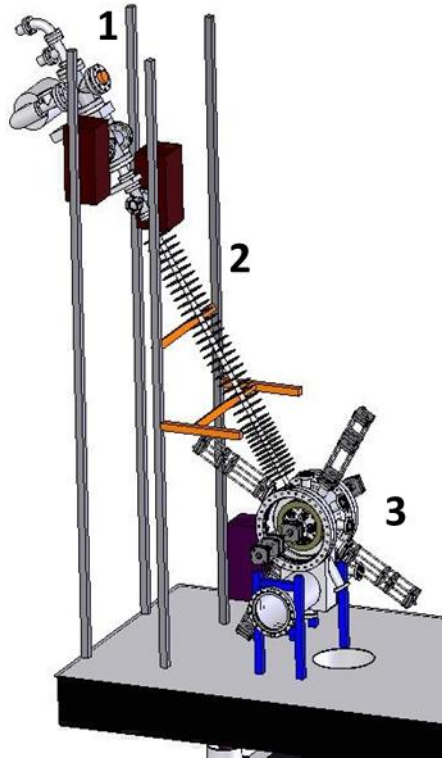


Figure 10 – Schematic drawing of the vacuum system where the experiment is performed. Part 1 indicates the atomic oven, where an Rb sample is heated to around 90 °C, providing an atomic flow of  $2 \cdot 10^{16}$  atoms/s. The tube in part 2 is the Zeeman slower, where atoms with an initial speed below 346 m/s are decelerated to a few m/s before entering the final vacuum chamber, indicated on part 3. In this chamber, a pressure below  $10^{-11}$ Torr is maintained, providing an adequate environment to the atomic and molecular traps.

Source: Adapted from MENEGATTI. (68)

In figure 10, part 1 is the atomic oven, in which ampoules containing  $^{85}\text{Rb}$  and  $^{87}\text{Rb}$  are heated to temperatures around 90 °C. At this temperature, rubidium atoms reach a vapor pressure of  $\sim 1.2 \cdot 10^{-4}$  Torr, yielding a collimated atomic flow of  $2 \cdot 10^{16}$  atoms/s at the exit of the oven. It is important to mention that this system was actually designed to provide potassium (K) and rubidium (Rb) atoms, but for the experiment described in this dissertation, it was adapted to work with Rb atoms only.

Part 2 (figure 10) represents the Zeeman slower, which is responsible for decelerating the atomic beam (7). In Zeeman tuning technique, the atoms are constantly decelerated by a counterpropagating resonant optical beam. As the atoms change their velocity, its resonance frequency also changes due to the Doppler effect. This is compensated by creating an inhomogeneous magnetic field along the tube axis, which corrects the atomic resonance frequency via Zeeman effect. The generic expression for the magnetic field as a function of the longitudinal coordinate  $z$  is given by:

$$B(z) = B_1 + B_2\sqrt{1 - \alpha z} \quad (41)$$

The constants  $B_1$ ,  $B_2$  and  $\alpha$  are chosen according to the Zeeman shift of the considered transition, the laser detuning from the resonance and the maximum initial velocity of the atoms that can be decelerated. It is convenient to choose the laser detuning to be of hundreds of MHz, so the beam does not affect the magneto-optical trap when passing through it. (67)

In our system, we use the D<sub>2</sub> rubidium line for this process, and the Zeeman slower light is red-detuned from this line. The slower tube is about 1 m long and is surrounded by 38 coils, designed to produce the field profile on equation 41. Rb atoms with an initial speed of less than 346 m/s can be decelerated by the apparatus. (67) The coils are clustered into 4 groups, where the last one generates a field in the opposite direction compared to the others. This group is called “compensation coils”, and is used to cancel the magnetic field in the final chamber region, thus avoiding interference with the MOT fields.

After passing through the Zeeman slower, the atoms reach the vacuum chamber indicated on part 3 of figure 10, where the MOT and ODT traps are produced. This chamber is evacuated to an ideal pressure of less than  $10^{-11}$ Torr. The low pressure in this region is crucial for the quality of the traps, because collisions with background particles is one of the main loss mechanisms. The chamber has several optical windows, through which the light beams for the MOT, ODT, optical pumping and others can reach the atoms. It is also connected to an ion pump and a sublimation pump, both used to keep the low background pressure.

#### 4.1.2 The magneto-optical trap (MOT)

The magneto-optical trap was certainly one of the most important achievements for experimental Atomic Physics. It was first demonstrated in 1987 by Raab et al. (43), and since then it has been used on the majority of cold atoms experiments in the world.

The MOT is composed by two force components: a frictional force, which causes the atoms to decelerate, and a restoring force, which attracts the atoms to a certain spatial region. The frictional part is generated by three orthogonal pairs of counterpropagating optical beams, and is also called “optical molasses”. The light frequency of the six beams must be red-detuned with respect to the atomic resonance. Due to Doppler effect, each atom is more resonant with the beams that propagate in the opposite direction of its movement, thus absorbing more photons of these beams. This force causes the atoms to decelerate, which represents a temperature reduction on the atomic cloud. The cooling effect is limited by the so called

Doppler limit, when the average momentum of the atoms is comparable with the recoil due to photon absorption or emission. For  $^{87}\text{Rb}$  atoms, the Doppler limit is about  $146 \mu\text{K}$ . (69)

The restoring force is produced with a non-uniform magnetic field, besides the optical beams. In each direction, the magnetic field must vary linearly with space, as shown in Figure 11.a). If, for example, the excited state has quantum number  $F' = 1$ , then the field will cause a Zeeman splitting on the  $m_F$  quantum number (projection of the  $\mathbf{F}$  electronic plus nuclear angular momentum in the considered field direction) into  $m_F = 1, 0, -1$  (see 11.b)). Considering circularly polarized light, there will also be a selection rule for a transition  $F = 0 \rightarrow 1$  as follows: right polarization ( $\sigma^+$ ) excites only to  $m_F = 1$ , whereas left polarization ( $\sigma^-$ ) excites to  $m_F = -1$ . Setting the beam that comes from the positive-field side to be  $\sigma^-$ , atoms that are located on that side will be more resonant with this beam, as the energy of the allowed transition is reduced (remember that the light is red-detuned). It means, for instance, that atoms on the right side of the zero-field point will be forced to the left by the radiation pressure. Similarly, if the beam that comes from the negative-field side is  $\sigma^+$ , the atoms on that side will be forced to the zero-field point again. The result is a restoring force, which traps the atoms around the point of zero magnetic field. The same idea can be applied for  $F' > 1$ , always considering the selection rule for circularly polarized light.

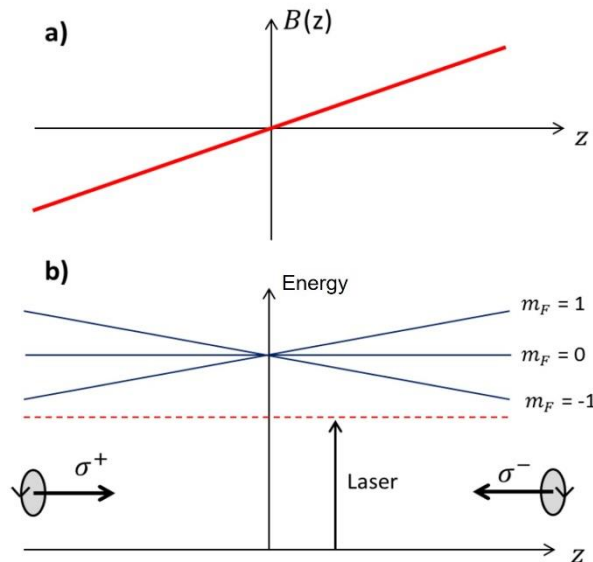


Figure 11 – Schematic representation of the MOT restoring force. A non-uniform magnetic field (fig. a) splits the states with different  $m_F$ . The beam that comes from the positive  $z$  side (right) is circularly polarized to the left, and the other beam is polarized to the right. Due to selection rules and the laser detuning to the red, atoms that have positive  $z$  coordinate are more resonant with the beam that comes from the right, having a net force to the left. The opposite situation happens at the negative  $z$  side.

Source: Adapted from MARANGONI. (67)

One more aspect to be considered on the MOT design is that the accessible atomic states must form a “closed cycle”. For example,  $^{85}\text{Rb}$  atoms excited to the  $5^2P_{3/2}$  can possibly decay to two different hyperfine states of  $5^2S_{1/2}$ , corresponding to  $F = 2$  and  $F = 3$ . The trapping light can only excite atoms from  $F = 3$ , therefore atoms that decay to  $F = 2$  are no longer accessible by this light source, leaving the cooling cycle. The solution, in this case, is to add another light source, called *repumping* light, which can re-excite those atoms that fall in  $F = 2$  state. This is better understood with figure 12, where the hyperfine states involved in this process are shown for  $^{85}\text{Rb}$ .

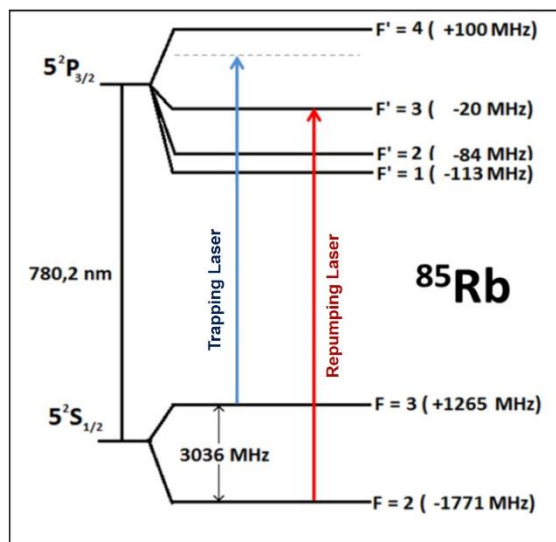


Figure 12 – Hyperfine structure of rubidium-85  $D_2$  line. The two laser frequencies used for the MOT (trapping and repumping) are shown by blue and red arrows, respectively.  
Source: Adapted from MARANGONI. (67)

For alkali atoms, which have a single valence electron, the simple structure of the energy levels makes it easy to create a closed cooling cycle, with one or two lasers. However, for more complex species (like molecules or transition metals), this is much more difficult due to the complexity of their structure, thus making laser cooling and trapping very challenging. (70-71)

#### 4.1.3 The optical dipole trap (ODT)

The optical dipole trap is a nearly conservative trap based on the optical dipole force. (72) The optical dipole force on atoms was first demonstrated in 1978 by Bjorkholm *et al.* (73), and the first ODT was produced in 1986 by Chu *et al.* (9), at the same epoch of the first MOT.

The optical dipole force on neutral and polarizable particles is proportional to the gradient of the light intensity, meaning that its potential energy is proportional to the light intensity itself. This can be quickly demonstrated by considering a harmonic oscillating electric field and a linearly polarizable particle:

$$\mathbf{E}(\mathbf{r}, t) = \mathbf{E}_0(\mathbf{r}) \cdot e^{-i\omega t} \quad (42)$$

$$\mathbf{d}(\mathbf{r}, t) = \alpha(\omega) \cdot \mathbf{E}(\mathbf{r}, t) \quad (43)$$

Here  $\mathbf{E}$  is the complex electric field,  $\mathbf{d}$  is the complex dipole moment and  $\alpha$  is the complex polarizability. The potential energy of the particles in this field is given by the time average of the scalar product between  $\mathbf{E}$  and  $\mathbf{d}$ , with a “1/2” factor due to the linearly induced dipole:

$$U(\mathbf{r}) = -\frac{\langle \mathbf{d}(\mathbf{r}, t) \cdot \mathbf{E}(\mathbf{r}, t) \rangle}{2} \quad (44)$$

A brief justification for the “1/2” factor due to the induced dipole moment is given on Appendix A, as most texts in this subject only mention it without justifying. One may calculate the time average of the two harmonic functions  $\mathbf{d}$  and  $\mathbf{E}$  according to section 6.9 of reference (74):

$$U(\mathbf{r}) = -\frac{1}{2} \frac{\text{Re}(\mathbf{d} \cdot \mathbf{E}^*)}{2} = -\frac{1}{4} |E_0|^2 \text{Re}(\alpha(\omega)) \quad (45)$$

Using the expression for light intensity in function of squared electric field (SI units; see reference (11)):

$$I = \frac{1}{2} c \varepsilon_0 |E_0|^2 \quad (46)$$

Equation 45 becomes:

$$U(\mathbf{r}) = -\frac{1}{2} \frac{I}{\varepsilon_0 c} \text{Re}(\alpha(\omega)) \quad (47)$$

Equation 47 shows that the potential energy for the optical dipole force is proportional to the light intensity. Another interesting fact is that this potential is applicable for atoms,

molecules or even microscopic particles; it is only required that the object is polarizable by an electric field. In the case of atoms, semiclassical models (like presented in (8)) show that, for  $\omega$  close to a single atomic resonance  $\omega_0$ , it is true that  $\text{Re}(\alpha(\omega)) > 0$  for  $\omega < \omega_0$  and  $\text{Re}(\alpha(\omega)) < 0$  for  $\omega > \omega_0$ . This separates the optical dipole traps into two categories, the *red-detuned* and the *blue-detuned* ones. By providing a focused light beam which is red-detuned from the atomic resonance, it is possible to create an attractive potential well, whose depth is proportional to the light intensity.

In our experiment, we create a red-detuned ODT with a Gaussian beam. It is visible from equation 47 that, in this case, the potential well has a negative Gaussian shape. One issue is that the potential has weak confinement along the propagation direction of the beam, because the Rayleigh length  $z_r$  of a Gaussian light beam is typically much greater than its waist. This limitation is solved by crossing two Gaussian beams focused on the same point, creating a so called *crossed* ODT. Figure 13 illustrates the difference between single beam ODT and crossed ODT.

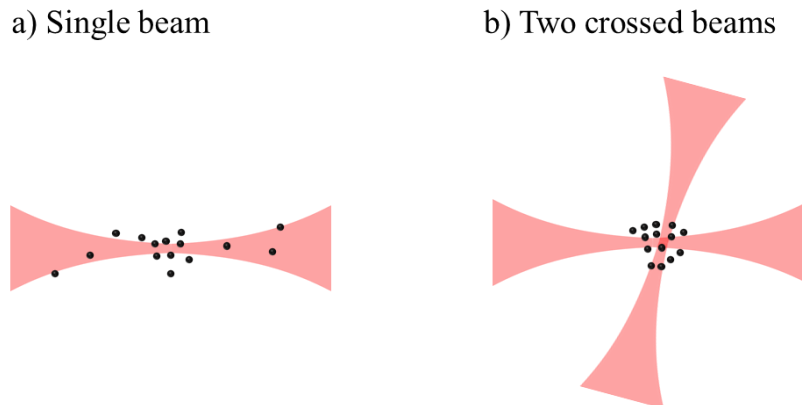


Figure 13 – Comparison between single beam ODT (a) and crossed ODT (b). The confinement along the propagation axis in case (a) is poor, whereas crossed ODT has a good confinement in all spatial directions.

Source: By the author.

Another important aspect of an optical dipole trap is how far the light frequency is from the resonance. It is possible to show that a near-resonance trap, although very deep because  $\text{Re}(\alpha(\omega))$  is large, have also an undesired high scattering rate. The ideal case is to work with a *far-off-resonance trap* (FORT), which is nearly-conservative due to low scattering rate. The ideal detuning from the resonance may be chosen to achieve a good balance between depth and scattering effects.

#### 4.1.4 Optical setup for MOT and ODT

For the production of the MOT, two Toptica DL 100 diode lasers are used: one to the trapping light and the other to the repumping light. Both lasers work around 780.2 nm, near the Rb D<sub>2</sub> line, which corresponds to the transitions from  $5S_{1/2}$  to  $5P_{3/2}$  (recall Figure 12). Each laser frequency is determined by using *saturated absorption spectroscopy* (SAS) technique (75), which uses an Rb vapor cell in room temperature, and then is locked by a Toptica Digilock 110 module.

The optical setup for both trapping and repumping lights is show in Figure 14. *Acousto-optic modulators* (AOM) from IntraAction are used to achieve the desired detuning for each beam. The trapping laser provides around 100 mW of light. This beam is subject to a double pass on AOM2, followed by an amplification to 400 mW by a *tapered amplifier* (TA), from which it is coupled to an optical fiber. Part of the beam is extracted by a polarizer beam splitter before AOM2, and is sent to AOM3 to be used on the Zeeman slower optical setup. The repumping laser, which also provides  $\sim 100$  mW, is divided between Zeeman slower and MOT on AOM4. The first order goes to the Zeeman slower arrangement, whereas zeroth order is sent to AOM5 and then coupled to an optical fiber.

Trapping and repumping lights are combined to the Zeeman slower setup by a half mirror. The combined beam is then amplified twice: the first time in a Thorlabs TCLDM9 slave laser, and the second in another TA. After this, it is coupled to an optical fiber.

The trapping and repumping optical fibers are part of an optical set from Canadian Instrumentation & Research Ltda. They are combined and distributed to six output fibers, of which three are used to the MOT.

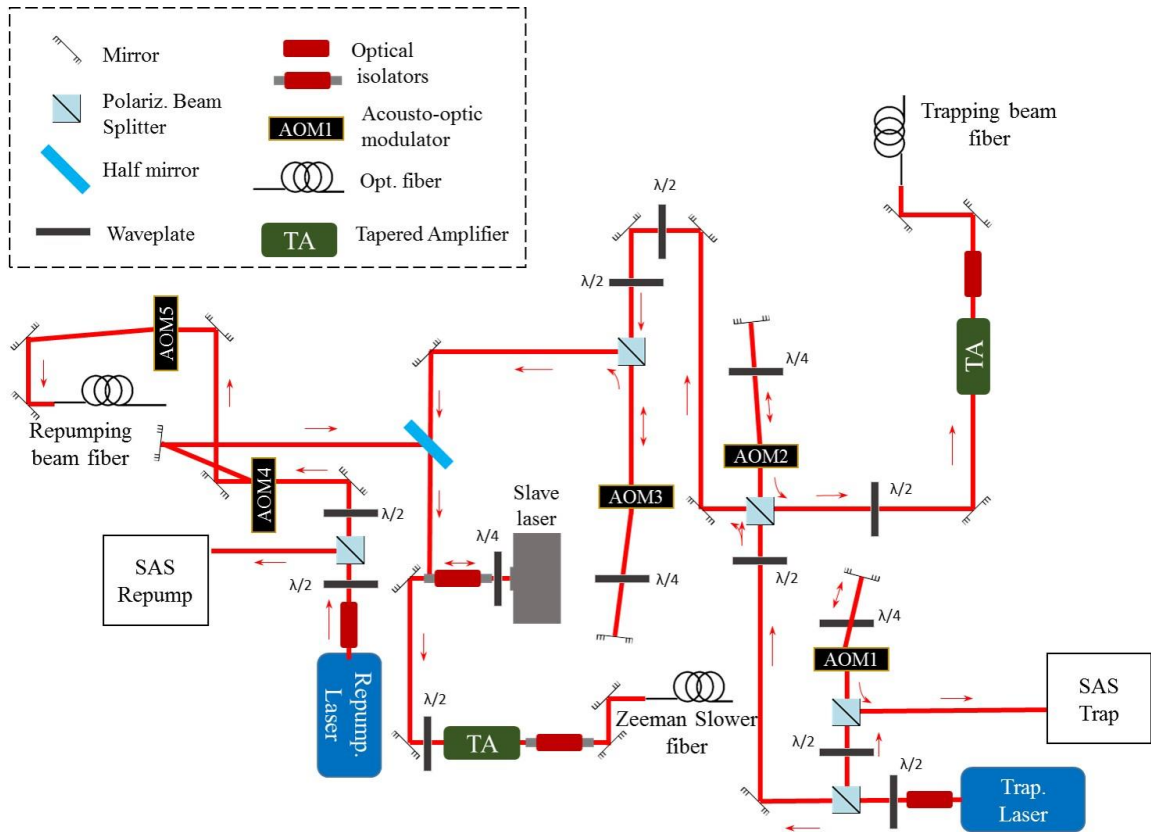


Figure 14 – Optical setup for trapping, repumping and Zeeman slower. Both laser frequencies are determined and locked by saturated absorption spectroscopy (SAS) technique. (75) Trapping beam is detuned by AOM2 and amplified by a TA. Repumping beam is detuned by AOM5. Zeeman slower receives light from both trapping and repumping sources, and is twice amplified before sent to the experiment.

Source: By the author.

The following table shows the AOM frequencies used on this experiment.

Table 1 – Acousto-optic modulators and their frequencies.

AOM	Frequency (MHz)	Pass	Purpose
AOM1	-93.5	Double	Trapping light SAS
AOM2	+83.5	Double	Trapping light to the MOT
AOM3	-200	Double	Trapping light to Zeeman slower
AOM4	-175	Single	Repumping light to Zeeman slower
AOM5	+80.0	Single	Repumping light to the MOT

Source: By the author.

The optical dipole trap must be produced with a high power light source. This is achieved using an IPG Photonics YAR-50K-1064-SF high power fiber amplifier, with an operational range from 1060 nm to 1070 nm. This amplifier can generate an adjustable output power of up to 50 W, with a minimal linewidth of 60 kHz. The light source that seeds the amplifier will be discussed in detail in section 4.2. The optical setup for the crossed ODT is shown in Figure 15. The beam is first sent to an AOM, which allows for control of the laser

intensity during the experiment. The first order beam passes through a telescope, which increases the beam waist by a factor of two. The beam is then focused inside the atomic chamber, with a measured waist of  $w_0 = (40 \pm 10)\mu\text{m}$  on the focus. (76) The waist was measured by using the *knife-edge method*. (77) After passing by the chamber for the first time, the beam is recycled to provide the second arm of the crossed trap. This beam has its polarization direction rotated by  $90^\circ$  by a half-wave plate, to avoid interference effects with the first arm. After the second pass on the chamber, the beam is dumped in an appropriate device.

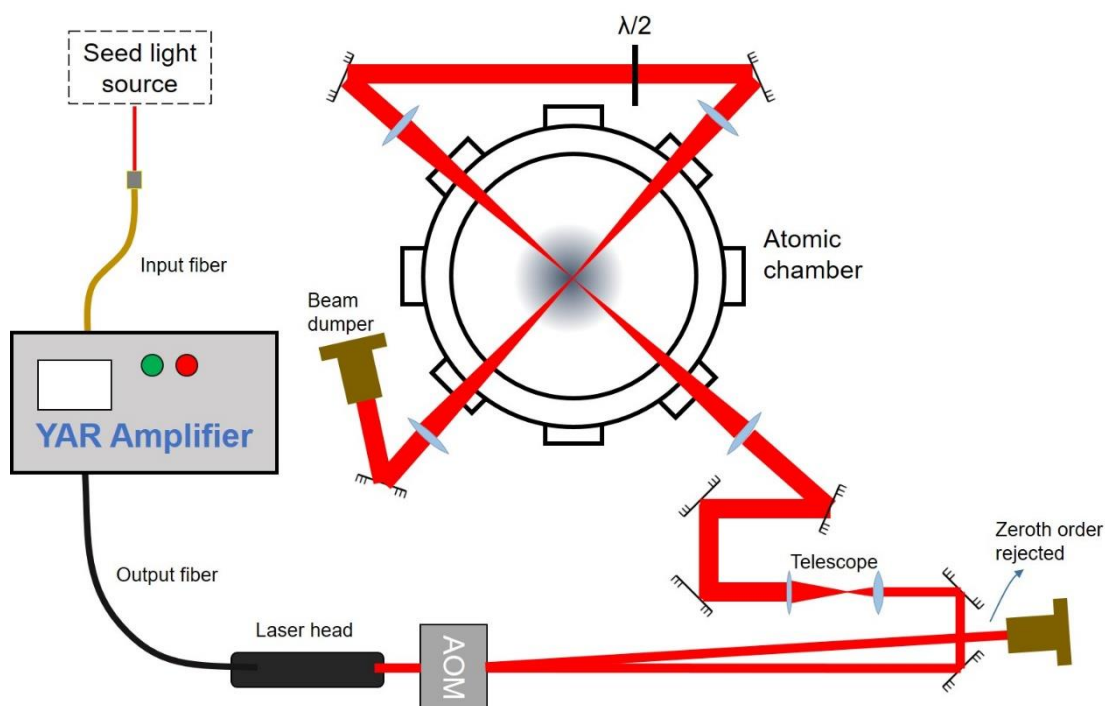


Figure 15 – Optical setup for the crossed optical dipole trap. The high power light is provided by a fiber amplifier, which provides up to 50 W. An AOM is used to control the laser intensity during the experiment. The same laser source is used to create the two arms of the crossed trap. The waist at the focus is of  $\approx 40 \mu\text{m}$ .

Source: By the author.

## 4.2 Production and manipulation of molecules

Once the atoms are cooled and trapped, molecules can be produced via photoassociation. In order to study molecular collisions in the ODT, molecules must be transferred to the fundamental vibrational state, which can be performed by optical pumping. Both photoassociation and optical pumping processes were briefly described in sections 3.1 and 3.3. In this section, we shall discuss technical details of the implementation of these techniques in our experiment involving  $\text{Rb}_2$  molecules.

### 4.2.1 Photoassociation

In the last years, atomic population lifetime measurements, performed in our old ODT, strongly suggest that the trap laser was able to produce molecules via photoassociation, due to its bandwidth of  $\sim 2$  nm. (78-79) Based on this result, we have decided to implement a major modification of our experimental setup, which allows us to control the molecular states that are accessed in the photoassociation process. The old high power broadband fiber laser was replaced by a YAR high power amplifier described in section 4.1.4. This amplifier is seeded by a single mode grating stabilized QPhotonics QLD-1060-100S diode laser, tunable in the 1062-1070 nm range. The linewidth of this diode laser is below 1 MHz, and the YAR amplifier is designed to work with at least 60 kHz of linewidth; therefore the amplified light has the same linewidth as the seed laser, i.e., below 1 MHz. Comparing to the old high power laser (bandwidth  $\sim 2$  nm or  $\sim 50$  GHz), this is an improvement of at least  $5 \cdot 10^4$  in the laser resolution. This allows us to solve the rotational structure of the vibrational states used in photoassociation, which are separated by  $\sim 1$  GHz.

According to our previous work, the photoassociation occurs between the fundamental  $X^1\Sigma_g^+$  and the excited  $0_u^+$  potentials of the Rb-Rb interaction. Based on spectroscopic data provided by our collaborators Olivier Dulieu and Nadia Bouloufa-Maafa, we predict that the  $0_u^+$  vibrational states from  $\nu' = 137$  to 140 are accessible by our diode laser and YAR amplifier operation range. Figure 16 shows the Franck-Condon factors for the excitation from the most energetic vibrational state of the fundamental  $X^1\Sigma_g^+$  potential to different vibrational states of  $0_u^+$ . The last vibrational state of the fundamental potential is a good approximation for the free atoms wavefunction with energy very close to the asymptotic limit. The wavelengths of each transition is also shown on table 2.

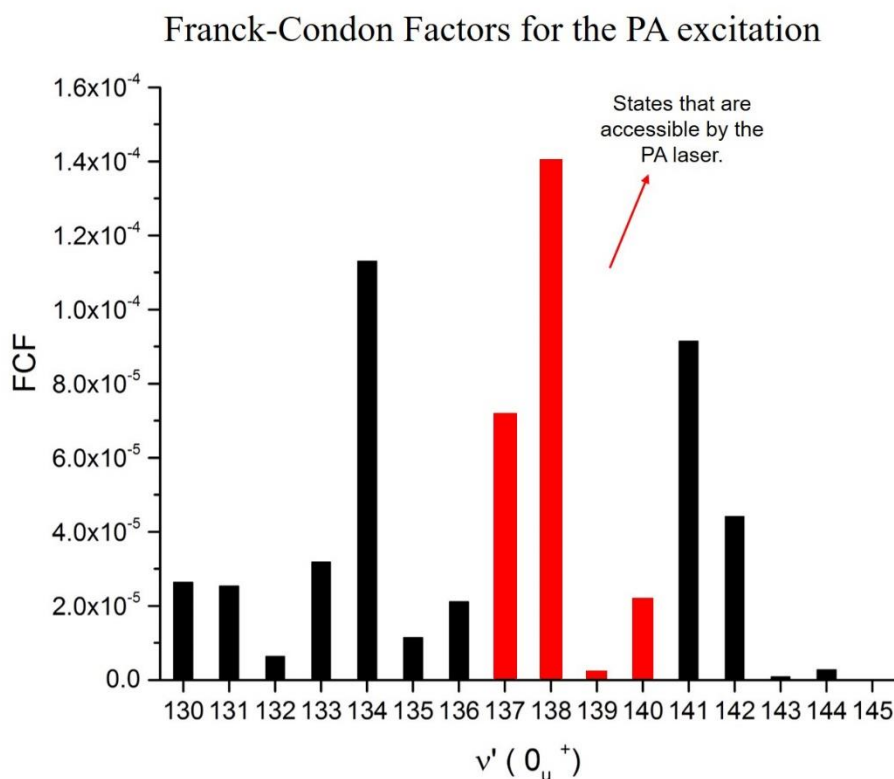


Figure 16 – Calculated Franck-Condon factors for the photon absorption from  $X^1\Sigma_g^+$  to  $0_u^+$ , which is used to the photoassociation. The calculations consider the most excited vibrational state of the  $X^1\Sigma_g^+$ , which is a good approximation for the free atoms wavefunction. In red, the states that can be accessed by the PA seed and amplifier tenability ranges (1060 to 1070 nm) are highlighted.

Source: By the author.

Table 2 – Accessible states by the PA laser and its wavelengths.

$v' (0_u^+)$	Franck-Condon Factor	Transition wavelength
137	$7.18 \cdot 10^{-5}$	1068.07
138	$1.40 \cdot 10^{-4}$	1066.17
139	$2.22 \cdot 10^{-6}$	1063.41
140	$2.19 \cdot 10^{-5}$	1061.78

Source: By the author.

## 4.2.2 Vibrational cooling

The vibrational cooling via optical pumping is a succession of absorption/emission cycles by the molecules, so that in average the vibrational energy of the molecules is reduced until most of them reach the dark fundamental state. To understand this process, we can study the Franck-Condon map between the two electronic states involved on the optical pumping. This map is a two-dimensional plot of the Franck-Condon factors for each pair of vibrational states; each axis contains the vibrational quantum number of each electronic state. Using the classical statement of the Franck-Condon principle (see section 2.4), it can be shown that the

most likely transitions (i.e., the highest Franck-Condon factors) for two single-minimum potentials lie in a parabolic-like curve in the Franck-Condon map. (80) This curve is called *Condon parabola*. (39) Figure 17 shows an abstract example of a Condon parabola.

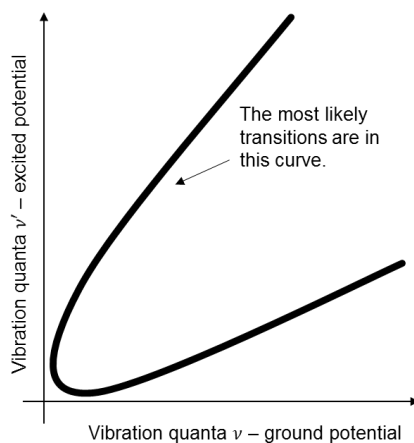


Figure 17 – Scheme of a Franck-Condon map, where the Franck-Condon factors are plotted as a function of the vibrational quantum numbers of each potential involved in the process. For molecular potentials that have a single minimum, the most probable transitions (i.e., the highest FCFs) are located in the Condon Parabola.

Source: By the author.

To excite the molecular transitions, it is necessary to provide a broadband light source, because the transitions have different frequencies. This broadband light also needs to be spectrally shaped, in order to remove all the spectral components that can excite transitions from the fundamental vibrational state of the ground potential; otherwise, the molecules would not accumulate in this state. This is performed by removing the frequencies greater than or equal to a certain cutoff frequency, which is that of the transition from  $\nu = 0$  to  $\nu' = 0$ . The final spectrum of the broadband source and the allowed excitations are represented in figure 18.

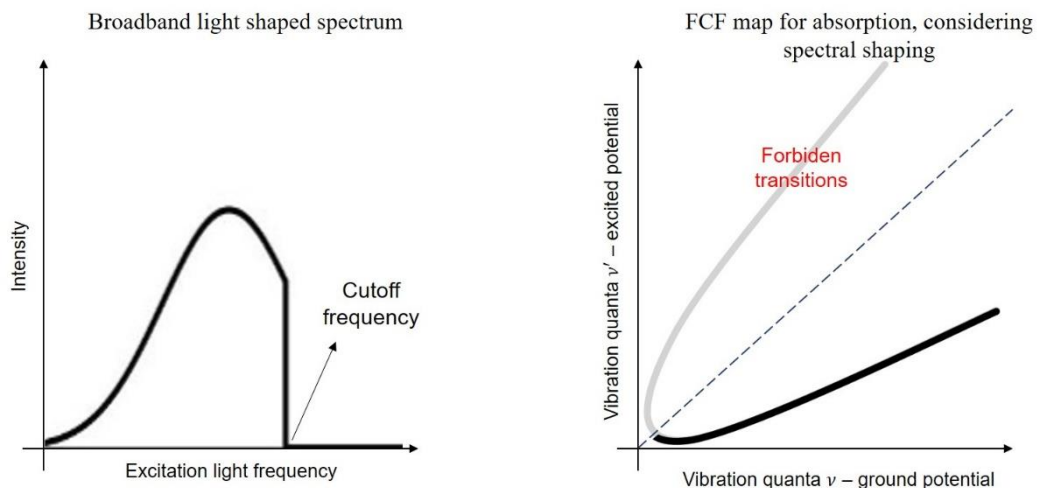


Figure 18 – Representation of the excitation light spectrum (left) and the Franck-Condon map for absorption of a photon by the molecules (right). The spectral shaping avoids any transition from the fundamental vibrational level of the ground potential.

Source: By the author.

Figure 19 shows a possible sequence of absorption and emission of photons in the vibrational cooling process. Due to the Condon parabola and the spectral shaping of the exciting light source, the molecule have a high probability of being excited to a low energy vibrational state on the excited potential. In the sequence, the spontaneous decay (which is not subject to the limitation of the spectral shaping) is more likely to happen either to the initial vibrational state (path ii) or to another one which is less energetic than the first (path i). After several cycles, the molecules will reduce their vibrational quantum number, until they reach the fundamental vibrational state. Once this happens, they cannot be excited again by the broadband shaped source.

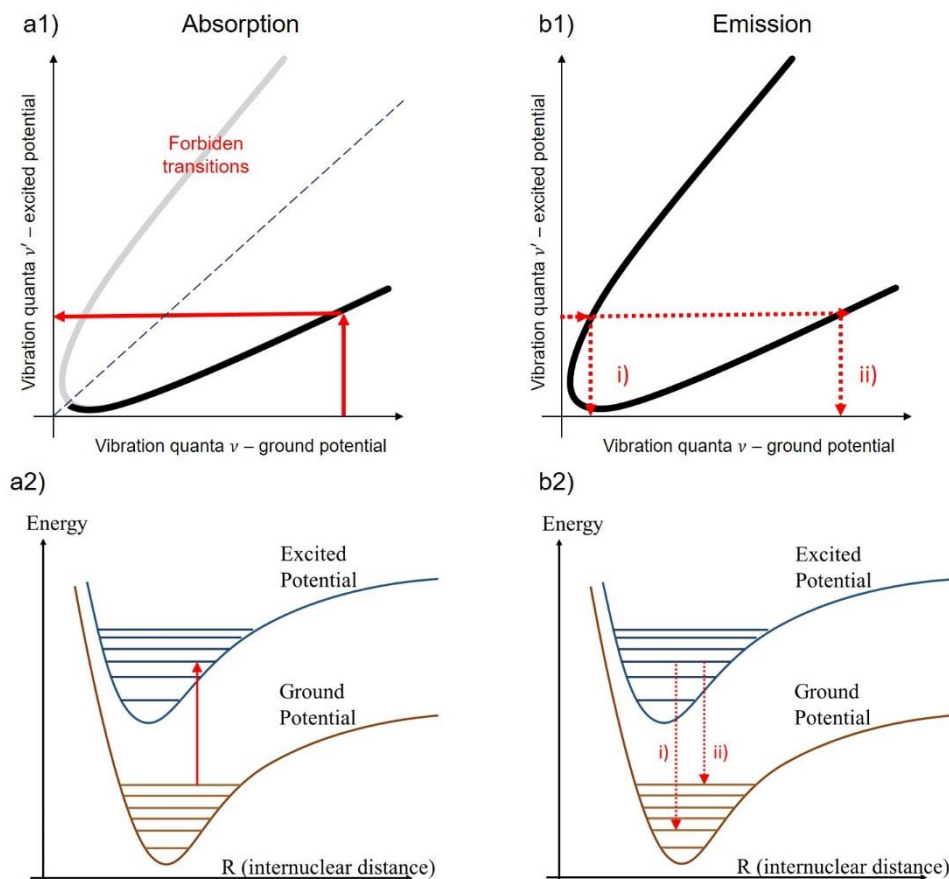


Figure 19 – A possible cycle of absorption and emission during the vibrational cooling process. In the absorption (fig. a1), the molecule is excited to a low-energy vibrational state of the excited potential (fig. a2). Then it spontaneously decays to the ground potential (figs. b1 and b2), either to the initial vibrational state (path i) or to a lower energy state (path ii). The net effect is to reduce the vibrational energy. The process ends when the molecule reaches the fundamental vibrational state, from which it cannot be excited.

Source: By the author.

In order to perform the vibrational cooling of  $\text{Rb}_2$  in our experiment, we use a QPhotonics QSDMI-1060 *super luminescent diode* (SLD). It has a central wavelength around 1060 nm, and its bandwidth (-3 dB) is of  $\sim 20$  nm. This broad operation range is enough to access a wide set of vibrational transitions between the  $X^1\Sigma_g^+$  and  $0_u^+$  potentials – the same potentials used for the photoassociation. This diode provides a net power from 50 to 300 mW, which is easily controllable by setting its operating current. The optical setup for both vibrational pumping and photoassociation will be presented in the next section.

Figure 20 shows the  $X^1\Sigma_g^+$  and  $0_u^+$  potentials, and figure 21 shows the Franck-Condon map for these potentials. The Franck-Condon factors were calculated using the software Level 8.0, developed by Robert Le Roy. (81) Notice that, in this case, the Condon parabola pattern is not very notable in the Franck-Condon map, due to the closeness of the two minima of the potentials (for the case of two identical potentials with same minima positions, the Condon

parabola degenerates into a straight line). However, the optical pumping process is still possible, because the spectral shaping (red dashed line) cuts the map in the region of the most likely transitions.

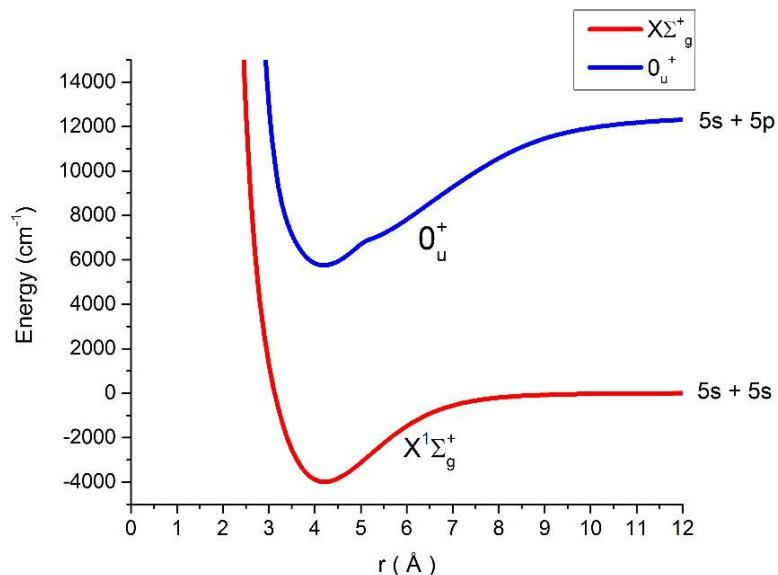


Figure 20 – Interaction potentials used in the vibrational cooling process.  
Source: By the author.

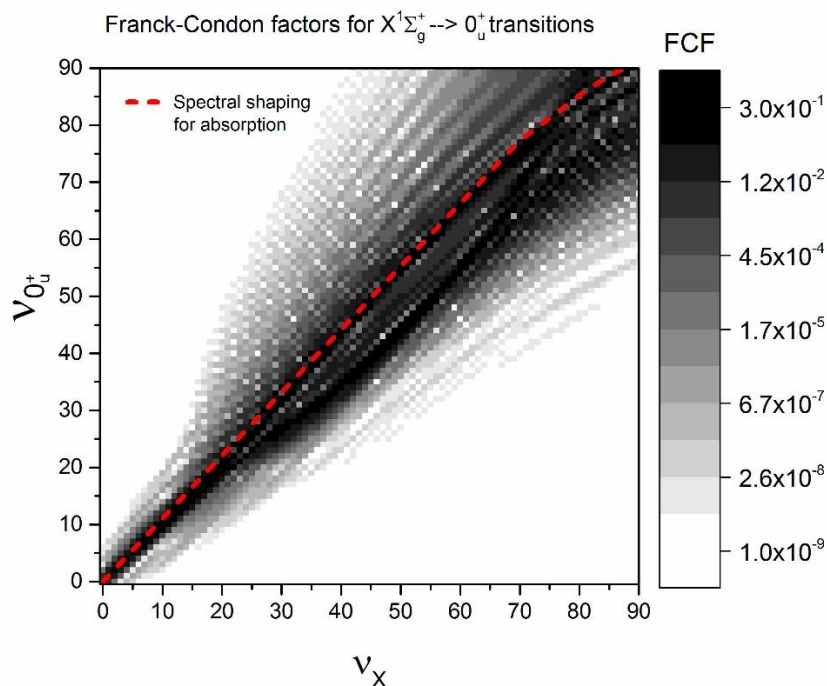


Figure 21 – Franck-Condon factors map for the two potentials used for the vibrational cooling. The red dashed line is the approximate spectral shaping cutoff of the broadband SLD, meaning that any transition above this line is inaccessible by the excitation light.  
Source: By the author.

### 4.2.3 Optical setup for photoassociation and vibrational cooling

The spectral shaping of the broadband SLD is performed with the same technique used by Viteau and collaborators (65), presented in section 3.3. The beam is spectrally dispersed by a diffraction grating, and then collimated by a cylindrical lens. An adjustable metallic mask is placed to partly block the beam, so that the highest frequencies (smallest wavelengths) are removed from the spectrum. To adjust the position of the mask, the shaped beam is monitored by a wide range spectrometer, and then the mask is moved until the right cutoff frequency is reached. For the case of  $\text{Rb}_2$ , it corresponds to any wavelength between 1042 nm (transition  $\nu = 1 \rightarrow \nu' = 0$ ) and 1048 nm (transition  $\nu = 0 \rightarrow \nu' = 0$ ).

The spectrally shaped SLD beam and the photoassociation beam are injected into the YAR high power amplifier, creating a single light beam, which is responsible for the optical dipole trap, and the photoassociation and vibrational cooling processes. This is a remarkable simplification on the experimental procedure, because there is no need to align a photoassociation and an optical pumping beam separately. We only need to align this single light beam in the magneto-optical trap region.

The optical setup is represented in figure 22. A small part of the PA light beam is sent to a HighFinesse WS7 Wavelength Meter, which measures its frequency. If it is necessary, the WS7 can also send a correction (feedback) signal to the laser piezoelectric controller to lock and stabilize the laser in a given frequency. The PA beam is then combined with the spectrally shaped SLD beam by a 50/50 beam splitter cube, from which both beams are sent to the YAR amplifier.

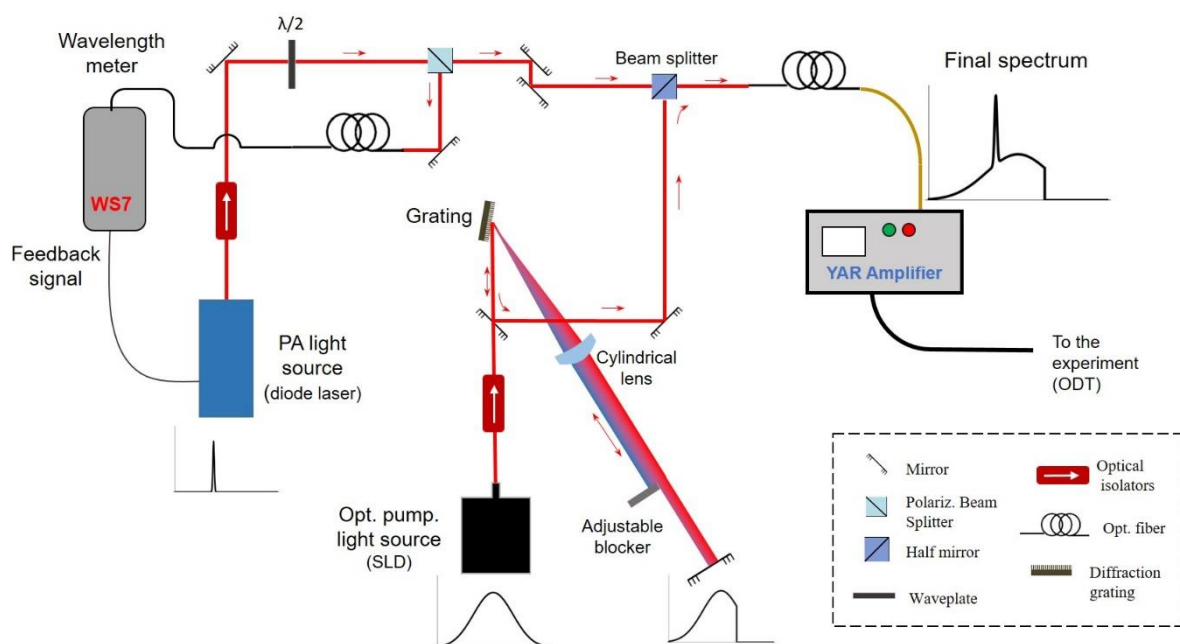


Figure 22 – Schematic representation of the optical setup for photoassociation and vibrational cooling. The SLD is spectrally dispersed by a diffraction grating, and then the higher frequencies are removed by a blocker. The photoassociation laser has its frequency measured and controlled by a wavelength meter. Both beams are combined and injected on the YAR high power amplifier, which produces the ODT. Source: By the author.

Figure 23 shows the combined spectrum (a) before and (b) after amplification. The input power of each beam is approximately the same ( $\sim 2$  mW each). By analyzing the amplified spectra, we estimate that around 75% of the output power is concentrated on the sharp band of the spectrum (the PA band), corresponding to a total of 37 W for the photoassociation. This power generates around  $4 \text{ MW/cm}^2$  at the crossed dipole region. The difference in the level ratio before and after amplification may be due to the gain function of the YAR amplifier, which is optimum only in the range from 1060 to 1070 nm.

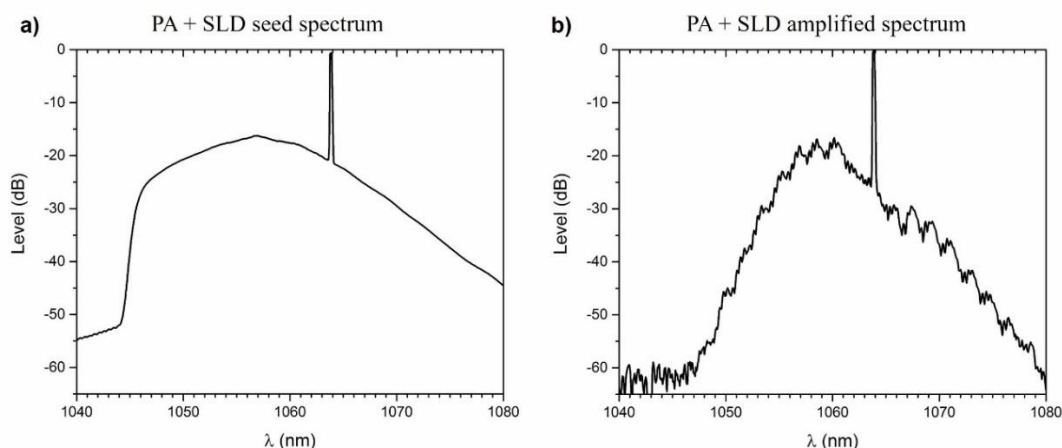


Figure 23 – Combination of the photoassociation and vibrational cooling light sources, before (a) and after (b) amplification by the YAR amplifier. The cutoff frequency is chosen to be between 1042 nm and 1048 nm, corresponding to the transitions  $\nu = 0 \rightarrow \nu' = 0$  and  $\nu = 1 \rightarrow \nu' = 0$  respectively.

Source: By the author.

### 4.3 The REMPI detection technique.

Once the molecules are produced in the MOT or ODT, they can be detected by resonance-enhanced multiphoton ionization (REMPI) process. This is a frequently used technique (82-83), and has the important feature of being selective to the vibrational state, i.e., the molecules are detected in one vibrational state at a time.

In this technique, a pulsed dye laser is used to excite molecules from the ground  $X^1\Sigma_g^+$  potential to an ionized state, in a one-color two-photon process (1 + 1 REMPI). (84) An intermediate state in the  $Z^1\Sigma_u^+$  potential is accessed by the first photon, whereas the second photon leads to the ionization (see figure 24). An electric field applied to the sample drives the ionized molecules towards a Channeltron® electron multiplier, which generates a measurable and short electric pulse for each ion that reaches it. Figures 24, 25 and 26 show respectively the  $\text{Rb}_2$  potentials involved on the REMPI process, the FCF map for the first photon absorption and an a schematic representation of the experimental setup for ionization.

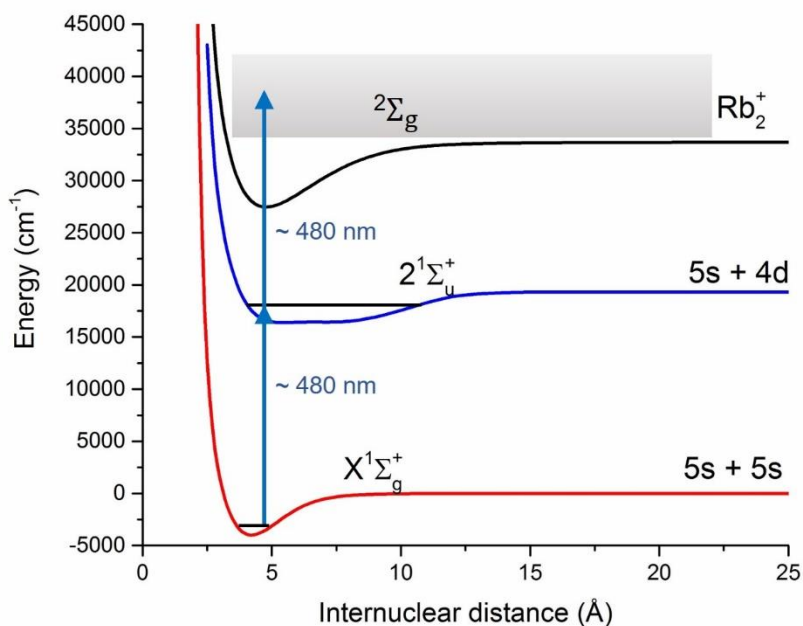


Figure 24 –  $\text{Rb}_2$  potentials involved on the two-photon one-color REMPI (ionization) process.  
Source: By the author.

Franck-Condon factors for REMPI first photon absorption

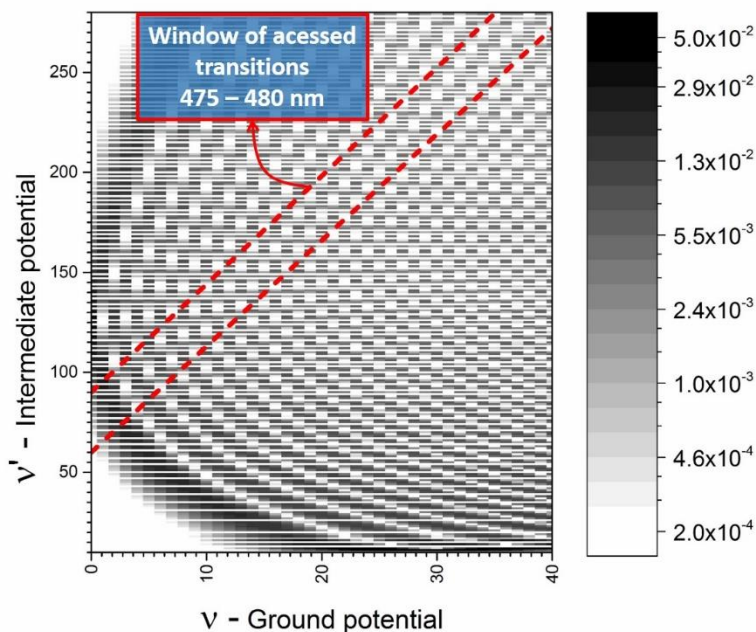


Figure 25 – Franck-Condon map for the ionization process (REMPI). The red dashed lines mark approximately the transitions accessed during the measurements with our pulsed dye laser. The laser spectral range was chosen to reach some of the strongest transitions from the fundamental vibrational state  $\nu = 0$ .  
Source: By the author.

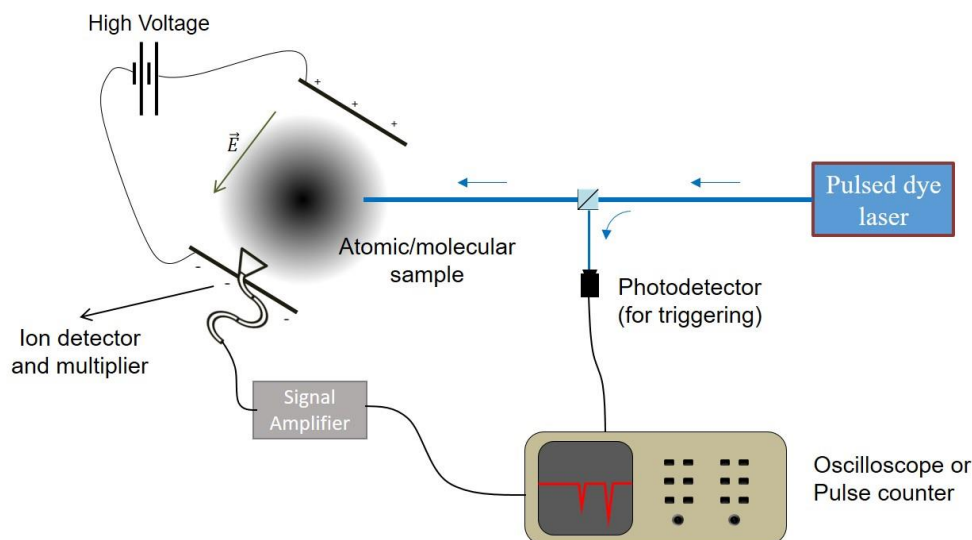


Figure 26 – Schematic representation of the REMPI experimental setup. The pulsed dye laser ionizes atoms and molecules in the sample, and each particle has a specific time-of-flight which depends on its mass. Each detected ion generates a pulse, which is viewed in an oscilloscope triggered by the laser pulses. This allows us to correlate the ions with the laser pulse times.

Source: By the author.

A pulsed laser is used to ionize the molecules because it allows to distinguish molecules from atoms by time of flight. Each particle that is ionized by the laser has a characteristic time-of-flight from the trap to the detector, and it scales with the square root of the particle's mass. This means that, if the atomic ions are detected at a time  $t$  after the laser pulse, diatomic molecular ions will be detected after a time  $\sqrt{2} \cdot t$  (given that the mass of a molecule is twice that of an atom). If the laser pulse width is much smaller than  $t$ , it is possible to distinguish the molecular from the atomic ions when they are detected. In this sense, REMPI is also a mass-spectroscopic technique.

We use a Jaguar – Continuum pulsed dye laser, pumped by the third harmonic of a Nd:YAG laser, to ionize the molecules. The laser operates at a repetition rate of 20 Hz and has a pulse width of 5 ns. The dye is a Coumarin 480 from Exciton, with a concentration chosen to have maximum intensity around 475 nm, ranging from 459 nm to 508 nm. (85) This range is where the strongest transitions from the fundamental vibrational state ( $v = 0$ ) of the  $X^1\Sigma_g^+$  were expected to be, according to the Franck-Condon factors (figure 25).

The pulses from the Channeltron® ion detector are amplified and then monitored in an oscilloscope. A small fraction of the pulsed light is collected by a photo detector, whose signal is used to trigger the oscilloscope. In this way, we can see the ions that are detected just after the laser pulse (a few microseconds, which is the typical time-of-flight of  $\text{Rb}^+$  and  $\text{Rb}_2^+$  ions). This setup is used to align the pulsed laser with the crossed ODT region. When the beam is

adequately aligned and the PA laser is in the correct frequency, the signal as seen in the oscilloscope is similar to figure 27:

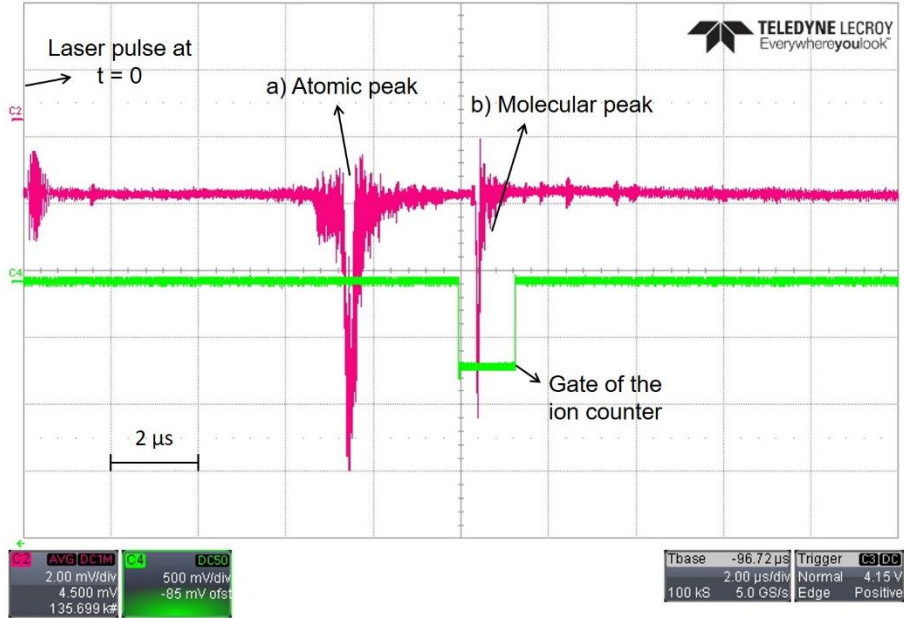


Figure 27 – Signal of the ion detector, as seen in the oscilloscope. The trigger is the laser pulse, and an average of 10 pulses is taken. The ratio between the molecular (b) and the atomic (a) peak delays is approximately  $\sqrt{2}$ , which is in agreement with the square root of the mass scaling.

Source: By the author.

The two negative peaks correspond to  $\text{Rb}^+$  atomic ions (a) and  $\text{Rb}_2^+$  molecular ions (b). Notice that the atomic peak is at  $\sim 7.5 \mu\text{s}$  after the laser pulse, whereas the molecular peak is at  $\sim 10.5 \mu\text{s}$ . This is in agreement with the square root scaling mentioned above, because:

$$\frac{t_{mol}}{t_{at}} \approx \frac{10.5}{7.5} = 1.4 \approx \sqrt{2} \quad (48)$$

Once the alignment is correct, the ion signal and the pulsed light trigger are sent to a Stanford Research SR400 pulse counter. This equipment is able to count the ion pulses that arrive only in a specific time window (gate) after the laser pulses. The information viewed in the oscilloscope is used to set the gate in the molecular peak only, which avoids counting atoms and many other spurious ions that are uncorrelated to the laser pulses.

## 4.4 Control of the experiment

The control of the experiment is performed with the use of National Instruments hardware, boards, three computers and LabVIEW software. With this structure, we are able to control several parameters (such as the acousto-optic modulators, automatic optical shutters and magnetic fields) with a temporal precision of  $100 \mu\text{s}$ . In this section, we explain briefly the following control software and sequences: the “Startup”, the REMPI sequence and the ODT loading and imaging.

### 4.4.1 “Startup” – constant parameters

The simplest control protocol is the “Startup” program, which sets all the parameters to constant values. All the parameters are either analogic or digital outputs from a National Instruments board, which is connected to the control computer; the output tensions are sent to their respective devices by cables. With this software, we can load a static MOT by setting the trapping and repumping beams to their maximum power\*, and the magnetic fields on (this set of conditions will henceforth be referred as “MOT conditions”). The user interface of the Startup program is shown in figure 28:

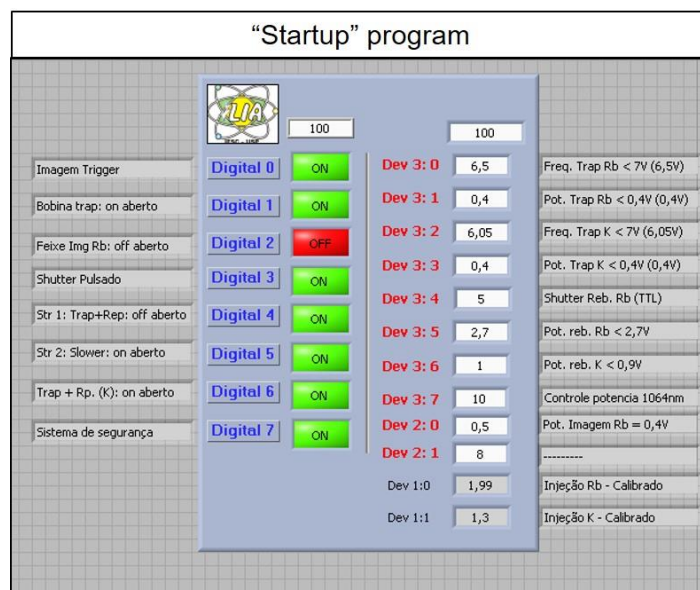


Figure 28 – Startup program interface. The program simply sets the controllable parameters to a constant value, which allows us to load a static MOT.

Source: By the author.

\* The power of the trapping and repumping beams, as well as their detuning, are controlled by the power and the frequency of their respective AOMs.

#### 4.4.2 REMPI experiments control sequence

For the REMPI experiments performed in the MOT, there is a periodic temporal sequence to be followed. The sequence synchronizes some processes performed on the MOT with the pulses from the pulsed REMPI dye laser, and is represented in figure 30. The first (and longest) step is to load the MOT, letting the parameters at the MOT conditions. This is followed by a brief detuning on the trapping light and decreasing of the repumping light power, which should reduce the temperature and increase the density of the MOT. After this step, the repumping light is turned off, so the atoms are transferred to the hyperfine  $F = 2$  level of the  $5s$  state (see figure 12)<sup>†</sup>. At this stage, it is expected that the PA laser starts producing molecules, because it is tuned to photoassociate atomic pairs at  $F = 2$ . Finally, a trigger is sent to the REMPI laser, requesting a single pulse from it. By this time (and 1 ms after), the MOT lights are turned off, because remarkable signal-to-noise ratio is obtained with this procedure. The extra 1 ms after is left to account for the delay between the electric pulse sent to the laser and the actual light pulse. The described sequence is repeated in loop, with a period of 50 ms (20 Hz repetition rate).

The LabVIEW program to perform this sequence was made by the author, adapted from the program used to load the ODT, and its interface is shown in figure 29:

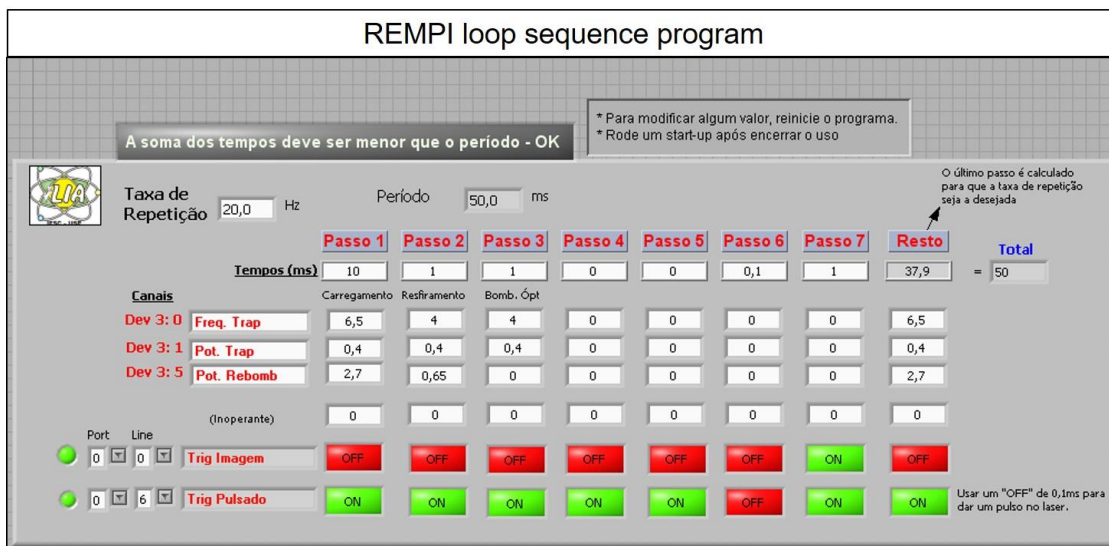


Figure 29 – LabVIEW program interface to control the REMPI experiment on the MOT.

Source: By the author.

<sup>†</sup> This state is preferable for the ODT, as it avoid losses due to hyperfine state changing collisions. Although we are not loading the ODT in this experiment, we prefer to perform it with the hyperfine level that will be used in the ODT in future experiments.

	MOT loading 47.9 ms	MOT cooling 1 ms	Opt. pumping to F = 2 1 ms	REMPI Laser pulse 0.1 ms	Acquisition 1 ms
Trapping laser detuning	-20 MHz	-35 MHz	-35 MHz		
Trapping laser power	~8 mW/cm <sup>2</sup>	~8 mW/cm <sup>2</sup>	~8 mW/cm <sup>2</sup>	OFF	OFF
Repumping laser power	~1.6 mW/cm <sup>2</sup>	~60 $\mu$ W/cm <sup>2</sup>	OFF	OFF	OFF
REMPI laser trigger				PULSE	

Figure 30 – Representation of the periodic sequence for the REMPI experiment on the MOT. The first step is the MOT loading, with all parameters at MOT conditions. Following steps are the cooling of the MOT (to increase density) and the transference of the atoms to F = 2, which allows the photoassociation. The ionization dye laser is then pulsed, generating the ions, with the MOT lights off. An extra time is given to ensure that the ionization will occur with no MOT lights.

Source: By the author.

#### 4.4.3 Optical dipole trap loading and imaging

The ODT loading process also requires a precise temporal sequence of events, which is controlled by a LabVIEW program. The first step is to load a MOT during a time of 6 to 10 s, which is enough to attain an order of  $10^8$  atoms trapped in the MOT and a density of  $2 \cdot 10^{10} \text{ cm}^{-3}$ . (68) In the sequence, the ODT high power laser is turned on, and the trap is submitted to a process of cooling by reducing both trapping and repumping light intensities, as well as detuning the trapping light further from the resonance. This process increases the efficiency of the ODT loading, because the temperature of the atoms in the normal (static) MOT ( $\sim 0.3 \text{ mK}$  (68)) is comparable to the ODT depth ( $\sim 1.4 \text{ mK} \cdot K_B$  (76),  $K_B$  is the Boltzmann constant). During the 50 ms of this stage, the atoms are loaded to the ODT. The next step is to transfer the atoms to the F = 2 hyperfine level, to avoid losses due to hyperfine state-changing collisions (86), which is achieved by turning off the repumping light. At this time, the MOT magnetic field are also turned off. After this step, all the MOT lights are turned off, leaving only the ODT laser on. This step is the “lifetime” of the ODT.

Differently to the MOT, the number of trapped atoms in an ODT decreases with time, due to the existence of some loss mechanisms (like collisions with hot background particles) and the absence of any extra loading mechanism. Under favorable conditions (like high quality vacuum and good beam alignment), our ODT can last up to 5 s until most of the atoms are lost.

Figures 31 and 32 show the LabVIEW program that controls the loading and imaging of the ODT and a summary of the experimental sequence.



Figure 31 – Front panel of the LabVIEW program to control the ODT loading sequence. Some of the parameters in this print may not be set to the actual values.

Source: By the author.

	MOT loading 6000 to 10000 ms	ODT loading 50 ms	Opt. pumping to F = 2 1 ms	Optical dipole trap 20 to 5000 ms	Fluorescence Image 1 ms
Trapping laser detuning	-20 MHz	-35 MHz	-35 MHz		-20 MHz
Trapping laser power	~8 mW/cm <sup>2</sup>	~8 mW/cm <sup>2</sup>	~8 mW/cm <sup>2</sup>	OFF	~8 mW/cm <sup>2</sup>
Repumping laser power	~1.6 mW/cm <sup>2</sup>	~60 μW/cm <sup>2</sup>	OFF	OFF	~1.6 mW/cm <sup>2</sup>
ODT laser power	OFF	50 W	50 W	50 W	OFF
MOT Magnetic Fields	ON	ON	OFF	OFF	OFF
Camera Trigger					Pulse

Figure 32 – Sequence of events for the loading and imaging of the optical dipole trap. After loading a MOT for some seconds, the parameters are changed in order to reduce the atoms’ temperature. This allows for an efficient loading of the optical dipole trap. After this step, the repumping light is turned off to transfer the atoms for the F = 2 hyperfine level. The MOT is then turned off, leaving the atoms to be trapped only in the ODT. The ODT shape and population can be proved by a fluorescence image.

Source: By the author.

Even if the desired experiment is not performed on the ODT, its loading process is still very important to verify the alignment of the high power laser beam with the densest region of

the MOT (remember that this is also the beam that promotes photoassociation and vibrational cooling), as well as the correct overlapping between the two crossed arms of the beam. To prove the ODT quality (and, as a consequence, the quality of the experiment as a whole), we use a fluorescence imaging technique, which allows us to analyze the shape and the density of the ODT.

The fluorescence image is acquired by a digital camera placed in one of the windows of the main vacuum chamber, pointing to the trap region. This camera is connected to a computer which is dedicated to image acquisition, and the image is processed in a LabVIEW program. This program waits for a trigger signal to be sent by the ODT control program and then acquires the image. The trigger signal is sent after an indicated time that is given for the ODT (see figure 32). Simultaneously to the image trigger, the trapping and repumping lights are set to MOT conditions, causing the atoms to emit light by fluorescence. Figure 33 shows two examples of fluorescence images of the ODT, comparing its quality in two conditions.

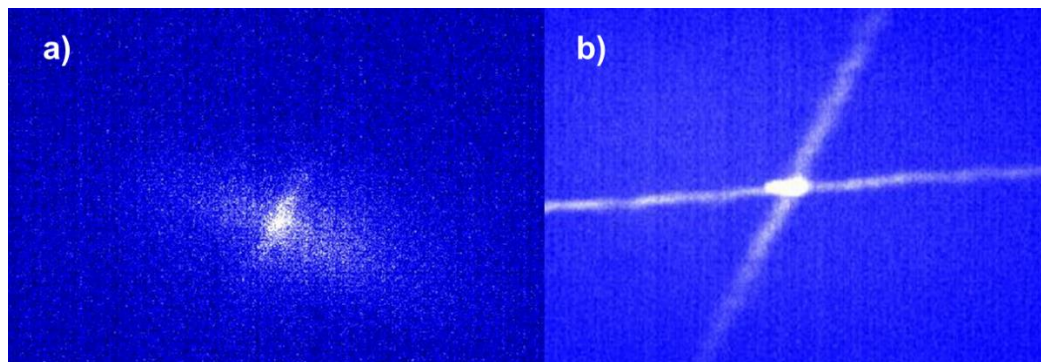


Figure 33 – Two examples of ODT images, showing a “bad” (a) and a “good” (b) trap. In a), only one of the beams are visible, meaning that the overlapping between the two arms is not correct. In b), the two arms are visible and a brighter spot at the center is present, indicating that the arms are correctly overlapped.

Source: Adapted from MENEGATTI. (68)



## 5 RESULTS AND DISCUSSION

In this chapter, the first section is dedicated to a discussion on previous results relevant to this dissertation. (78) In the following sections, we present a description of the measurement in details and followed by a discussion about it. Each result is preceded by a description of the measurement details and followed by a discussion about its features. Finally, the last section provides a more detailed discussion about the vibrational cooling to the fundamental state, which deserves particular attention due to its importance and difficult interpretation.

### 5.1 Preliminary results

The first evidence that it is possible to photoassociate  $\text{Rb}_2$  with a high power laser was obtained in 2012 by our group. (78) In that experiment, the ODT was provided by a broadband fiber laser around 1071 nm, with a *full width at half maximum* (FWHM) bandwidth of 1.5 nm and maximum power of 40 W. The Rb atomic population as a function of time was measured using imaging techniques, and a non-exponential decay was observed (see figure 34). The decay curve could be fitted by a model that considers both single-body and two-body losses (i.e., collisions between Rb atoms and background atoms, and collisions between two Rb atoms, respectively). According to theoretical calculations, these two-body losses (which are usually negligible for most ODTs in which the atoms are in their lowest hyperfine state (72)) could be explained by short-range photoassociation to the  $0_u^+$  coupled states. In the case of  $^{85}\text{Rb}$  atoms, the vibrational state  $\nu' = 136$  of the  $0_u^+$  potential could be accessed within the bandwidth of the fiber laser.

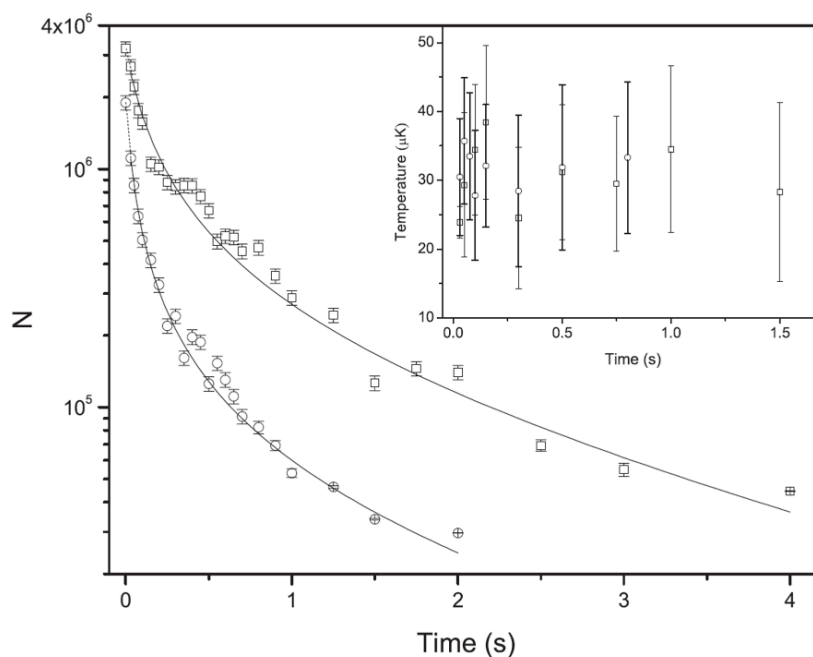


Figure 34 – Number  $N$  of atoms in the ODT as a function of time, for  $^{87}\text{Rb}$  (circles) and  $^{85}\text{Rb}$  (squares) atoms. The solid line represents a curve fitting that considers both single-body and two-body losses, resulting in a clearly non-exponential decay. The two body losses can be explained by photoassociation. The inset shows the temperature over time, and the nearly constant value indicates that no relevant losses due to thermalization occurred.

Source: MENEGATTI et al. (78)

However, the fixed bandwidth and central wavelength of this laser did not allow for us to control the photoassociation process. In addition, due to the distribution of the laser power over the 1.5 nm bandwidth, the molecular formation rate was low and insufficient for our purposes. These limitations, combined with the possibility of photoassociation by a high power beam, motivated us to change this old laser for the YAR amplifier as described in section 4.2.3, which would allow us to tune different photoassociation transitions with high resolution.

Our first results with the new setup were obtained by the end of 2015. These results were based on two different experiments, both concerning to the atomic population (therefore indirect measurements), and were already presented by Henry Passagem (76) in his dissertation.

The first experiment involved the measurement of the MOT fluorescence as a function of the PA laser frequency, obtaining a trap loss spectrum. The MOT repumping light was chopped ON and OFF at a 500 Hz repetition rate, allowing us to use a lock-in amplifier to precisely measure the MOT fluorescence intensity. The YAR amplifier was seeded only by the photoassociation laser, which had its wavenumber scanned around  $9362.8\text{ cm}^{-1}$  (1068.1 nm) and  $9379.5\text{ cm}^{-1}$  (1066.2 nm). These peaks correspond respectively to the  $\nu' = 137$  and  $\nu' = 138$  transitions to the  $0_u^+$  potential (considering  $F = 2$  as the initial atomic hyperfine state), as

predicted by calculations performed by our collaborators from Olivier Dulieu's group (see table 2). The results are shown in figure 35:

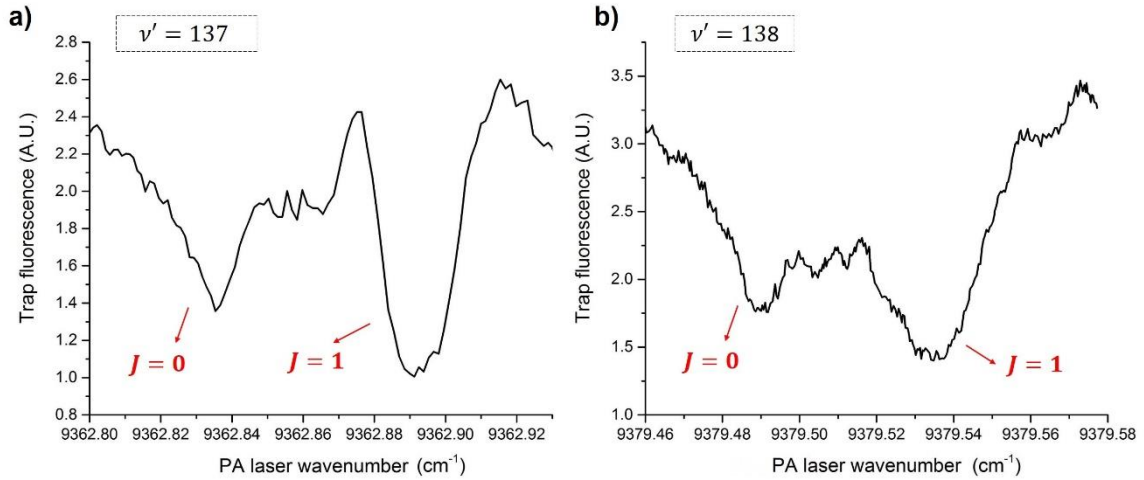


Figure 35 – Trap loss spectra of the magneto-optical trap, as a function of the PA laser wavenumber. The measurements were performed both around  $\nu' = 137$  (a) and  $\nu' = 138$  (b) transitions. The negative peaks indicated by red arrows are attributed to the photoassociation by the high power laser.

Source: By the author.

The red arrows show where the MOT fluorescence is considerably reduced, meaning that a frequency-dependent loss mechanism is present. We interpret this mechanism as the photoassociation, because atomic pairs that are converted to molecules are no longer trapped by the MOT. This is, however, an indirect measurement, and the shape of the spectrum, as well as the absolute position of the peaks, are subject to some imprecision.

The second experiment was a reproduction of the ODT population decay measurement performed in 2012. The atomic population at each instant was measured by fluorescence imaging (described in section 4.4.3) under two different wavenumbers of the PA seed laser:  $9379.52 \text{ cm}^{-1}$  (on resonance) and  $9390.41 \text{ cm}^{-1}$  (off-resonance). Results are in figure 36:

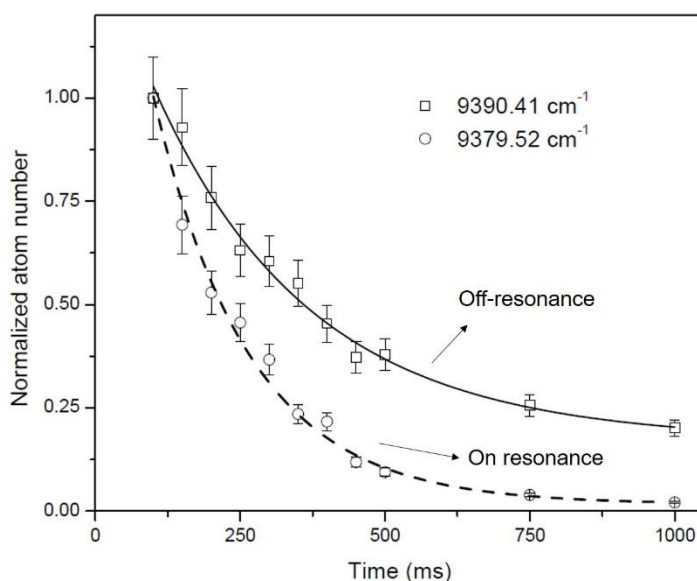


Figure 36 – Lifetime measurements performed with the new setup (using the YAR amplifier instead of the broadband laser).

Source: By the author.

Notably, the populational decay is greater when the laser is resonant, indicating that the photoassociation is also possible with the new laser, with the advantage of having a tunable frequency. It should be noticed that, as the atoms are trapped in the ODT region, power broadening effects may cause off-resonance photoassociation. For this reason, the off-resonance wavenumber was chosen to be very distant from resonance, avoiding this effect.

These preliminary results, although subject to considerable uncertainty, had fundamental importance to guide the next steps of our experiments, including the direct measurements that will be presented in the following sections.

## 5.2 Ionization spectrum as function of the photoassociation laser wavenumber

In the next experiment, we implemented the REMPI technique to detect molecules in the lowest vibrational states of the  $X^1\Sigma_g^+$  fundamental potential.

The experiment is performed in the MOT, and the trapping and repumping lights are modulated at a 20 Hz rate, with the sequence explained in section 4.4.2 (figure 30). The pulsed ionization laser is set to a fixed wavelength, and the PA laser wavenumber is scanned around the same range as used in the trap loss experiment for  $\nu' = 138^*$ . The broadband SLD for vibrational cooling is not used at this stage. For each point, we collect the ions from 300 laser

\* We have tried to perform the same experiment for  $\nu' = 137$ , with no success.

pulses, and the presented graph is an average of 4 sweeps. To enhance the signal-to-noise ratio, the pulsed laser is set to the wavelength  $\lambda_{PI} = 479,59$  nm, in which the molecular signal is very intense (reaching a maximum of 4 molecules per pulse). Figure 37 shows the result of the average scan, compared to the trap loss spectrum of the same state:

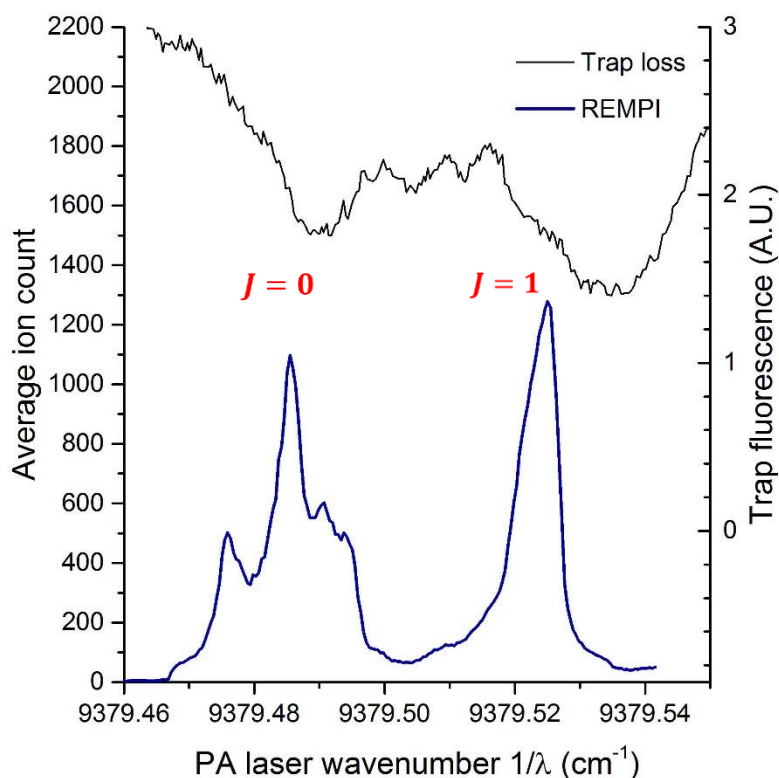


Figure 37 – Molecular ionization signal (REMPI) as a function of the photoassociation laser wavenumber, and comparison with the previously shown trap loss spectrum for  $v' = 138$ . Each peak correspond to a different rotational state ( $J = 0$  and  $J = 1$ ) from this vibrational quantum number.

Source: By the author.

First of all, we must compare the trap loss and ion spectrum. Despite some deviation in the peak positions, there is a good agreement between both results. We should also point out that, in both spectra, there are two peaks, which are interpreted as the rotational splitting from vibrational level  $v' = 138$  of the excited potential. The expected wavenumber of the first peak, which corresponds to the fundamental rotational level ( $J = 0$ ), is  $9379.52$   $\text{cm}^{-1}$ , according to theoretical predictions from Dulieu's group. Although the absolute discrepancy from the measured value is at the order of the rotational splitting, the relative error is very small ( $\approx 10^{-6}$ ), showing good agreement. Besides, the absolute value of the measured wavenumbers are subject to some slow "drifting" of  $\pm 0.02$   $\text{cm}^{-1}$  during 1 to 2 days, probably due to fluctuations

in the wavelength meter calibration. Therefore, the absolute position of the peaks are not very reliable at this precision.

Despite this slow drifting of the calibration, the scans were performed in the time of  $\sim 1$  hour, meaning that the separation between the peaks is very reliable, and it contains information about the rotational splitting. From the theory (36), we know that the energy of each rotational level is given by  $B_\nu \cdot J(J + 1)$ , where  $B_\nu$  is the *rotational constant* of the vibrational level  $\nu$ , and  $J$  is the rotation quantum number. For the states  $J = 0$  and  $J = 1$ , the separation is then  $2B_\nu$ . Considering  $\nu' = 138$  of the  $0_u^+$  potential, theoretical predictions provided by Dulieu's group estimate that  $B_{138} = 0.015 \text{ cm}^{-1}$  (or equivalently, in frequency, 0.455 GHz), resulting in a separation of  $0.030 \text{ cm}^{-1}$ . Our experimental data shows that the separation between  $J = 0$  and  $J = 1$  is about  $0.031 \pm 0.001 \text{ cm}^{-1}$  (both trap loss and REMPI experiments yield this value, although the error is estimated from the REMPI data), in reasonable agreement with the theory.

Finally, we should notice that the  $J = 0$  peak presents a notable structure around it, which is very similar to molecular hyperfine splitting lines already detected in previous works. (45) In our particular case, the absence of this structure in the other peak suggests that the splitting is due to an accidental degeneracy with a level from another molecular symmetry, similarly to what was reported in a recent work. (87)

### 5.3 Molecular signal as a function of PA and REMPI laser intensities

To test the proposed mechanisms for photoassociation and REMPI processes, we can measure the molecular ionization signal as a function of the PA beam and ionization laser intensities, respectively. For each case, a power law dependency is expected, with the exponent close to the number of photons involved on the mechanism.

In this experiment, both PA and ionization laser frequencies are set to a fixed value, for which the REMPI signal is optimal, and the SLD is not injected to the YAR amplifier yet. To vary the PA beam intensity at the sample, we change the amplifier output power from 5 W to 50 W, which can be easily set by its front panel interface. Figure 38 shows the REMPI molecular signal as a function of the YAR power normalized by its maximum:

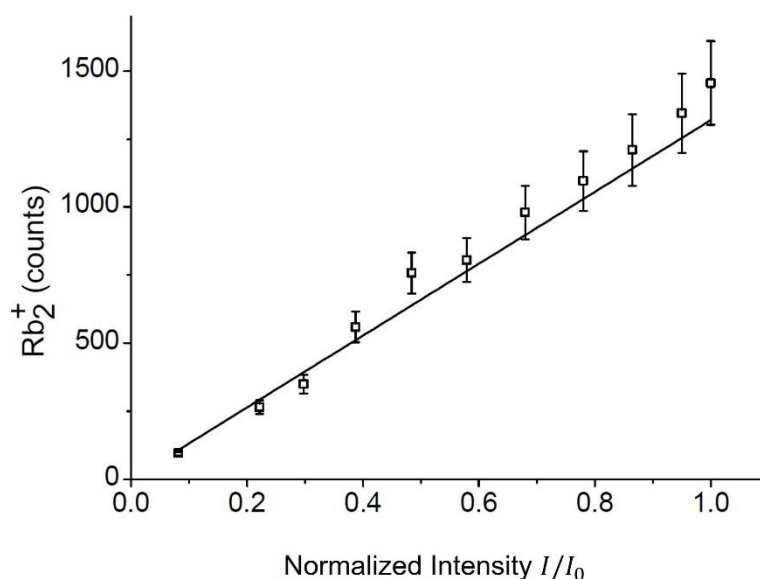


Figure 38 – Molecular ionization signal as a function of the PA laser intensity, which can be varied by changing the output power of the YAR amplifier.  $I_0$  is the intensity that corresponds to the maximum output power of the YAR amplifier (50 W). The linear behavior is expected, as the PA is a single-photon mechanism.

Source: By the author.

The linear PA intensity dependence shows that, indeed, the photoassociation occurs through a single-photon mechanism.

To vary the REMPI dye laser intensity, we have to change the current of the Nd:YAG laser that pumps it. To measure the actual laser power, we have to subtract the dye fluorescence that composes the total spot (and does not contribute to the REMPI process). This is performed by first measuring the total spot power, and then measuring the power of the spot with the laser cavity blocked. The last measurement provides the fluorescence-only power, and can be subtracted from the first measurement to yield the laser-only power. The REMPI molecular signal as a function of the REMPI laser power (normalized by its maximum) is showed in figure 39:

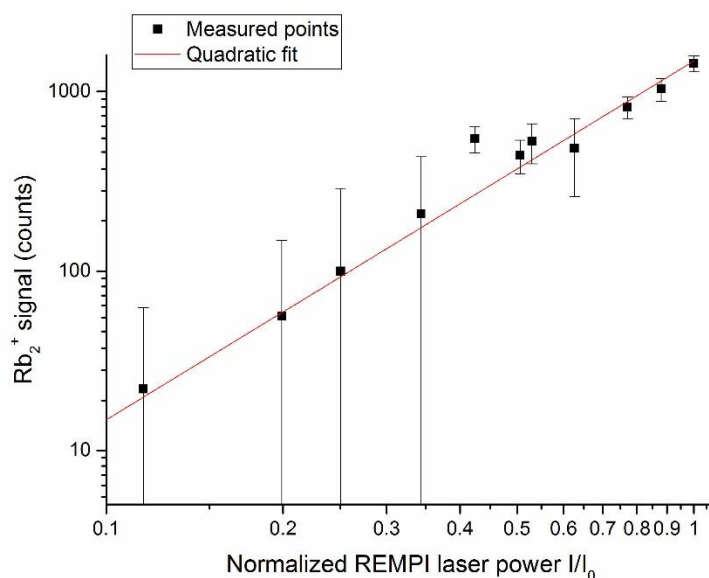


Figure 39 – Ionization signal as a function of the ionization laser power. The two-photon mechanism of the 1+1 REMPI process is compatible with the measured points.

Source: By the author.

A power law fit of the experimental points, in which the exponent is left to be calculated, yields a value between 1 and 2, with high uncertainty (probably due to the data fluctuations). However, it is noticeable that the points can be fitted by a parabola, a result that is compatible with the two-photon mechanism of the 1 + 1 REMPI process (see figure 24 in section 4.3).

#### 5.4 Molecular spectra as a function of the REMPI laser wavelength

As mentioned in section 4.3, the REMPI technique has the important feature of selecting the vibrational states of the molecules of the ground state potential. This happens because each pair of vibrational levels  $\nu \rightarrow \nu'$  at the first photon absorption has a different transition energy, so different transitions can be tuned by varying the ionization laser frequency. Furthermore, the REMPI molecular spectrum as a function of this laser frequency should provide us information about the vibrational distribution of the molecules in the ground potential, and therefore it must be sensible to the presence of the shaped SLD (the light that optically pumps the molecules to the fundamental vibrational state).

To perform this experiment, the PA laser wavenumber is set to one of the peaks shown in figure 37, in order to maximize the molecular formation rate. The MOT is modulated as explained before, and the experiment is now performed for two conditions: one with the SLD pumping light and other without it. The REMPI laser wavelength is scanned at steps of

$\sim 0.004$  nm, and each point is a collection of 300 laser pulses. The results for both conditions are shown in figure 40:

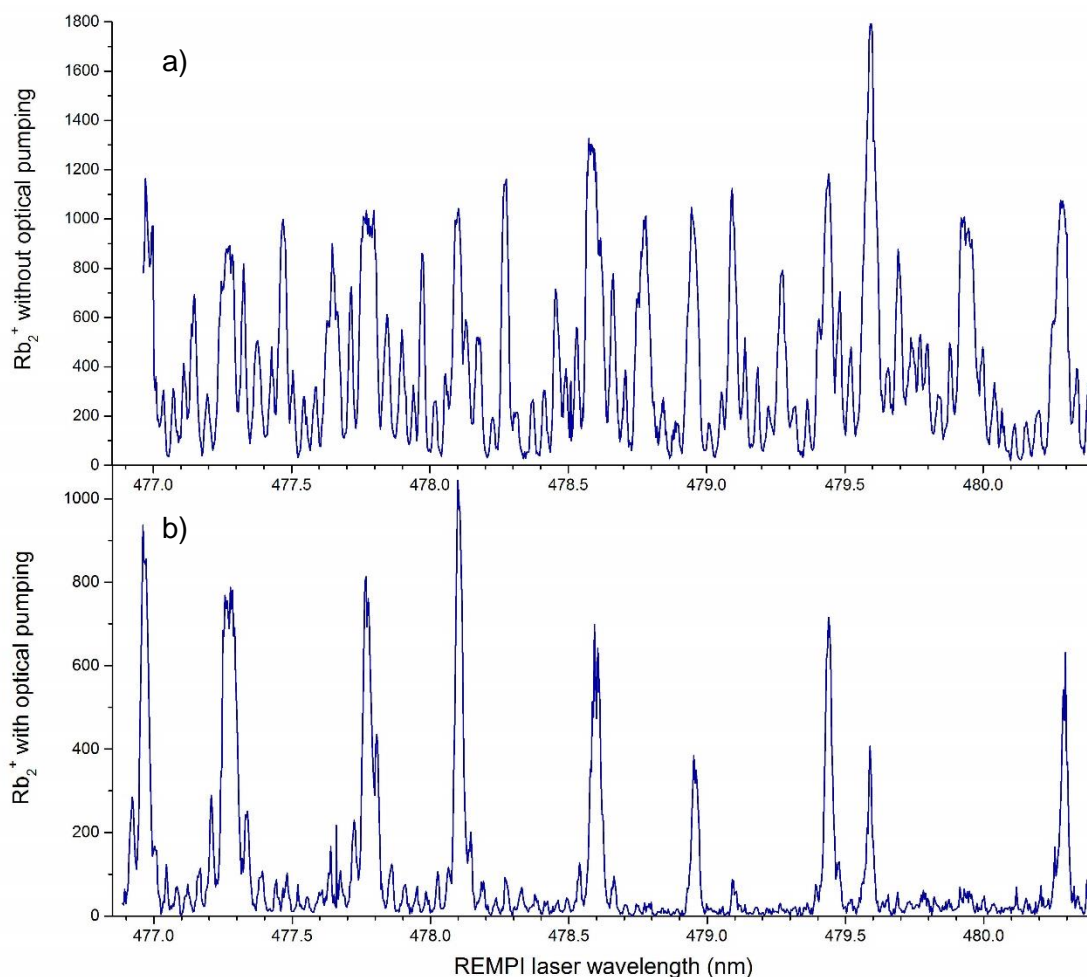


Figure 40 – Molecular ionization signal for REMPI laser wavelength scan, in the absence (a) and presence (b) of optical pumping by the shaped broadband SLD light. Notably, the number of peaks is smaller when the optical pumping is present, meaning that the number of occupied states is reduced in this case.

Source: By the author.

Despite the complexity of both spectra, the most noticeable feature is that, when the optical pumping by the SLD is present, the number of peaks is drastically reduced. This is a strong evidence that the number of populated vibrational states is much smaller after the optical pumping, which means that the optical pumping process is taking place. We should notice that, in the spectrum of the optically pumped sample, some residual peaks are still present, which may be due to other residually occupied states added to some intrinsic noise of the measurement.

Although the qualitative comparison of the two spectra is immediate, a precise interpretation in terms of occupied vibrational states is a much more difficult task. In order to

do this, we need a very accurate map of the possible transitions in this spectral window, including their wavelength and Franck-Condon factors. At the present moment, the only available map is based on *ab-initio* data from the  $(2)^1\Sigma_u^+$  potential, provided by our collaborators from Dulieu's group, and is known not to be very precise. Based on this data, we have simulated the expected vibrational spectrum in the same window of our measurements.

The simulation is constructed as follows: each transition from the theoretical data is represented as a Gaussian peak centered in the transition wavelength, with a  $1/e$  half width of 0.011 nm (estimated from the experimental peaks and attributed to the dye laser bandwidth). The amplitude of the peak is a product of the transition's Franck-Condon factor, the expected population in the correspondent vibrational state and an arbitrary scaling factor which is the same for the whole spectrum. To reduce the complexity, only transitions with FCF above  $10^{-4}$  were considered. The resulting simulated spectrum for the case of no optical pumping is shown in figure 41:

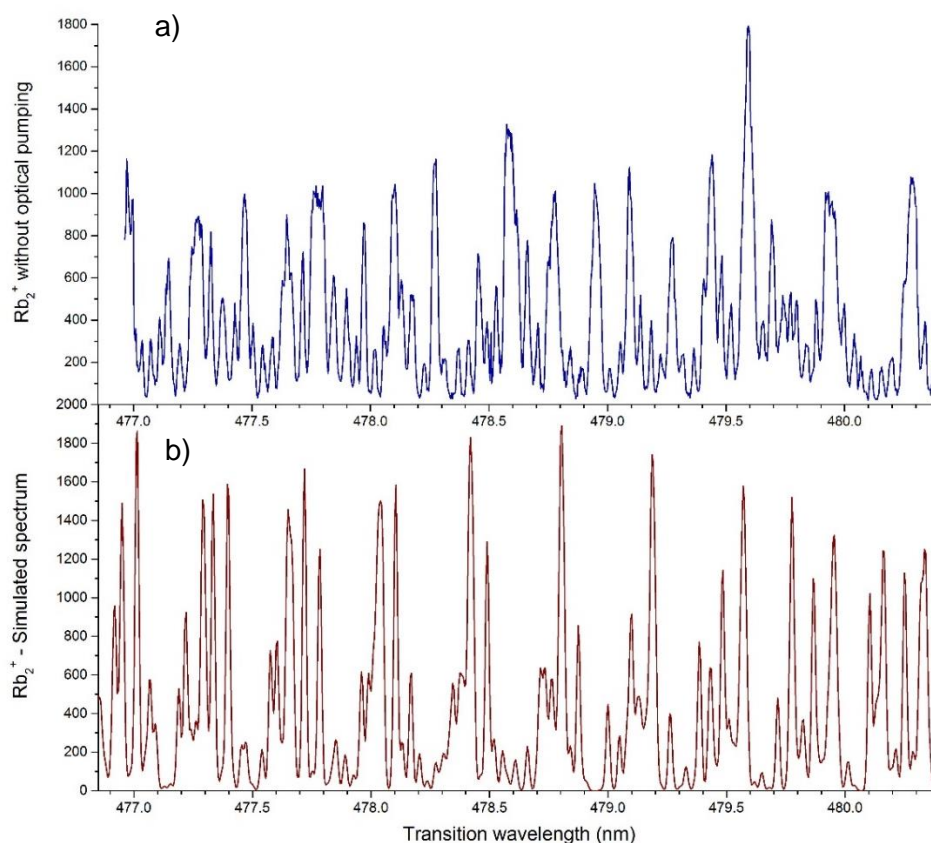


Figure 41 – Comparison between the experimental spectrum (a) and a simulated spectrum (b), based on *ab initio* calculations performed by Dulieu's group. The simulation considers the vibrational distribution and the FCFs shown in figure 25 (section 4.3). Although the simulation could not reproduce the experimental spectrum (discussion in the text), some qualitative features such as peak density and average separation are similar.

Source: By the author.

Some features of the simulation, including the peak density and the average distance between the main peaks, are very similar to the experimental spectrum. However, it is not possible to make a simple equivalence between the two spectra. This may be due to the inaccuracy of the theoretical map, but could also be due to differences in the actual vibrational distribution, due to some unexpected optical pumping effect. Considering this, we have tried to fit the experimental spectrum taking the populations in each vibrational state as variables, but the fitting process did not converge, as it had too many free parameters.

Another remark concerning the discrepancies is that, in this simple simulation, we do not consider the spin-orbit coupling of  $2^1\Sigma_u^+$  with the  $2^3\Pi_u$ , another potential that belongs to the same atomic asymptote; the effects of this coupling had been observed in another work (83). Finally, the dye laser's wavelength is measured at some points by a spectrometer, and then linearly interpolated to the whole measurement range. The points are well fitted to a linear function, but the interpolation method estimates a 0.01 nm error for the final value – at the order of the peak widths. Although small, it may contribute to the disagreements.

## 5.5 Discussion about the vibrational cooling

Due to the limitations of the theoretical model, we need to find an alternative way to interpret the REMPI laser scan spectrum for the case with optical pumping. We will use an indirect argument, based only on some general features of the theoretical spectrum, since the exact positions of the peaks are not very reliable.

We first need to observe the Franck-Condon map for the ionization in detail, which is shown in figure 25 (section 4.3). Starting from a single vibrational state  $\nu$  of the ground potential, there are several transitions that have low Franck-Condon factors; in general, for each three consecutive transitions, two of them are “strong” (i.e., have a high Franck-Condon factor, greater than  $1 \cdot 10^{-3}$ ) and one is “weak” (i.e., it has low Franck-Condon factor, typically less than  $10^{-6}$ ). This peculiar behavior can be noticed by the horizontal white lines on the map.

By observing our experimental spectrum with optical pumping (figure 40, lower graph), we can notice that the peaks appear to be grouped by pairs. This is compatible to the FCF behavior described here, which means that for each three consecutive transitions, one of them is “missing” due to poor Franck-Condon overlap. Assuming this, we label the transitions according to this rule (figure 42), and then plot the transition wavenumbers as a function of the vibrational quanta (figure 43). This plot can be compared to the theoretical data. The quantum number  $\nu'_0$  is unknown, but supposed to be between 50 and 100.

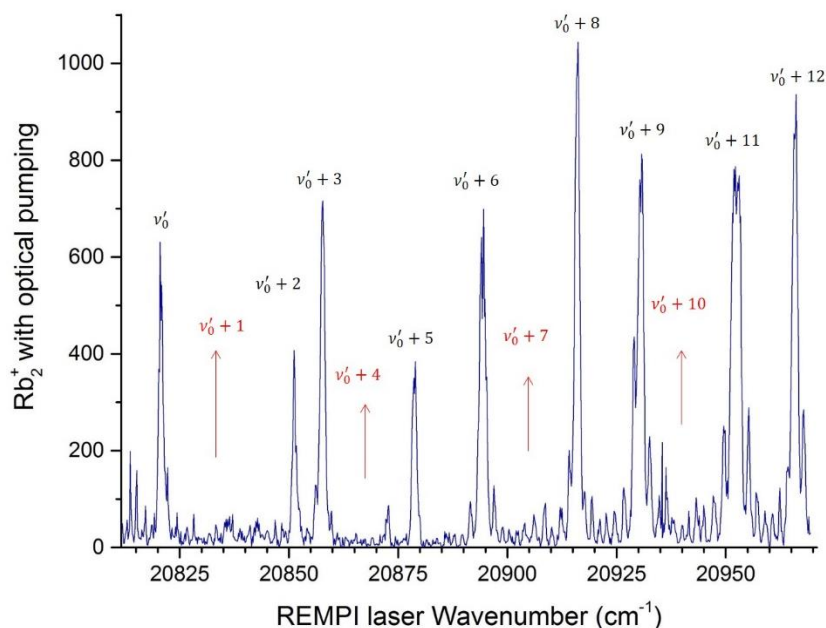


Figure 42 – Experimental vibrational spectrum with optical pumping. The wavelengths were converted to wavenumbers ( $1/\lambda$ ), and the peaks were labeled considering that, for each three consecutive transitions, one of them is missing due to low FCF. This behavior is qualitatively extracted from the Franck-Condon map.

Source: By the author.

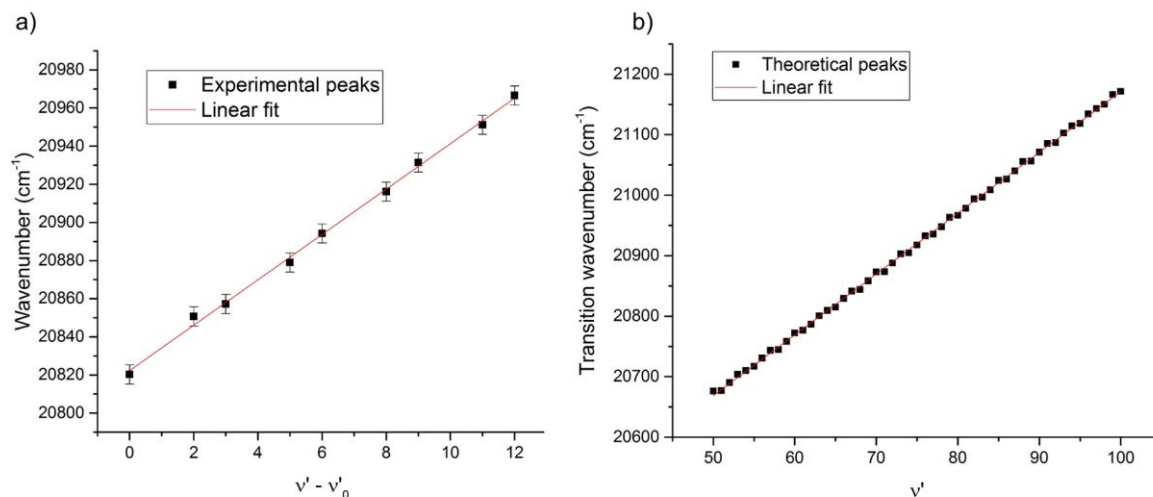


Figure 43 – Transition wavenumbers as a function of the quantum number, for both experimental spectrum (a) and theoretical data (b). The experimental slope of the line is of  $11.9 \text{ cm}^{-1}$ , whereas the theoretical is of  $10.0 \text{ cm}^{-1}$ , showing good agreement. The initial quantum number  $v'_0$  is supposed unknown within the 50 – 100 range.

Source: By the author.

The linear behavior is notable in both theoretical and experimental peaks, which can be understood if we compare the potential in this region with a harmonic oscillator. The linear fit

for the experimental peaks shows a slope of  $(11.9 \pm 0.2) \text{ cm}^{-1}$  per vibrational quantum, whereas the theoretical peaks yield  $(10.0 \pm 0.1) \text{ cm}^{-1}$ , which agrees considerably.

Another situation that could explain the “pairwise” behavior of the experimental peaks is to consider that there are two vibrational states occupied by the molecules on the ground potential, specifically  $\nu = 0$  and  $\nu = 1$ . This is a possible situation because the YAR amplifier generates little power at 1048 nm (see figure 23.b, section 4.2.3), which is the only transition from  $\nu = 1$  available in the vibrational cooling process. If the pumping intensity in this transition is weak, there should also be molecules occupying  $\nu = 1$ , and we should observe REMPI peaks also from this state besides  $\nu = 0$ ; this could explain the “pairwise” peaks. However, if that was the case, the linear slope calculated in figure 43.a) would be around three times greater (because, for each pair of peaks, only one would be from  $\nu = 0$ ), deviating considerably from the theoretical value. We therefore discard this explanation, concluding that the observed peaks can only be from molecules in the  $\nu = 0$  vibrational state.

The arguments that were used in this section are considerably indirect, but a more precise analysis of our spectrum would require a more accurate theoretical map of the transitions from  $X^1\Sigma_g^+$  to  $2^1\Sigma_u^+$ , which is unavailable at the moment.



## 6 FUTURE PERSPECTIVES

This chapter is dedicated to discuss and present future directions that are expected to be taken in our laboratory. Many of the equipment and techniques that will be used are already implemented, but were not performed yet due to the logical sequence of the experiment.

The chapter is divided in three sections. In the first, we discuss the molecular loading and losses experiments, which will complete the present stage in which we are testing our new setup. Second section is a brief discussion about KRb molecules. In the last section, we propose a new technique to promote rotational cooling by optical pumping, using two diffraction gratings to improve the spectral shaping resolution.

### 6.1 Loading and losses of molecules in the ODT

For Rb<sub>2</sub> molecules, we have already demonstrated two processes that were expected to happen with our experimental setup, in which the YAR high power amplifier is seeded with combined sharp band and broadband light sources: the photoassociation, discussed in section 5.2, and the vibrational cooling, as discussed in section 5.5. We have also showed that the YAR beam can also load atoms in an ODT, as verified by fluorescence imaging. To complete this stage of our work, one more process should be demonstrated: the loading of molecules in the ODT.

In order to perform this, a REMPI experiment with pulse trains is proposed. A variation of this technique was already applied by our group with KRb molecules. (88) For this experiment, we propose to measure the molecular signal as a function of the time after the YAR beam is turned on, obtaining a characteristic loading curve of molecules in the ODT. The proposed control sequence is composed of two stages: first, the MOT is normally loaded by keeping the trapping and repumping lights at MOT conditions, and the YAR (PA/ODT) laser off; then the YAR laser is turned on, and the MOT parameters are chopped according to the sequence already described in section 4.4.2, to allow the molecules to be produced and loaded to the ODT. At the second stage, the molecular population is acquired by sending pulses from the REMPI laser. The sequence is represented in figure 44:

	MOT loading	Molecular production and loading
MOT trap/repump parameters	MOT conditions	
MOT Magnetic Fields	ON	ON
PA/ODT laser power	OFF	50 W
REMPI Laser		

Figure 44 – Control sequence of the proposed molecular loading experiment. The first stage is a normal MOT loading, keeping the parameters at constant MOT conditions. In the second stage, the YAR laser (PA/ODT) is turned on and the molecular signal is measured over time by REMPI pulses. At this stage, the MOT parameters are chopped according to figure 30 from section 4.4.2.

Source: By the author.

It is important to point out that, due to low repetition rate, our current REMPI laser of 20 Hz will not be used to this experiment. Instead, a laser with a tunable repetition rate from 1 to 10 kHz will be used, allowing for much better time resolution. We have already installed the laser at the experiment, as well as developed the control and acquisition LabVIEW programs to perform this measurement.

Another proposed experiment is to measure the molecular population decay curve in the ODT. The sequence for this case will also be composed of two stages: in the first, the MOT is chopped in order to produce and load molecules in the ODT; in the second, all the MOT parameters are turned off, leaving only the atoms and molecules trapped in the ODT. The PA/ODT laser must be on at the whole time, and the REMPI pulses are sent during the second stage. The expected signal is a decay curve that shows how the molecules are lost from the ODT. The proposed sequence is shown in figure 45:

	Molecular production and ODT loading	ODT population decay
MOT trap/repump parameters		OFF
MOT Magnetic Fields	ON	OFF
PA/ODT laser power	50 W	50 W
REMPI Laser		

Figure 45 – Control sequence of the molecular population decay in the ODT. The molecules are produced and transferred to the ODT in the first stage. In the second stage, the molecules are left at the ODT and should be lost with time.

Source: By the author.

## 6.2 KRb molecules

Despite the fact that present work was completely carried out with  $^{85}\text{Rb}$  atoms, our experiment has also a complete setup to trap, cool and manipulate  $^{39}\text{K}$  (potassium) atoms, simultaneously to  $^{85}\text{Rb}$  or  $^{87}\text{Rb}$ . This hybrid setup allows for the production of KRb molecules, which have a much greater scientific interest due to their permanent electric dipole moment (as any other heteronuclear diatomic molecule). (12,22,89)

In previous works of our group, the loading of K atoms in a single-species ODT (90) and the simultaneous loading of K and Rb (79) were already demonstrated. As presented in the later work, the populational decay curves of K atoms in the presence and absence of Rb atoms showed a faster decay when both species are present, suggesting that two-body losses were occurring due to photoassociation of KRb molecules (in a similar result to that shown in section 5.1).

For the next stages of our experiment, we expect to reproduce the same processes that we applied to  $\text{Rb}_2$  to KRb molecules: the controlled photoassociation, vibrational cooling and ODT loading, all of them with the new setup that uses the YAR high power laser. The interaction potentials, levels and transitions still have to be calculated; however it is expected that the required KRb frequencies can be reached by the same lasers that we already have in our lab. This can be understood by considering the  $R \rightarrow \infty$  asymptote in the interaction potentials: the energetic difference between  $5s + 5s$  and  $5s + 5p$  in  $\text{Rb}_2$ , for example, is basically the same difference from  $4s + 5s$  and  $4s + 5p$  (considering the order K + Rb) in KRb. Therefore, the energy differences at finite  $R$  from KRb to  $\text{Rb}_2$  are displacements from the same asymptotes, thus expected not to be much different.

## 6.3 Rotational cooling by optical pumping

Our experimental molecular sample is only vibrationally cooled, which is enough for cold collisions experiments. However, ro-vibrationally pure molecules (a term that refers to vibrationally and rotationally controlled states) are useful for many other applications, ranging from fundamental physics tests (17) to quantum computation (21-22) and others. (13)

Until recently, most of the techniques to promote rovibrational cooling were based on the STIRAP method, briefly described in section 3.3. Some alternatives have been proposed recently (91-92), in which optical pumping methods are applied to rotationally cool  $\text{Cs}_2$  molecules. In this section, we propose a technique to rotationally cool  $\text{Rb}_2$  molecules by optical

pumping, using a simple experimental method that is very similar to our vibrational cooling technique.

The main idea is to use a light source with enough bandwidth to access several rotational transitions from  $X\Sigma_g^+$  to an excited potential, and then shape the spectrum to avoid transitions from  $J = 0$  to any other state. However, the energy scale of the rotational splitting is much smaller than that of the vibrational states separation, so the main challenge is to improve the spectral shaping resolution to achieve the rotational splitting scale. In particular, for  $\text{Rb}_2$  molecules, the rotational splitting is the order of  $\sim 1$  GHz ( $0.04 \text{ cm}^{-1}$ ), meaning that our shaping device must have a resolution of the same order or less. This can be achieved by modifying the shaping apparatus shown in section figure 22 (section 4.2.3), using a more dispersive element and a lens with greater focal distance.

Our starting point is the work by Horchani (91), in which a femtosecond pulsed laser beam is dispersed by a diffraction grating, collimated through a lens and then reflected in a *digital light processing* (DLP) unit, a matrix of  $1024 \times 768$  micro-mirrors that can be individually rotated through a digital interface. The DLP is used to select only the desired spectral components, which are retro-reflected to the grating and recombined as a single beam again; the undesired components are deviated and lost. The grating and the DLP are placed at a focal distance  $f$  of the lens, forming the so-called  $4f$  system. This configuration is very common in Fourier optics systems (93), and has the advantage of providing maximum separation between the components in the plane of the mask (Fourier plane). The experimentally achieved resolution was of  $\sim 0.01$  (5GHz). The setup is represented in figure 46.a):

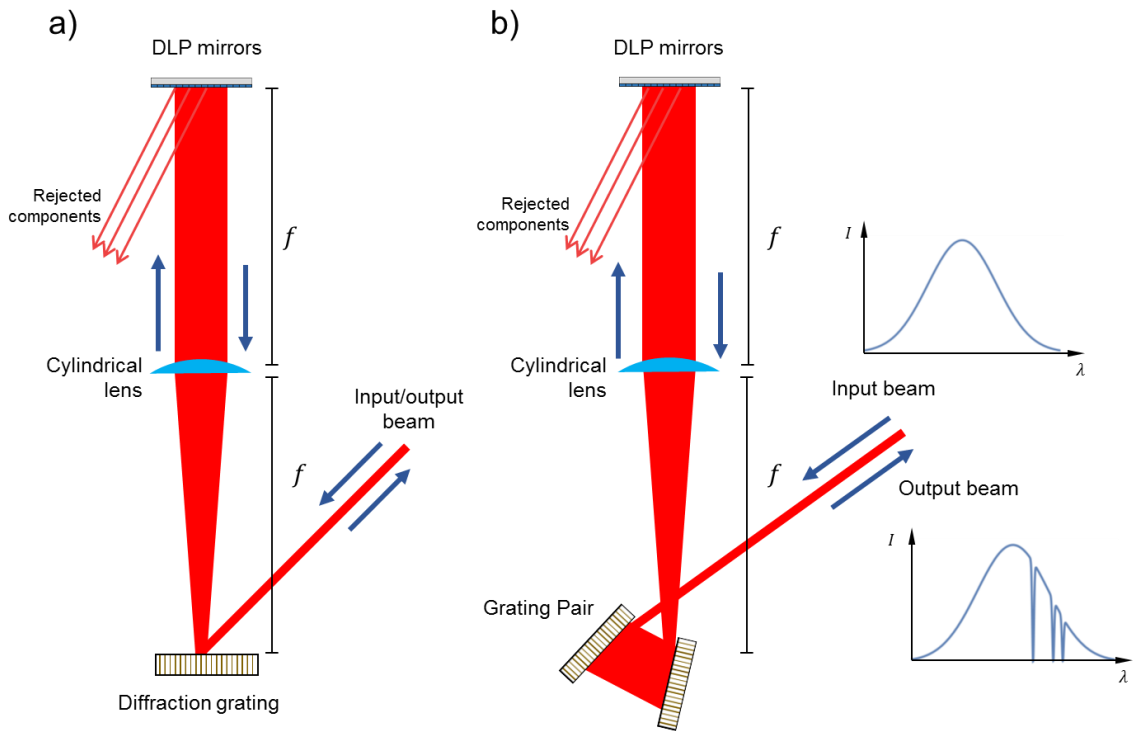


Figure 46 – Comparison between the experimental setup developed by Horchani (91) (a) and our similar proposal using two diffraction gratings (b). In both cases, the dispersed light is collimated by a cylindrical lens and then processed in the DLP mirror matrix, which discards the undesired spectral components. The mirror must be placed at a focal distance  $f$  to the lens, in order to optimize the distinction between spectral components.

Source: By the author.

In order to improve the resolution, our proposal is to replace the single diffraction grating by a pair of gratings in a near-grazing setup, similarly to what have been long used to reduce the linewidth of dye lasers. (94-97) We have developed a simple model to predict if this system can reach the resolution of  $< 1$  GHz with feasible experimental parameters. Consider the equation for diffraction maxima in both gratings, initially for a monochromatic beam:

$$a_1(\sin \theta_1 + \sin \theta_2) = m_1 \lambda \quad (49)$$

$$a_2(\sin \theta_3 + \sin \theta_4) = m_2 \lambda \quad (50)$$

Where  $a_1$  and  $a_2$  are the periodicity of the first and the second grating respectively,  $m_1$  and  $m_2$  are the orders of each diffraction,  $\lambda$  is the wavelength and the angles  $\theta_1$  to  $\theta_4$  are defined according to figure 47:

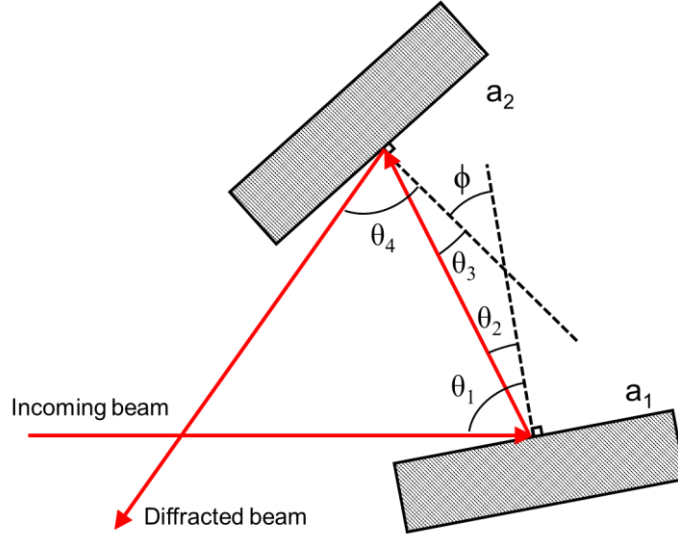


Figure 47 – Schematic representation of the dispersion over the grating pair.  $\phi$  is the angle between the normal vectors of the gratings.  $\theta_1$  and  $\theta_3$  are incidence angles, whereas  $\theta_2$  and  $\theta_4$  are diffraction angles. Source: By the author.

The variables that can be controlled are the first incidence angle  $\theta_1$  and the angle  $\phi$  between the gratings.  $\theta_2$ ,  $\theta_3$  and  $\theta_4$  are dependent variables that can be calculated by equations 49 and 50, as well as the geometrical constraint  $\theta_2 + \theta_3 = \phi$ . In appendix B, we explain in detail the calculation of these angles, and show that the angular dispersion after the second diffraction can be written as:

$$\frac{\partial \theta_4}{\partial \lambda} = \frac{\left( \frac{m_2}{a_2} - \frac{m_1}{a_1} \cdot \frac{\cos \theta_3}{\cos \theta_2} \right)}{\cos \theta_4} \quad (51)$$

The angular dispersion allows us to calculate the spectral width  $\Delta \lambda$  that will be contained in a small angular aperture  $\Delta \theta$  at the diffracted beam by the expression:

$$\Delta \theta = \frac{\partial \theta_4}{\partial \lambda} \Delta \lambda \Leftrightarrow \Delta \lambda = \frac{1}{\partial \theta_4 / \partial \lambda} \cdot \Delta \theta \quad (52)$$

As long as the dispersion is not null. The diffracted beam is collimated by a cylindrical lens at its focal distance  $f$  (see figure 46), meaning that each component of spectral width  $\Delta \lambda$  will span at a spatial length  $\Delta l = \Delta \theta \cdot f$  at the DLP mirror matrix. Considering  $\Delta l$  as the separation between each micro-mirror,  $\Delta \lambda$  is the minimal bandwidth that can be selected by this apparatus, and it is given by:

$$\Delta\lambda = \frac{1}{\partial\theta_4/\partial\lambda} \cdot \frac{\Delta l}{f} \quad (53)$$

We calculate the dependent angles and the resolution considering a broadband light source with central wavelength  $\lambda = 1042$  nm, which is approximately where the rotational transitions from  $X\Sigma_g^+, \nu = 0$  to the  $0_u^+, \nu' = 0$  are located. We consider two diffraction gratings of  $1/a = 1200$  grooves/mm, which is an experimentally feasible value for this wavelength, and a lens with focal distance of 50 cm (notice that greater focal distance decreases  $\Delta\lambda$ , improving the resolution). For the DLP mirror matrix, we consider a separation of  $\Delta l = 13$   $\mu\text{m}$  between each mirror. Both diffractions occur at the first order  $m_1 = 1 = m_2$ . For a considerably (but not exaggeratedly) high incidence angle of  $\theta_1 = 79^\circ$ , and an angle of  $\phi = 31^\circ$  between the gratings, we get a final diffraction angle of  $\theta_4 \approx 80^\circ$ , which is also not too close from  $90^\circ$ , and a resolution of  $\Delta\lambda \approx 0.002$  nm or 0.55 GHz in frequency, which is enough for our purpose. The angles in figure 47 are very closely drawn according to these results.

However, it is important to remark that  $\phi$  is very close to its critical value in which the second diffraction does not occur anymore, thus making the results very sensible to small changes in that angle. The alignment process must take this into account, and the actual resolution may be different from the calculated. This is not a problem, as our calculations were intended only to show that this resolution is attainable. A suggested alignment process is to set the incidence angle to the greatest value as possible (below  $90^\circ$ ), and then to rotate the second grating until a high diffraction angle is achieved.

Another remark is that our model does not consider the resolution loss due to diffraction blur, which can also influence. The calculation of this effect is much more complex, and is beyond the present knowledge of the author. However, the 4f configuration and a high number of illuminated slits in the first grating can reduce this effect to a probably negligible scale.



## 7 CONCLUSIONS

This work provides the guidelines for applying already well-established techniques – the photoassociation and vibrational cooling – in a completely new regime: the  $\sim\text{MW}/\text{cm}^2$  intensity generated by the fiber laser amplifier. Furthermore, the unifying of the PA, vibrational cooling and optical trapping in a single light beam is, from our knowledge, exclusive from our work. Our goals concerning to the demonstration of this method were partially achieved, as we gathered evidences for the PA and vibrational cooling processes in  $\text{Rb}_2$ , but the verification of the optical trapping in the ODT is still needed. Unfortunately, we had no time to work with K atoms and produce the same results for  $\text{KRb}$  molecules during this period.

The REMPI technique is a direct measurement of the molecular density. The signal as presented in figure 27 of section 4.3, containing the atomic and molecular peaks in their time windows, is a final evidence that molecules are present in our sample. Furthermore, the fact that the molecular peak vanishes if the PA laser is turned off proves that the molecules are indeed present due to the photoassociation by this laser, and not to other spurious processes. The results from the PA laser wavenumber scan (section 5.2) are very solid. The wavenumber of the peaks is in well agreement, as well as the rotational splitting between  $J = 0$  and  $J = 1$  peaks, which reinforces the calculations.

The photoassociation process is further confirmed by the molecular signal as a function of the PA laser intensity, presented in figure 38, where the linear dependency is an evidence of the single-photon PA mechanism. The two-photon REMPI process is also in agreement with the dependency on REMPI laser intensity, although in this case the measurement is more uncertain.

When the SLD is included on the YAR high power amplifier, with its spectrum adequately shaped (as explained in section 4.2.3), the molecules are optically pumped to the fundamental vibrational state of the ground potential. Evidences for this process rely on the REMPI laser scan measurements, where the influence of the broadband light is very clear. Without the SLD light, the high density of peaks on the spectrum shows that many vibrational levels are occupied. When the broadband light is included, optical pumping takes place and a single state ( $\nu = 0$ ) is occupied, resulting on a much smaller number of main peaks in the spectrum.

We conclude by fitting our work on the global context of research in ultracold molecules. We try to develop techniques that are notably simpler than the average in this field.

Our laboratory is relatively small when compared to others that work with cold molecules, both in material and human resources, and therefore simplification is a necessary feature of our work. The main example presented in this dissertation is the performance of three tasks (PA, vibrational cooling and trapping) with a single high power laser, which is a considerable simplification of the alignment process. We expect that our contributions can be useful not only by other research groups, but also for those who are working to bring atomic and molecular physics into a more portable scale, a case in which the simplification of the techniques is very desirable.

## REFERENCES

- 1 COHEN, S. M. **Atomism**, 2002. Available from: <<https://faculty.washington.edu/smcohen/320/atomism.htm>>. Accessible at: 6 Dec. 2016.
- 2 TOULMIN, S.; GOODFIELD, J. **The architecture of matter**. Chicago: University of Chicago Press, 1962.
- 3 WALTER, J. M.; BARRATT, S. The existence of intermetallic compounds in the vapour state. The spectra of the alkali metals, and of their alloys with each other. **Proceedings of the Royal Society of London A**, v. 119, n. 782, p. 221, 1928.
- 4 EINSTEIN, A. Quantentheorie des ainatomigen idealen gases. **Sitzungsberichte der Preussischen Akademie der Wissenschaften**, p. 261-267, 1924.
- 5 COOPER, L. N. Bound electron pairs in a degenerate Fermi gas. **Physical Review**, v. 104, n. 4, p. 1189-1190, 1956.
- 6 HANSCH, T. W.; SCHAWLOW, A. L. Cooling of gases by laser radiation. **Optics Communications**, v. 13, n. 1, p. 68-69, 1975.
- 7 PHILLIPS, W.; METCALF, H. Laser deceleration of an atomic beam. **Physical Review Letters**, v. 48, n. 9, p. 596-599, 1982.
- 8 MIGDALL, A. L. et al. First observation of magnetically trapped neutral atoms. **Physical Review Letters**, v. 54, n. 24, p. 2596-2599, 1985.
- 9 ASHKIN, A. et al. Observation of a single-beam gradient force optical trap for dielectric particles. **Optics Letters**, v. 11, n. 5, p. 288 - 290, 1986.
- 10 GALLAGHER, T. F. Rydberg atoms. **Reports on Progress in Physics**, v. 51, n. 2, p. 143-188, 1988.
- 11 WEIDEMÜLLER, M. Rydberg atoms: there can be only one. **Nature Physics**, v. 5, n. 2, p. 91-92, 2009.
- 12 DEMILLE, D.; HUDSON, E. R. Ultracold molecules - the coldest polar region. **Nature Physics**, v. 4, n. 12, p. 911-912, 2008.
- 13 GADWAY, B.; YAN, B. Strongly interacting ultracold polar molecules. **Journal of Physics B**, v. 49, n. 15, p. 152002, 2016.
- 14 CAHN, S. B. et al. Zeeman-tuned rotational level-crossing spectroscopy in a diatomic free radical. **Physical Review Letters**, v. 112, n. 16, p. 163002, 2014.
- 15 BARON, J. et al. Order of magnitude smaller limit on the electric dipole moment of the electron. **Science**, v. 343, n. 6168, p. 269-272, 2014.

- 16 DEMILLE, D. et al. Enhanced sensitivity to variation of  $m_e/m_p$  in molecular spectra. **Physical Review Letters**, v. 100, n. 4, p. 043202, 2008.
- 17 DEMILLE, D. Diatomic molecules, a window onto fundamental physics. **Physics Today**, v. 68, n. 12, 2015.
- 18 CHIN, C.; FLAMBAUM, V. V.; KOZLOV, M. G. Ultracold molecules: new probes on the variation of fundamental constants. **New Journal of Physics**, v. 11, p. 055048, 2009.
- 19 CARR, L. D. et al. Cold and ultracold molecules: science, technology and applications. **New Journal of Physics**, v. 11, p. 055049, 2009.
- 20 OSPELKAUS, S. et al. Quantum-state controlled chemical reactions of ultracold potassium-rubidium molecules. **Science**, v. 327, n. 5967, p. 853-857, 2010.
- 21 ANDRÉ, A. et al. A coherent all-electrical interface between polar molecules and mesoscopic superconducting resonators. **Nature Physics**, v. 2, n. 9, p. 636-642, 2006.
- 22 DEMILLE, D. Quantum computation with trapped polar molecules. **Physical Review Letters**, v. 88, n. 6, p. 067901, 2002.
- 23 WEI, Q. et al. **Quantum computation using arrays of N polar molecules in pendular states**. ArXiv, 2016 Available from: <<https://arxiv.org/abs/1607.04959>>. Accessible at: 15 Dec. 2016.
- 24 PUPILLO, G. et al. Cold atoms and molecules in self-assembled dipolar lattices. **Physical Review Letters**, v. 100, n. 5, p. 050402, 2008.
- 25 BÜCHLER, H. P. et al. Strongly correlated 2D quantum phases with cold polar molecules: controlling the shape of the interaction potential. **Physical Review Letters**, v. 98, n. 6, p. 060404, 2007.
- 26 MEERAKKER, S. Y. T. et al. Direct measurement of the radiative lifetime of vibrationally excited OH radicals. **Physical Review Letters**, v. 95, n. 1, p. 013003, 2005.
- 27 STAANUM, P. et al. Experimental investigation of ultracold atom-molecule collisions. **Physical Review Letters**, v. 96, n. 2, p. 023201, 2006.
- 28 BORN, M.; OPPENHEIMER, J. R. **On the quantum theory of molecules**. Translated version of the original article. Available from: <<http://www.chm.bris.ac.uk/pt/manby/papers/bornop.pdf>>. Accessible at: 27 July 2016.
- 29 AVOIRD, A. V. D. **Derivation of the Born-Oppenheimer approximation**, 2007. Available from: <<http://www.acmm.nl/molsim/han/2007/part4.pdf>>. Accessible at: 27 July 2016.
- 30 SHERRILL, D. **The Born-Oppenheimer approximation**, 2001. Available from: <<http://vergil.chemistry.gatech.edu/notes/quantrev/node31.html>>. Accessible at: 27 July 2016.

- 31 HERZBERG, G. **Molecular spectra and molecular structure**. 2nd. ed. Princeton: D. Van Nostrand Company, 1950. v. 1.
- 32 VALEEV, E. F.; SHERRILL, C. D. The diagonal Born–Oppenheimer correction beyond the Hartree–Fock approximation. **Journal of Chemical Physics**, v. 118, n. 9, p. 3921-3927, 2003.
- 33 GRIFFITHS, D. J. Identical particles. In: \_\_\_\_\_. **Introduction to quantum mechanics**. 2nd. ed. Upper Saddle River: Pearson Prentice Hall, 2005. chap. 5, p. 484.
- 34 GRIFFITHS, D. J. Quantum mechanics in three dimensions. In: \_\_\_\_\_. **Introduction to quantum mechanics**. 2nd. ed. Upper Saddle River: Pearson Prentice Hall, 2005. chap. 4, p. 484.
- 35 BROWN, J.; CARRINGTON, A. Electronic and vibrational states. In: \_\_\_\_\_. **Rotational spectroscopy of diatomic molecules**. New York: Cambridge University Press, 2003. chap. 6, p. 177-289.
- 36 COHEN-TANNOUDJI, C.; DIU, B.; LALOË, F. Complement C-VI - Rotation of diatomic molecules. In: \_\_\_\_\_. **Quantum mechanics**. 2nd. ed. Paris: Hermann, 1978. v. 1. p. 712-726.
- 37 STEPANOV, N. F.; ZHILINSKII, B. I. When and why Hund's cases arise. **Journal of Molecular Spectroscopy**, v. 52, n. 2, p. 277-286, 1974.
- 38 HERZBERG, G. Finer details about electronic states and electronic transitions. In: \_\_\_\_\_. **Molecular spectra and molecular structure**. 2nd. ed. Princeton: D. Van Nostrand Company, 1950. v. 1. chap. V, p. 212-308.
- 39 HERZBERG, G. Elementary discussion of electronic states and electronic transitions. In: \_\_\_\_\_. **Molecular spectra and molecular structure**. 2nd. ed. Princeton: D. Van Nostrand Company, 1950. v. 1. chap. IV, p. 146-204.
- 40 FRANCK, J.; DYMOND, E. G. Elementary processes of photochemical reactions. **Transactions of Faraday Society**, v. 21, p. 536-542, 1926.
- 41 CONDON, E. U. Nuclear motions associated with electron transitions in diatomic molecules. **Physical Review**, v. 32, n. 6, p. 858-872, 1928.
- 42 STWALLEY, W. C.; WANG, H. Photoassociation of ultracold atoms: a new spectroscopic technique. **Journal of Molecular Spectroscopy**, v. 195, n. 2, p. 194–228, 1999.
- 43 RAAB, E. L. et al. Trapping of neutral sodium atoms with radiation pressure. **Physical Review Letters**, v. 59, n. 23, p. 2631, 1987.
- 44 THORSHEIM, H. R.; WEINER, J.; JULIENNE, P. S. Laser-induced photoassociation of ultracold sodium atoms. **Physical Review Letters**, v. 58, n. 23, p. 2420-2423, 1987.

- 45 LETT, P. D. et al. Spectroscopy of Na<sub>2</sub> by photoassociation of laser-cooled Na. **Physical Review Letters**, v. 71, n. 14, p. 2200-2203, 1993.
- 46 VIVANCO, F. J. et al. A simplified method for identification of the vibrational series of long-range states in Na<sub>2</sub>. **Brazilian Journal of Physics**, v. 45, n. 3, p. 272–279, 2015.
- 47 VESHAPIDZE, G. et al. Pathway for two-color photoassociative ionization with ultrafast optical pulses in a Rb magneto-optical trap. **Physical Review A**, v. 76, n. 5, p. 051401, 2007.
- 48 PAIVA, R. et al. Photoassociative ionization of Na inside a storage ring. **Optics Communications**, v. 285, n. 8, p. 2085–2089, 2012.
- 49 MILLER, J. D.; CLINE, R. A.; HEINZEN, D. J. Photoassociation spectrum of ultracold Rb atoms. **Physical Review Letters**, v. 71, n. 14, p. 2204-2207, 1993.
- 50 ABRAHAM, E. R. I. et al. Photoassociative spectroscopy of long-range states of ultracold <sup>6</sup>Li<sub>2</sub> and <sup>7</sup>Li<sub>2</sub>. **Journal of Chemical Physics**, v. 103, n. 18, p. 7773-7778, 1995.
- 51 WANG, H.; GOULD, P. L.; STWALLEY, W. C. Photoassociative spectroscopy of ultracold K atoms in a high-density vapor-cell magneto-optical trap. **Physical Review A**, v. 53, n. 3, 1996.
- 52 FIORETTI, A. et al. Formation of cold Cs<sub>2</sub> molecules through photoassociation. **Physical Review Letters**, v. 80, n. 20, p. 4402-4405, 1998.
- 53 WANG, H.; STWALLEY, W. C. Ultracold photoassociative spectroscopy of heteronuclear alkali-metal diatomic. **Journal of Chemical Physics**, v. 108, n. 14, p. 5767-5771, 1998.
- 54 SHAFFER, J. P.; CHALUPCZAK, W.; BIGELOW, N. P. Photoassociative ionization of heteronuclear molecules. **Physical Review Letters**, v. 82, n. 6, p. 1124-1127, 1999.
- 55 KÖHLER, T.; GÓRAL, K.; JULIENNE, P. S. Production of cold molecules via magnetically tunable Feshbach resonances. **Reviews of Modern Physics**, v. 78, n. 4, p. 1311-1361, 2006.
- 56 STWALLEY, W. C. Stability of spin-aligned hydrogen at low temperatures and high magnetic fields: new field-dependent scattering resonances and predissociations. **Physical Review Letters**, v. 37, n. 24, p. 1628, 1976.
- 57 PH. COURTEILLE, R. S. F. A. D. J. H. Observation of a Feshbach resonance in cold atom scattering. **Physical Review Letters**, v. 81, n. 1, p. 69-72, 1998.
- 58 INOUE, S. et al. Observation of Feshbach resonances in a Bose-Einstein condensate. **Nature**, v. 392, n. 6672, p. 151-154, 1998.
- 59 THALHAMMER, G. et al. Long-lived Feshbach molecules in a three-dimensional optical lattice. **Physical Review Letters**, v. 96, n. 5, p. 050402, 2016.

- 60 STIMULATED raman adiabatic passage in physics, chemistry and technology - what is STIRAP?, 2015. Available from: <<http://www.stirap.com/What%20is%20STIRAP.pdf>>. Accessible at: 18 July 2016.
- 61 UNANYANA, R. et al. Robust creation and phase-sensitive probing of superposition states via stimulated Raman adiabatic passage (STIRAP) with degenerate dark states. **Optics Communications**, v. 155, n. 1-3, p. 144-154, 1998.
- 62 NESTERENK, V. O. et al. STIRAP transport of Bose-Einstein condensate in triple-well trap. **Laser Physics**, v. 19, n. 4, p. 616, 2009.
- 63 PANDA, C. D. et al. STIRAP preparation of a coherent superposition of ThO H<sub>3</sub>Δ<sub>1</sub> states for an improved electron EDM measurement. **Physical Review A**, v. 93, n. 5, p. 052110-052114, 2016.
- 64 AIKAWA, K. et al. Coherent transfer of photoassociated molecules into the rovibrational ground state. **Physical Review Letters**, v. 105, n. 20, p. 203001, 2010.
- 65 VITEAU, M. et al. Optical pumping and vibrational cooling of molecules. **Science**, v. 321, n. 5886, p. 232-234, 2008.
- 66 SOFIKITIS, D. et al. Vibrational cooling of cesium molecules using noncoherent broadband light. **Physical Review A**, v. 80, n. 5, p. 051401, 2009.
- 67 MARANGONI, B. S. **Colisões heteronucleares em uma armadilha de dipolo**. 2013. 139 p. Tese (Doutorado em Ciências) - Instituto de Física de São Carlos, Universidade de São Paulo, São Carlos, 2013.
- 68 MENEGATTI, C. R. **Armadilha de dipolo para átomos e moléculas**. 2011. 162 p. Tese (Doutorado em Ciências) – Instituto de Física de São Carlos, Universidade de São Paulo, São Carlos, 2011.
- 69 STECK, D. A. **Rubidium 85 D line data**, 2008. Available from: <<http://steck.us/alkalidata/rubidium85numbers.pdf>>. Accessible at: 23 Sep. 2016.
- 70 KUROSU, T.; SHIMIZU, F. Laser cooling and trapping of calcium and strontium. **Japanese Journal of Applied Physics**, v. 29, n. 11, p. L2127, 1990.
- 71 SHUMAN, E. S.; BARRY, J. F.; DEMILLE, D. Laser cooling of a diatomic molecule. **Nature**, v. 467, n. 7317, p. 820 - 823, 2010.
- 72 GRIMM, R.; WEIDEMÜLER, M. Optical dipole traps for neutral atoms. **Advances In Atomic, Molecular, and Optical Physics**, v. 42, p. 95 - 170, 2000.
- 73 BJORKHOLM, J. E. et al. Observation of focusing of neutral atoms by the dipole forces of resonance-radiation pressure. **Physical Review Letters**, v. 41, n. 20, p. 1361 - 1364, 1978.

- 74 JACKSON, J. D. Maxwell equations, macroscopic electromagnetism, conservation laws. In: \_\_\_\_\_. **Classical electrodynamics**. 3rd. ed. Hoboken: John Wiley & Sons Inc, 1999. chap. 6, p. 237-294.
- 75 PRESTON, D. W. Doppler-free saturated absorption: laser spectroscopy. **American Journal of Physics**, v. 64, n. 11, p. 1432-1436, 1996.
- 76 PASSAGEM, H. F. **Fotoassociação de curto alcance em átomos de rubídio**. 2016. 80 p. Dissertação (Mestrado em Ciências) - Instituto de Física de São Carlos, Universidade de São Paulo, São Carlos, 2016.
- 77 ARNAUD, J. A. Modes of propagation of optical beams in helical gas lense. **Applied Optics**, v. 10, n. 5, p. 2775-2776, 1971.
- 78 MENEGATTI, C. R. et al. Trap loss in a rubidium crossed dipole trap by short-range photoassociation. **Physical Review A**, v. 87, n. 5, p. 053404, 2013.
- 79 MENEGATTI, C. R. et al. Simultaneous loading of 39K and Rb into a crossed dipole trap: characterization and two-body losses. **Physical Review A**, v. 88, n. 2, p. 023411, 2013.
- 80 STANDARD, J. M.; CLARK, B. K. The Franck-Condon principle and Condon parabolas in a physical chemistry or quantum physics course. **Journal of Chemical Education**, v. 76, n. 10, p. 1363-1366, 1999.
- 81 LE ROY, R. J. LEVEL: a computer program for solving the radial Schrödinger equation for bound and quasibound levels. **Journal of Quantitative Spectroscopy and Radiative Transfer**, v. 186, p. 167-178, 2017. In press.
- 82 HAIMBERGER, C. et al. Formation and detection of ultracold ground-state polar molecules. **Physical Review A**, v. 70, n. 2, p. 021402(R), 2004.
- 83 HUANG, Y. et al. Formation, detection and spectroscopy of ultracold Rb<sub>2</sub> in the ground X<sup>1</sup>Σ<sub>g</sub><sup>+</sup> state. **Journal of Physics B**, v. 39, n. 19, p. S857–S869, 2006.
- 84 STREIBEL, T.; ZIMMERMANN, R. Resonance-enhanced multiphoton ionization mass spectroscopy (REMPI-MS): applications for process analysis. **Annual Review of Analytical Chemistry**, v. 7, p. 361-381, 2014.
- 85 COUMARIN 480. Exciton reference page for laser dyes. Available from: <<http://www.exciton.com/pdfs/c480.pdf>>. Accessible at: 14 Nov. 2016.
- 86 KUPPENS, S. et al. Loading an optical dipole trap. **Physical Review A**, v. 62, n. 1, p. 013406, 2000.
- 87 DEIB, M. et al. Mixing of 0<sup>+</sup> and 0<sup>-</sup> observed in the hyperfine and Zeeman structure of ultracold Rb<sub>2</sub> molecules. **New Journal of Physics**, v. 17, p. 083032, 2015.

- 88 MENEGATTI, C. R.; MARANGONI, B. S.; MARCASSA, L. G. Observation of cold Rb<sub>2</sub> molecules trapped in an optical dipole trap using a laser-pulse-train technique. **Physical Review A**, v. 84, n. 5, p. 053405, 2011.
- 89 LAHAYE, T. et al. The physics of dipolar bosonic quantum gases. **Reports on Progress in Physics**, v. 72, n. 12, p. 126401, 2009.
- 90 MARANGONI, B. S.; MENEGATTI, C. R.; MARCASSA, L. G. Loading a 39K crossed optical dipole trap from a magneto-optical trap. **Journal of Physics B**, v. 45, n. 7, p. 175301, 2012.
- 91 HORCHANI, R. Femtosecond laser shaping with digital light processing. **Optical and Quantum Electronics**, v. 47, n. 8, p. 3023-3030, 2015.
- 92 MANAI, I. et al. Rovibrational cooling of molecules by optical pumping. **Physical Review Letters**, v. 109, n. 18, p. 183001, 2012.
- 93 HECHT, E. Fourier optics. In: \_\_\_\_\_. **Optics**. 4th. ed. Boston: Addison-Wesley, 2001. p. 521-561.
- 94 LITTMAN, M. G. Single-mode operation of grazing-incidence pulsed dye laser. **Optics Letters**, v. 3, n. 4, p. 138-140, 1978.
- 95 ILES, M. K.; DSILVA, A. P.; FASSEL, V. A. Single mode nitrogen pumped dye laser. **Optics Communications**, v. 35, n. 1, p. 133-136, 1980.
- 96 HUNG, N. D.; BRECHIGNAC, P.; COUTANT, B. A quasi double-grating grazing incidence pulsed dye laser. **Applied Physics B**, v. 51, n. 1, p. 75-79, 1990.
- 97 HUNG, N. D.; BRECHIGNAC, P. A single-mode single-grating grazing incidence pulsed dye laser. **Optics Communications**, v. 54, n. 3, p. 151-154, 1985.
- 98 GRIFFITHS, D. J. Electromagnetic waves. In: \_\_\_\_\_. **Introduction to electrodynamics**. 3rd. ed. Upper Saddle River: Prentice Hall, 1999. p. 364 - 411.
- 99 BROWN, J. M.; CARRINGTON, A. **Rotational spectroscopy of diatomic molecules**. Cambridge: Cambridge University Press, 2003.



## APPENDIX A – Justification of the “1/2” factor on the optical dipole force

In this appendix, which is a complement to section 4.1.3, we will give a simplified argument to justify the “1/2” factor that is included on the potential energy of an induced dipole interacting with an oscillating electric field.

The fundamental expression of the dipole-field interaction is the equation for the force (see reference (100), eq. 4.5):

$$\mathbf{F} = (\mathbf{d} \cdot \nabla) \mathbf{E} \quad (54)$$

Here  $\mathbf{d}$  is the electric dipole moment,  $\mathbf{E}$  is the electric field and  $\mathbf{F}$  is the net force that the dipole is subject to. By “fundamental”, it must be understood that this equation does not depend on the dipole behavior, i.e., if it is permanent or induced.

For simplicity, we will consider a one-dimensional case, for which vector quantities become scalar, and there is only one spatial coordinate (say  $x$ ). The three-dimensional case can be obtained with a similar argumentation, but more complicated calculations. In this case, equation 54 becomes:

$$F = d \cdot \frac{\partial E}{\partial x} \quad (55)$$

The potential energy can be obtained by integrating the force over a range which goes from  $x_0$  to  $x_f$ :

$$U_{x_0}(x_f) = - \int_{x_0}^{x_f} d \cdot \frac{\partial E}{\partial x} dx = -d \cdot E|_{x_0}^{x_f} + \int_{x_0}^{x_f} \frac{\partial d}{\partial x} \cdot E dx \quad (56)$$

Where in the second step we have used integration by parts. If the dipole moment is permanent, the second integral on the last expression vanishes, as  $d$  is a constant and  $\frac{\partial d}{\partial x} = 0$ . If however we assume that  $d = \alpha E$ , i.e., the dipole is linearly polarizable with the field (as in equation 43), then equation 56 becomes:

$$U_{x_0}(x_f) = - \int_{x_0}^{x_f} \alpha E \cdot \frac{\partial E}{\partial x} dx = -d \cdot E|_{x_0}^{x_f} + \int_{x_0}^{x_f} \alpha \frac{\partial E}{\partial x} \cdot E dx \quad (57)$$

Which is equivalent to:

$$U_{x_0}(x_f) = -d \cdot E|_{x_0}^{x_f} - U_{x_0}(x_f) \quad (58)$$

Solving for  $U_{x_0}(x_f)$ , we have:

$$U_{x_0}(x_f) = -\frac{d \cdot E|_{x_0}^{x_f}}{2} \quad (59)$$

This is the instantaneous potential energy for an induced electric dipole moment, in a one-dimensional electric field, and the only difference for the permanent dipole is the factor “1/2”. The main idea that we can extract from these calculations is that the variation of the electric dipole affects the way of calculating the potential energy. More general dependencies of  $d$  on  $E$  could generate more complicated corrections.

## APPENDIX B – Proof of the angular dispersion equation

We show now the proof of equation 51 in section 6.3, the angular dispersion after the two-grating diffraction. As an intermediate step, we also show how the unknown angles of the problem are related to the controllable parameters.

We start by rewriting equations 49 and 50 for the diffraction maxima of a monochromatic source:

$$a_1(\sin \theta_1 + \sin \theta_2) = m_1 \lambda \quad (60)$$

$$a_2(\sin \theta_3 + \sin \theta_4) = m_2 \lambda \quad (61)$$

Where  $a_1, a_2$  are the periodicity of the gratings,  $m_1, m_2$  are the orders of the diffraction,  $\lambda$  is the light wavelength and the angles from  $\theta_1$  to  $\theta_4$  were defined in figure 47. The normal directions of the gratings form an angle  $\phi$  between them, which imposes the geometrical constraint:

$$\theta_2 + \theta_3 = \phi \quad (62)$$

Considering that  $\theta_1, \phi$  are controllable variables and  $a_1, a_2, m_1, m_2$  and  $\lambda$  are parameters, we have three unknown variables  $\theta_2, \theta_3, \theta_4$ , and three equations for them, so the problem is already closed with these equations. The solution for the unknown angles is:

$$\theta_2 = \arcsin\left(\frac{m_1 \lambda}{a_1} - \sin \theta_1\right) \quad (63)$$

$$\theta_3 = \phi - \theta_2 \quad (64)$$

$$\theta_4 = \arcsin\left(\frac{m_2 \lambda}{a_2} - \sin \theta_3\right) \quad (65)$$

Equations 63, 64 and 65 provide a simple algorithm to calculate the angles in sequence. Although we initially state the equations for monochromatic light, we want to study the behavior of polychromatic light, for which each spectral component  $\lambda$  is diffracted to slightly different angles. The angular dispersion is a quantity that measures how great the angular difference between the components around  $\lambda$  is. For the first diffraction, the angular dispersion  $\partial\theta_2/\partial\lambda$  is calculated by differentiating both sides of equation 60 with respect to the output angle  $\theta_2$ :

$$\frac{\partial}{\partial \theta_2} [m_1 \lambda] = \frac{\partial}{\partial \theta_2} [a_1 (\sin \theta_1 + \sin \theta_2)] \quad (66)$$

$$m_1 \frac{\partial \lambda}{\partial \theta_2} = a_1 \cos \theta_2 \quad (67)$$

$$\frac{\partial \theta_2}{\partial \lambda} = \frac{m_1}{a_1 \cos \theta_2} \quad (68)$$

For the first diffraction, the formula is simplified because the incidence angle  $\theta_1$  is an independent variable. This is not the case for the second diffraction, for which the incidence angle  $\theta_3$  depends on  $\lambda$ . Differentiating equation 61 with respect to  $\theta_4$  on both sides:

$$\frac{\partial}{\partial \theta_4} [m_2 \lambda] = \frac{\partial}{\partial \theta_4} [a_2 (\sin \theta_3 + \sin \theta_4)] \quad (69)$$

$$m_2 \frac{\partial \lambda}{\partial \theta_4} = a_2 \frac{\partial \sin \theta_3}{\partial \lambda} \frac{\partial \lambda}{\partial \theta_4} + a_2 \cos \theta_4 \quad (70)$$

$$\frac{\partial \theta_4}{\partial \lambda} = \frac{\left( \frac{m_2}{a_2} - \frac{\partial \sin \theta_3}{\partial \lambda} \right)}{\cos \theta_4} \quad (71)$$

Equation 71 isolates the final angular dispersion, but we still have to calculate  $\partial \sin \theta_3 / \partial \lambda$ . This is feasible, as we know the dependence of  $\theta_3$  on  $\theta_2$ , as well as the dependence of  $\theta_2$  on  $\lambda$ . Using the geometrical constraint of equation 62 and the chain rule:

$$\frac{\partial \sin \theta_3}{\partial \lambda} = \frac{\partial \sin(\phi - \theta_2)}{\partial \theta_2} \frac{\partial \theta_2}{\partial \lambda} = -\cos(\phi - \theta_2) \left( \frac{m_1}{a_1 \cos \theta_2} \right) = -\frac{m_1}{a_1} \frac{\cos \theta_3}{\cos \theta_2} \quad (72)$$

Therefore, the final expression for the angular dispersion after the second diffraction is:

$$\frac{\partial \theta_4}{\partial \lambda} = \frac{\left( \frac{m_2}{a_2} - \frac{m_1}{a_1} \cdot \frac{\cos \theta_3}{\cos \theta_2} \right)}{\cos \theta_4} \quad (73)$$